Pixel detector performance and study of CP invariance in H to tau tau decays with the ATLAS detector

Steffen Mæland

Avhandling for graden philosophiae doctor (ph.d.)
Universitetet i Bergen
2018

UNIVERSITETET I BERGEN

Pixel detector performance and study of CP invariance in H to tau tau decays with the ATLAS detector

Steffen Mæland

Avhandling for graden philosophiae doctor (ph.d.)
ved Universitetet i Bergen

2018

Dato for disputas: 27.04.2018

År: 2018

Tittel: Pixel detector performance and study of CP invariance in H to tau tau decays with the ATLAS detector

Navn: Steffen Mæland

Trykk: Skipnes Kommunikasjon / Universitetet i Bergen

Pixel detector performance and study of *CP* invariance in $H \to \tau\tau$ decays with the ATLAS detector

Steffen Mæland

Dissertation for the degree of Philosophiae Doctor (PhD)

Department of Physics and Technology
University of Bergen

January 2018

Abstract

Following its discovery by the ATLAS and CMS experiments in 2012, the Higgs boson has been studied in a multitude of decay modes. So far, its measured properties match very well with the predictions of the Standard Model of particle physics, which postulates the existence of a scalar field, to which all massive particles must couple. The scalar hypothesis can be tested by studying these couplings in detail. Several models predict an extension of the Higgs sector, which would involve a minimum of four additional Higgs bosons. These can potentially mix with each other, altering the kinematics of how the 125 GeV boson decays. This thesis presents a study of the potential for probing for new physics in Higgs decays into pairs of tau leptons. The correlation between the spin directions of the taus is reconstructed from the kinematics of the tau decay products, resulting in an observable angle, which is sensitive to the charge-parity (*CP*) state of the Higgs.

Successful reconstruction of tau leptons rely on the information from the ATLAS tracking detectors. The innermost part of the detector, consisting of high-granularity pixel sensors, was before the beginning of 2015 operation upgraded with an additional pixel layer, the IBL, positioned extremely close to the collision point. Part of this thesis is devoted to the readout software which converts pixel detector output into data objects used by the event reconstruction algorithms. This software provides the mapping from the subdetector-specific module identification numbers, to the global ATLAS coordinate system.

The intense conditions close to the collision point, under the record-breaking luminosity delivered by the LHC during the past three years of running, causes constant damage to the pixel sensors. To both ensure optimal operation of the detector, and to provide numbers to which simulations can be compared, a study has been carried out to measure the bias voltage required to fully deplete the sensors. Dedicated voltage scans have been performed at several occasions, to find the evolution of the depletion voltage over time.

Acknowledgements

The work presented in this thesis has benefited greatly from the collaboration and support from several people. First and foremost I would like to thank my supervisor Prof. Bjarne S. Stugu, for sharing many years of knowledge and experience with Higgses and taus. I very much appreciate the freedom I have had, and the opportunity to stay at CERN for a longer period of time. I would also like to thank my co-supervisor Prof. Gerald Eigen, and the other professors at the institute, Prof. Anna Lipniacka and Prof. Per Osland, for advice along the way.

My first task in ATLAS was not among the easiest, but I was lucky to be welcomed into the fearless bytestream converter team alongside Laura Franconi and Prof. Mapo Giordani, who both quickly impressed me with their level of dedication and aspiration. There is little doubt that we know page 67 of the ROD-BOC manual better than anyone, the original authors included. I owe great thanks to Mapo for continued support with both the pixel software, and with the depletion voltage measurements. From the pixel community I have also received a lot of helpful advice from Silvia Miglioranzi and Soshi Tsuno.

In the Higgs to Leptons group I have had the pleasure of collaborating with several talented and enthusiastic PhD students. A special thanks goes to co-analyser of Higgs *CP* invariance and $Z \to \tau\tau$ authority Maike Hansen; coding prodigy and Scandinavian sociology expert Eric Drechsler; and machine learner and globetrotter Brian Le. Many thanks to the Higgs *CP* analysis coordinators Daniele Zanzi, Christian Grefe and Elias Coniavitis.

Colleagues in Bergen have meant great deal, both in terms of maintaining the analysis and computing infrastructure (for which we all owe Bertrand Martin more or less everything), but of course also for providing a great social environment. Thanks to all of you: Ørjan Dale, Therese Sjursen, Jan Lindroos, Justas Zalieckas, Alex Kastanas, Simen Hellesund, and Andreas Heggelund.

Lastly, a special and sincere thanks to Inga Strümke. Little did I know, knocking on your office door that day in May three years ago.

S.

Contents

Chapter 1

Introduction

The announcement of the discovery of the Higgs boson on July 4, 2012, some 40 years after its existence was first proposed, marked two great successes of particle physics; first, the last missing piece of the Standard Model (SM) was finally identified, laying the foundation for the mechanism for how particles can have mass in a renormalisable theory; second, the very successful design and operation of the Large Hadron Collider, and the experiments surrounding it. The end of 2012 closed off the so-called Run 1 of the LHC, followed by a two-and-a-half year technical stop during which both the LHC and the ATLAS experiment were upgraded to deliver and record collisions at nearly twice the energy. The beginning of Run 2 heralded a new period in particle physics, where the aim was no longer to search for the Higgs, but now to measure its properties, its production and its decays, to identify if it really fits with the Standard Model expectation. Naturally, direct searches for beyond-SM physics is still a vital part of the ATLAS programme. But a strong indication of new physics, even far beyond the current LHC energy, would be if the Higgs properties turned out to deviate from the expectation. A good example would be if Higgs decays were to violate charge-parity (*CP*) symmetry — if the Higgs boson is not a pure scalar particle, as predicted by the SM, but rather a mixture containing a pseudoscalar component, this implies that additional Higgs bosons must exist. This is exactly the aim of the study presented in part III of the thesis. This study looks at the decay of the Higgs into pairs of tau leptons, which is arguably the most promising decay to probe *CP* violation in Yukawa interactions. In the SM, where neutrinos are considered massless, the only source of *CP* violation is in the quark mixing matrix. This effect is, however, not sizeable enough to explain the imbalance between matter and antimatter observed throughout the universe, giving a reason to believe that other sources of *CP* violation should exist.

The $H \to \tau\tau$ *CP* analysis was started from scratch in early 2015, with the author as one of two PhD students responsible for the main parts of the analysis. Since there is significant overlap with this analysis and the cross section measurement, I have also contributed to the analysis software used for the di-hadronic decay mode of the $H \to \tau\tau$ cross section measurement. Likewise, analysers working on the cross section measurement have also contributed to the *CP* analysis. Prior to getting involved with the analysis work, I took part in updating the software devoted to converting the raw data output from the pixel detector into an ATLAS-general format, so that it can be used in track reconstruction. This coincided with the commissioning of the new

addition to the ATLAS inner detector in 2014, the Insertable *b*-Layer (IBL). Continued changes in the readout system required the software to be actively maintained for two years to follow; chapter 4 describes the functionality and improvements added to the software. While engaged in the pixel community I started a study of the depletion voltage in the IBL and the pixel layers, a task touching the areas of both detector operation and sensor performance. The study is necessary to ensure that the proper bias voltage is applied, keeping the detector running at highest efficiency. At the same time, the study shows how silicon sensors are degraded by radiation, and provides valuable input for the modelling and simulation of radiation damage. This analysis uses data taken at the beginning and the end of the run periods in 2016 and 2017, thereby allowing to investigate not only the degradation caused by continuous irradiation, but also the beneficial annealing process during the winter shutdown between the two years. Chapter 5 describes the method and the results.

Part I

Theoretical background

Chapter 2

The Standard Model

The theory formulating the present knowledge of particle physics is known as the Standard Model (SM). It is mathematically founded in the framework of quantum field theory, and adheres to the principle of *gauge invariance*, stating that the Lagrangian is invariant under phase (or gauge) transformations. Such a transformation, acting on a particle field ψ, can be written in a general form as

$$\psi(x) \rightarrow U\psi(x), \text{ where } U = \mathrm{e}^{ig\sum_{a=1}^{N}\alpha_a\chi_a}. \tag{2.1}$$

The exponent contains a sum over Hermitian operators χ_a, multiplied by continuous, real parameters α_a, which change the phase of the field by an equal amount at each point in space. The SM Lagrangian is however also invariant under gauge transformations that are *local*, meaning α_a can be a function of space-time, so that $U = U(x) = \mathrm{e}^{ig\sum_{a=1}^{N}\alpha_a(x)\chi_a}$. Noether's theorem gives that such a symmetry of the Lagrangian must imply a conserved quantity, in our case a charge. The dimensions and the properties of the transformation matrix U specify the symmetry groups of the theory. Unitary $N \times N$ matrices make a U(N) group, and if the matrices also have determinant +1, the group is SU(N). The interactions of the SM are invariant under the joint $\mathrm{SU}(3)_C \times \mathrm{SU}(2)_L \times \mathrm{U}(1)_Y$ gauge groups, where subscripts indicate the conserved charge: C for colour charge, L for left-handedness (chirality) and Y for hypercharge. Thorough reviews of the symmetries of the SM can be found in [1] and [2]. The following focusses on electroweak symmetry breaking and the need for the Higgs boson.

2.1 Electroweak theory

It is known from experiments that the weak interactions involve only left-handed fermion fields. The left- and right-handed components are projected out as

$$\begin{aligned}\psi^L(x) &= \frac{1}{2}(1-\gamma_5)\psi(x)\\ \psi^R(x) &= \frac{1}{2}(1+\gamma_5)\psi(x).\end{aligned} \tag{2.2}$$

The quantum number of the $\mathrm{SU}(2)_L$ gauge symmetry is the weak isospin I_a, where $a = 1, 2, 3$. Right-handed fermions have zero isospin, hence their transformation

under $SU(2)_L$ is trivial. The quantum number of the $U(1)_Y$ group is the weak hypercharge Y, which is related to the electric charge Q and the third component of the weak isospin through

$$Y = \frac{Q}{e} - I_3, \tag{2.3}$$

where e is the fundamental charge. Under the two gauge groups combined, the above fields transform as

$$\begin{aligned} \psi^L(x) &\to \exp[ig\frac{\sigma_a}{2}\alpha_a(x) + ig'Y\beta(x)]\psi^L(x) \\ \psi^R(x) &\to \exp[ig'Y\beta(x)]\psi^R(x), \end{aligned} \tag{2.4}$$

where g and g' are the coupling constants of $SU(2)_L$ and $U(1)_Y$ respectively, σ_a are the 2×2 Pauli matrices, and α_a, β are real, differentiable functions. As one can see, left- and right-handed fields transform equally under $U(1)_Y$, since the electromagnetic interaction does not distinguish between handedness. At this point the theory contains three massless Yang-Mills gauge fields, of which two are charged ($W^{\pm}$), while the neutral one can along with the single massless $U(1)_Y$ field be written as linear combinations of the physical fields Z^0 and γ. The mixing of the neutral fields is parametrised by the electroweak mixing angle θ_W. Quarks and leptons so far have to be massless too, since mass terms $m\bar{\psi}\psi = m(\bar{\psi}_L\psi_R + \bar{\psi}_R\psi_L)$ are not invariant under the transformations in eq. (2.4).

2.2 Spontaneous symmetry breaking and the Higgs mechanism

Since explicit mass terms are not gauge invariant, fermion masses must instead be generated. This can be achieved by introducing a doublet of scalar fields Φ,

$$\Phi(x) = \begin{pmatrix} \phi^+(x) \\ \phi^0(x) \end{pmatrix} \tag{2.5}$$

where ϕ^+ and ϕ^0 are both complex fields with nonzero isospin and hypercharge. This means that under $SU(2)_L \times U(1)_Y$, Φ transforms the same way as the left-handed field in eq. (2.4). The addition to the Lagrangian following the introduction of Φ is

$$\mathscr{L}_\Phi = (D_\mu\Phi)^\dagger(D^\mu\Phi) - V(\Phi), \tag{2.6}$$

where D_μ is the gauge covariant derivative, and V is the scalar potential,

$$V(\Phi) = \mu^2\Phi^\dagger\Phi + \lambda(\Phi^\dagger\Phi)^2, \ \lambda > 0. \tag{2.7}$$

In classical field theory, $\mu^2 > 0$ corresponds the potential energy surface shown in fig. 2.1a, which exhibits an absolute minimum at the origin. Upon quantisation, such a field would represent a charged scalar particle of mass μ, with a unique ground state with zero vacuum expectation value. In the case of $\mu^2 < 0$, on the other hand, the potential energy surface takes the form shown in fig. 2.1b, and has its minimum at $|\Phi|^2 = -\frac{1}{2}\mu^2/\lambda$. The vacuum state becomes degenerate, and the (arbitrary)

choice of direction in weak isospin and hypercharge space spontaneously breaks the $\mathrm{SU}(2)_L \times \mathrm{U}(1)_Y$ symmetry. The introduction of Φ adds four new degrees of freedom, where one corresponds to a real field $\sigma(x)$ which gives rise to a massive, electrically neutral spin-0 particle, the Higgs boson. The explicit appearance of the tree remaining ones can be removed by a gauge transformation, and are then absorbed into the longitudinal degrees of freedom of the $W^{\pm}$ and Z bosons, which thereby acquire masses. After this transformation into what is known as the *unitary gauge*, the Φ field takes the simple form

$$\Phi(x) = \frac{1}{\sqrt{2}} \begin{pmatrix} 0 \\ \upsilon + \sigma(x) \end{pmatrix}, \tag{2.8}$$

with $\upsilon = \sqrt{-\mu^2/\lambda}$. The masses of the $W^{\pm}$ and Z bosons are given by υ and the two coupling constants of $\mathrm{SU}(2)_L \times \mathrm{U}(1)_Y$,

$$m_W = \frac{1}{2} g^2 \upsilon, \quad m_Z = \frac{1}{2} \sqrt{g'^2 + g^2}\upsilon, \tag{2.9}$$

while the mass of the Higgs boson is

$$m_H = \sqrt{-2\mu^2} = \sqrt{2\lambda\upsilon^2}. \tag{2.10}$$

After electroweak symmetry breaking the fermions acquire masses through the coupling between the Higgs and the fermion fields. These Yukawa interactions, shown here for the tau lepton,

$$\mathscr{L} \supset -G_\tau \upsilon [\bar{\tau_R}(\Phi^\dagger \ell_L) + (\bar{\ell_R}\Phi)\tau_L], \quad \ell_L = \begin{pmatrix} \nu_\tau \\ \tau \end{pmatrix}_L, \ \Phi = \begin{pmatrix} \phi^+ \\ \phi^0 \end{pmatrix}, \tag{2.11}$$

are both renormalisable and invariant under $\mathrm{SU}(2)_L \times \mathrm{U}(1)_Y$ transformations. The interpretation of the coupling constant G_τ becomes more apparent in the unitary gauge form of Φ, where one obtains

$$\mathscr{L} \supset -(G_\tau \upsilon/\sqrt{2})\bar{\tau}\tau - (G_\tau/\sqrt{2})\sigma\bar{\tau}\tau. \tag{2.12}$$

The first part is recognisable as a mass term, and the prefactor can be rewritten as $\sqrt{2}m_\tau/\upsilon$. The coupling to the Higgs field then becomes

$$\mathscr{L} = -\frac{m_\tau}{\upsilon}\sigma\bar{\tau}\tau, \tag{2.13}$$

showing that the Higgs coupling is proportional to the fermion mass.

2.3 Higgs production

At the LHC, Higgs bosons can be produced through a number of different processes, the most important ones being gluon fusion, and vector boson fusion. Production cross sections for a 125 GeV Higgs boson at a center-of-mass energy of $\sqrt{s} = 13$ TeV are given in table 2.1.

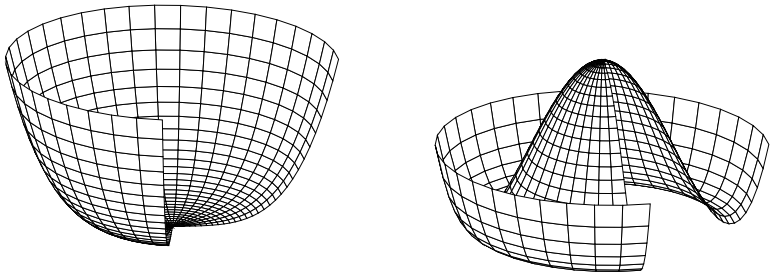

(a) $\mu^2 > 0$ (b) $\mu^2 < 0$

Figure 2.1: Illustration of the energy potential surfaces for positive and negative sign of μ^2.

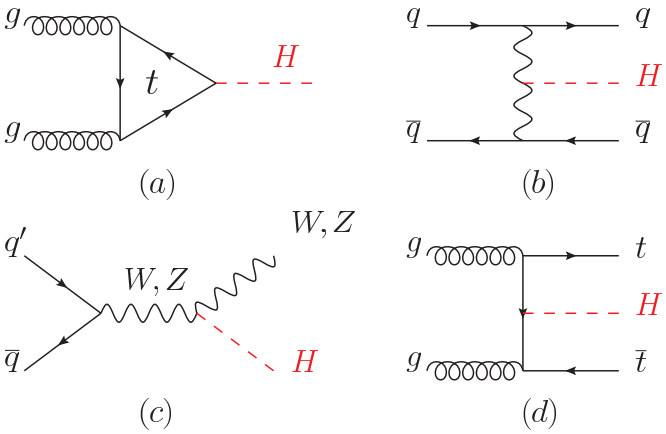

Figure 2.2: Feynman diagrams for the four most important Higgs production processes at the LHC. (a) Gluon-gluon fusion, (b) vector boson fusion, (c) W/Z-associated production, (d) $t\bar{t}$-associated production.

	ggF	VBF	WH	ZH	ttH	Combined
Predicted cross section	$48.6^{+5\%}_{-5\%}$	$3.7^{+2\%}_{-2\%}$	$1.37^{+2\%}_{-2\%}$	$0.88^{+5\%}_{-5\%}$	$0.5^{+9\%}_{-13\%}$	55.1
Measured signal strength μ	$1.3^{+0.16}_{-0.14}$	$1.18^{+0.25}_{-0.23}$	$0.89^{+0.40}_{-0.38}$	$0.79^{+0.38}_{-0.36}$	$2.3^{+0.7}_{-0.6}$	$1.09^{+0.11}_{-0.10}$

Table 2.1: Predicted cross section values, in pb, for different production processes. The values correspond to proton-proton collisions at a centre-of-mass energy of 13 TeV, for a 125 GeV Higgs boson. The measured signal strength μ gives the ratio of measured to predicted cross section; a value of $\mu = 1$ indicates full correspondence with the SM, while $\mu = 0$ would mean the process is not observed. The signal strengths values are the current world average numbers from the Particle Data Group (PDG) [3].

The gluon fusion (ggF) process, illustrated in fig. 2.2 (a), occurs through a loop exchange of virtual quarks. This will predominantly be the top quark, as the contribution is proportional to the square of the quark mass. Since this is a strong process there are significant radiative corrections; at next-to-leading (NLO) order, the diagram is augmented with real emissions of a gluon or a quark from one of the incoming gluons, or emission of a gluon from one of the internal quark propagators. These NLO corrections increase the cross section by approximately 80% [3], while NNLO corrections increase it even further by an additional 30%. This means a large part of Higgs bosons produced through ggF will be recoiling off one or several jets, providing a handle to separate such events from soft QCD background. The most recent cross section calculations are performed at N^3LO level [4].

Vector boson fusion (VBF) production, shown in fig. 2.2 (b), occurs through t- or u-channel exchange of W or Z bosons between two incoming quarks. The outgoing quarks form two jets, which are colour connected with the remnants of the colliding protons. This has two implications for the kinematics of the event; first, the two jets go predominantly in the forward and backward directions relative to the beam directions, and second, QCD radiation in the central direction is strongly suppressed. Although the VBF production cross section is ten times smaller than that of ggF, this clean signature makes it a highly sensitive process. Current VBF cross section numbers are calculated at NNLO for QCD and NLO for electroweak corrections.

The Higgs coupling to electroweak bosons are also involved in the W- and Z-associated production, shown in fig. 2.2 (c). The decay of the associated W/Z provides a signature for classifying this mode. As for VBF production, cross section calculations are available at NNLO for QCD and NLO for EW.

Besides ggF, the Higgs to top quark coupling comes into play in Higgs production associated with a $t\bar{t}$ pair, illustrated in fig. 2.2 (d). In addition to this diagram, one can also have s-channel $t\bar{t}$ production, where the Higgs is radiated off one of the top lines. The $t\bar{t}$- associated mode is of high interest since it allows for probing the top Yukawa coupling directly, exclusive of the loop effect in ggF. Cross section calculations have been performed at NLO level in QCD, with relatively high theoretical uncertainty, as can be seen in table 2.1.

2.4 Higgs quantum numbers

The Standard Model postulates the Higgs boson to be a CP-even scalar particle, $J^P = 0^+$. Since it has been observed to decay into pairs of photons, the Landau-Yang theorem states that it cannot have spin 1, but must have either spin 0 or 2. The spin 1 hypothesis has been excluded in decays to WW and ZZ too, at 99.999% confidence level (CL) [5]. Various graviton-like spin 2 modes have been tested, but are all excluded at 99% CL or higher by both ATLAS and CMS [5, 6]. The result from ATLAS is shown in fig. 2.3a.

The parity has been tested in WW and ZZ decays, both for fixed-parity state hypotheses $J^P = 0^+$ and $J^P = 0^-$, and for mixed states. In the fixed-parity scenario, studies of $H \to ZZ$ decays exclude the pure pseudoscalar hypothesis at 99.98% CL. The only remaining possibilities for non-SM properties lie in the couplings. Anomalous couplings to fermions can be probed either in $t\bar{t}H$ production or in H decays to

$b\bar{b}$ or $\tau\bar{\tau}$[1], none of which have been performed so far. Prospects for investigating possible *CP*-violating effects in decays to $\tau\tau$, are discussed in part III. The couplings to gauge bosons have been tested by both ATLAS and CMS, by parametrising the interaction in form of an effective field theory, where the Lagrangian under the spin 0 hypothesis is given by [7]

$$\begin{aligned}\mathscr{L}_0^{W,Z} =& \Big\{ \cos(\alpha)\kappa_{\mathrm{SM}}\big[\frac{1}{2}g_{HZZ}Z_\mu Z^\mu + g_{HWW}W_\mu^+ W^{-\mu}\big] \\ &- \frac{1}{4\Lambda}\big[\cos(\alpha)\kappa_{HZZ}Z_{\mu\nu}Z^{\mu\nu} + \sin(\alpha)\kappa_{AZZ}Z_{\mu\nu}\tilde{Z}^{\mu\nu}\big] \\ &- \frac{1}{2\Lambda}\big[\cos(\alpha)\kappa_{HWW}W_{\mu\nu}^+ W^{-\mu\nu} + \sin(\alpha)\kappa_{AWW}W_{\mu\nu}^+ \tilde{W}^{-\mu\nu}\big]\Big\} X_0.\end{aligned} \tag{2.14}$$

This equation will not be discussed in too much detail, apart from the coupling constants κ_{SM}, κ_{HVV} and κ_{AVV}, which correspond to the ZZ and WW couplings to a SM boson, a BSM *CP*-even boson, and a BSM *CP*-odd boson, respectively. Non-zero values of κ_{HVV} and κ_{AVV} would indicate the presence of additional Higgs bosons; values of the *CP* mixing angle $\alpha \neq 0, \pi$ would indicate mixing between them. No indication of new physics has so far been observed. Combined $H \to ZZ$ and $H \to WW$ results from ATLAS Run-1 data are shown in fig. 2.3b and fig. 2.3c. Updated $H \to ZZ$ results with Run-2 data can be found in [8] and [9].

[1] For shorthand the bar will be omitted ($\tau\tau$) in the following.

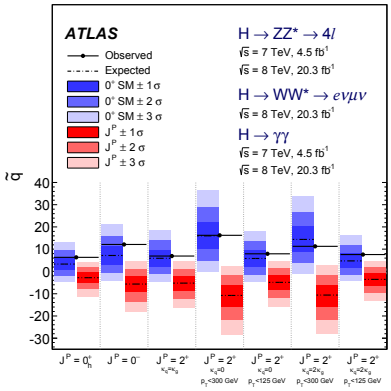

(a) Expected and observed distributions of the test statistic for the SM, in blue, and alternative J^P scenarios, in red.

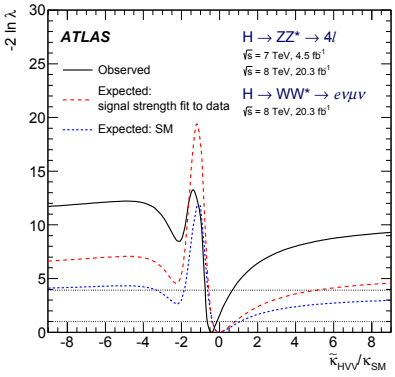

(b) Likelihood profile for the BSM *CP*-even coupling constant κ_{HVV} divided by the SM coupling constant κ_{SM}

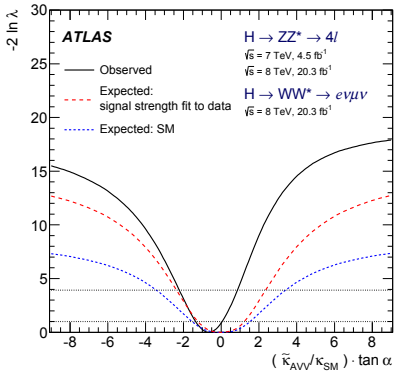

(c) Likelihood profile for the BSM *CP*-odd coupling constant κ_{AVV} divided by the SM coupling constant κ_{SM}, multiplied by the tangent of the *CP* mixing parameter α.

Figure 2.3: Results from analysis of alternative J^P scenarios and of anomalous couplings in $H \to ZZ^* \to 4\ell$, $H \to WW^* \to e\nu\mu\nu$ and $H \to \gamma\gamma$ decays [6].

Part II

The ATLAS detector

Chapter 3

The ATLAS experiment

3.1 CERN and the Large Hadron Collider

Located at the French-Swiss border just outside of Geneva, the European Organization for Nuclear Research (originally *Conseil Européen pour la Recherche Nucléaire* — CERN) is one of the leading laboratories for high-energy particle and nuclear physics. Founded in 1954, it has been the site of several major discoveries, among those the discovery of neutral currents (1973), the W and Z bosons (1983), direct CP violation (1999), and most recently, the Higgs boson (2012). The long history of accelerator development plays an important role in the modern-day operation of the experimental facilities at CERN — not only through accumulation of knowledge, but also in a more direct way, since the old circular colliders are being used as intermediate accelerators for the currently most powerful machine, the Large Hadron Collider (LHC).

3.1.1 The LHC

The LHC is a 27 km long circular proton-proton collider, designed for delivering collisions at a center-of-mass energy $\sqrt{s} = 14\,\text{TeV}$. The first beams were brought into orbit in 2008, but due to a technical malfunction causing severe damage to several of the superconducting bending magnets, the start of the first stable physics run was delayed until 2010. In the period from 2010 to 2013, referred to as Run 1, the LHC was operating at a collision energies of 7 and 8 TeV. Following a period of upgrades and maintenance, the Long Shutdown 1 (LS1), operation was continued in 2015 at $\sqrt{s} = 13\,\text{TeV}$. The first period of the second proton run, Run 2, was closed at the end of 2017.

3.2 The ATLAS experiment

The ATLAS (A Toroidal Lhc ApparatuS) detector, with a length of 44 m, diameter of 25 m, and an overall weight of around 7000 tons, is the largest of the LHC experiments. Named after its characteristic toroidal magnets surrounding the muon spectrometer, ATLAS is a multipurpose detector designed for making high-precision

measurements, under the radiation intensive conditions provided by the LHC. A cut-out overview is shown in fig. 3.1.

Coordinate system and common observables

The ATLAS coordinate system is defined with the nominal interaction point as the origin, where the x-axis points inwards to the centre of the LHC ring, and the y-axis points upwards. The system is right-handed, so that the z-axis goes along the beam line, in the counter-clockwise direction. Usually, cylindrical coordinates are used, with ϕ being the azimuthal angle around the z-axis, and θ the polar angle. Rather than the polar angle, a more convenient observable is the *pseudorapidity* η, defined as $\eta \equiv -\ln\tan(\theta/2)$. Under the assumption of particles moving at relativistic speeds (i.e. $p \approx E$), differences in pseudorapidities are Lorentz invariant under boosts along the z-axis. Observables defined in the transverse (x-y) plane are denoted by a subscript T, such as transverse momentum $p_{\mathrm{T}} \equiv p\sin\theta$ and transverse energy $E_{\mathrm{T}} \equiv E\sin\theta$. The angular distance between objects, ΔR, is defined as $\Delta R \equiv \sqrt{(\Delta\eta)^2 + (\Delta\phi)^2}$.

3.3 Layout of the ATLAS detector

3.3.1 Inner detector

Responsible for measuring particle momenta and vertex positions, the inner detector consists of three subsystems: the Pixel detector, the SemiConductor Tracker (SCT) and the Transition Radiation Tracker (TRT). The placement of the different subsystems is shown in fig. 3.2.

Pixels and the IBL

Arranged in four concentric cylinders around the beam pipe and three disks in each of the endcaps, the pixel detector is designed with high granularity in mind. The innermost barrel layer, the Insertable b-Layer (IBL), was installed during Long Shutdown 1. The three original layers are typically just referred to as 'pixels', and consist of in total 1744 modules, each with external dimensions of $19 \times 63\,\mathrm{mm}^2$. The sensors themselves are 250 µm thick, with nominal pixel size of $50 \times 400\,\mu\mathrm{m}^2$. The bulk material of the sensor wafer is oxygenated n-type silicon, with n^+ implants on the readout side, and p^+ regions on the back side, where the reverse bias is applied. This design is chosen to ensure high charge collection efficiency even after prolonged irradiation; see chapter 5 for further discussion about the effects of radiation damage. Each pixel module is assembled from 16 front-end electronics chips bump-bonded to the sensor. The front-end chips, type FE-I3 [11], amplify the sensor charge signal and digitise it in form of Time over Threshold (ToT), i.e. the time during which the signal amplitude is higher than the discriminator setting, measured in number of bunch crossings. Each individual front-end reads out signals for pixels arranged in 18 columns (along ϕ) and 164 rows (along η), which is forwarded to the Module Control Chip (MCC), located at the other side of the sensor wafer. The MCC formats and

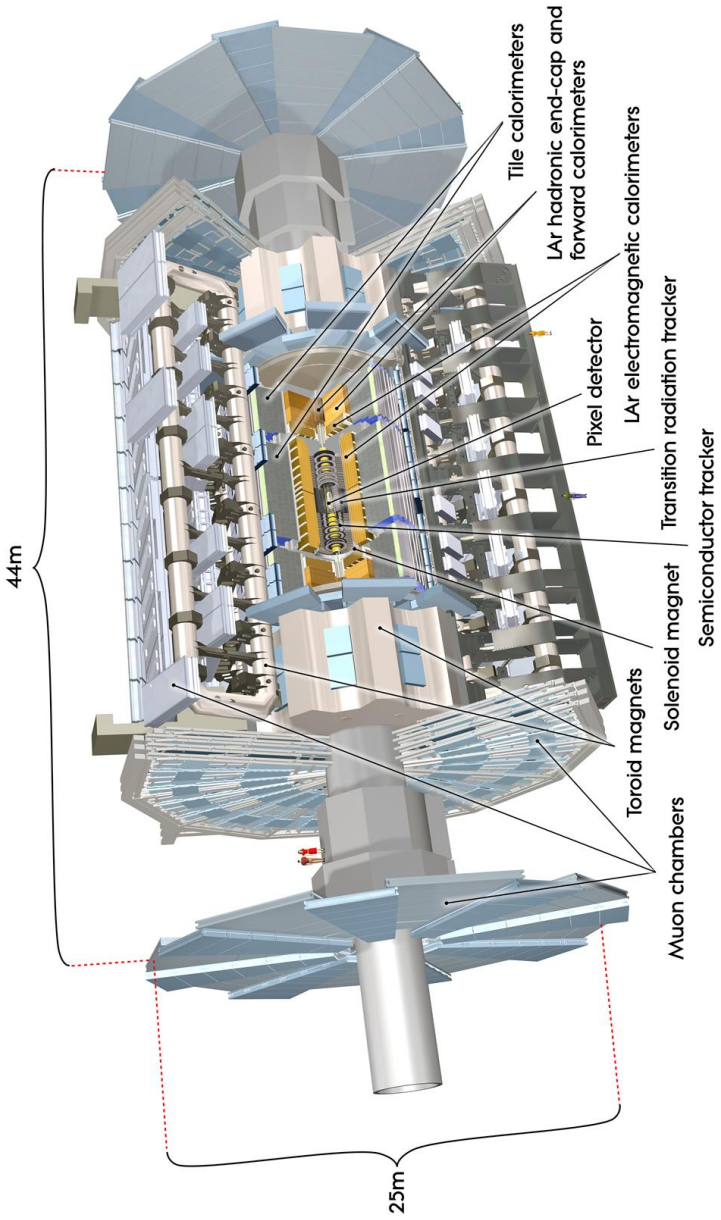

Figure 3.1: Overview of the ATLAS detector, showing the main detector components. The large toroid magnets surround the inner detector and the calorimeters, and the muon chambers are partly embedded inside them. The detector is situated in a cavern 100 m under ground. Graphic from [10].

transmits digital data, so-called bytestream data, to the off-detector readout electronics. In total for the three pixel layers, approximately 80 million individual channels are read out.

An additional 12 megapixels are provided by the IBL, which was installed between the innermost pixel layer and a new, smaller beam pipe in 2014. This layer features two different types of pixel technologies; out of 20 modules per stave, the 12 center modules have planar pixel sensors, while the 4 outermost modules on each side use 3D sensors. Both sensor types have a pixel size of $50 \times 250\,\mu\text{m}^2$, and are read out by a new, more radiation-hard front-end chip, named FE-I4B. The pixel configuration read out by each front-end consists of 336 columns and 80 rows.

The planar sensors have a surface of $41 \times 19\,\text{mm}^2$ and are 200 µm thick. One such sensor is read out by two front-ends, while the 3D sensors are half the surface area and 230 µm thick, and read out by a single chip. The 3D technology involves etching microscopic holes in the silicon wafer, from both sides; on the readout side, the columns are n^+ type, while the back side they are p^+. This technique allows for a shorter inter-electrode distance than for planar sensors, which lowers the voltage required for depleting the sensor, which in turn makes the sensor perform well after heavy irradiation [12]. This motivates the choice of 3D technology for the high pseudorapidity regions.

SemiConductor Tracker (SCT)

The SCT is a silicon microstrip detector, consisting of four layers in the barrel, and nine disks in each of the endcaps. The layers are arranged so that any track within the η coverage should pass through four sensors. The modules are double-sided, mounted with a stereo angle of 40 mrad, which give a position resolution along the strip direction of 580 µm. Along the perpendicular direction, the resolution is 17 µm. The number of readout channels is approximately 6.3 million.

Transition Radiation Tracker (TRT)

Consisting of 4 mm diameter gas-filled straw tubes, interleaved with radiation foils, the TRT offers both position measurements and electron identification. The straws are parallel with the beam axis in the barrel region, and extend radially in the endcaps. Although the position resolution is significantly lower than for the silicon systems, the TRT sees a large number of hits per track (36, on average), which makes an important contribution to tracking. While charged particles traversing the straws ionise the gas directly, considerably stronger ionisation can occur due to transition radiation, an effect caused by the change in dielectric constant seen by a particle crossing the tube boundary. Since the radiation intensity is proportional to the Lorentz factor γ, electrons can be separated from heavier particles, which radiate less. The total number of readout channels is approximately 351 000.

3.3.2 Calorimeters

The ATLAS calorimeters, all of the sampling type, using alternating layers of active and passive material, are assembled from five major subsystems. The electro-

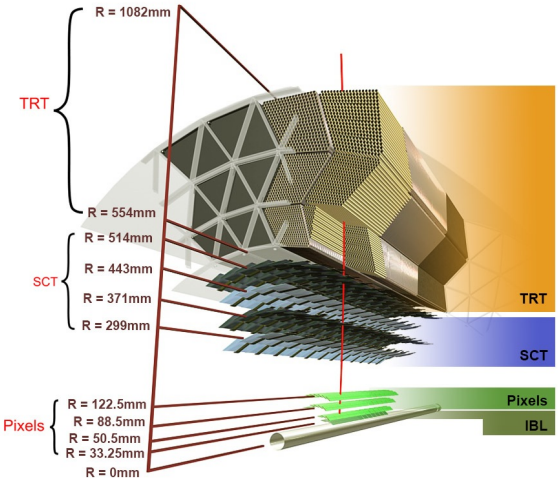

Figure 3.2: Cut-out view of the inner detector, showing at increasing radius the beam pipe, the IBL and pixel layers, the SCT, and finally the TRT. Graphic from [13].

magnetic calorimeter, consisting of barrel and endcap parts, uses liquid argon and accordion-shaped lead absorber plates. The coverage goes up to $|\eta| < 3.2$, although the resolution is best in the region $|\eta| < 2.5$. Since the electromagnetic calorimeter is situated downstream of the solenoid magnet, a single, thin liquid Ar layer is placed in front of the solenoid and serves as a presampler to correct for energy lost in the front of the calorimeter. The total thickness of the EM calorimeter ranges from > 22 radiation lengths in the barrel, to > 24 radiation lengths in the endcaps.

Directly outside of the EM calorimeter sits the hadronic calorimeter, which in the barrel region is constructed using plastic scintillators and steel absorber plates. This covers the region up to $|\eta| = 1.7$. The endcap sections, extending to $|\eta| = 3.2$, use liquid Ar as active material, in conjunction with copper absorber plates. The thickness of the hadronic calorimeter corresponds to approximately 10 interaction lengths, meaning there is little leakage, or 'punch-through', which is important for reconstruction of energetic jets. In addition, to ensure maximal hermeticity of the detector, a liquid argon forward calorimeter provides coverage up to $|\eta| = 4.7$. This subsystem uses a combination of copper and tungsten absorber plates, and is of high importance for reconstruction of very forward jets.

3.3.3 Muon spectrometer

The muon spectrometer employs four different detector technologies, put together to provide both precision measurements, and fast triggering. It is essentially built into the toroid magnet system, which bends tracks in the R-z-plane. The main technology used for tracking is Monitored Drift Tubes (MDT), which are 30 mm diameter gas-filled tubes, covering the pseudorapidity range up to $|\eta| < 2.7$. In the endcaps, MDTs are supported by segmented multiwire proportional chambers called Cathode Strip Chambers (CSC), which have higher rate capabilities. The muon trigger system is operated using a combination of resistive plate chambers in the barrel, and thin

multiwire proportional chambers in the endcaps. In addition to triggering, these systems also measure track coordinates in the non-bending (ϕ) direction, orthogonal to that of the MDTs and CSCs.

3.3.4 Magnet systems

The magnet system in ATLAS consists of the barrel solenoid, the barrel toroid, and two endcap toroids, all superconducting and operating at 4.6 K. The solenoid generates a 2 T magnetic field parallel to the beam axis. Since the coils are placed in front of the EM calorimeter, they were engineered with minimal thickness in mind; at normal incidence, the assembly corresponds to around 0.66 radiation lengths. The toroid systems feature eight coils each, providing a field of 0.5 to 1.0 T, depending on position. Mapping and continuous monitoring of the magnetic field is done using Hall effect sensors distributed around the detector volume.

3.3.5 Event triggering

Interesting collision events are selected by the trigger system, which is divided in two stages. The first stage, the Level 1 Trigger (L1), is implemented in the detector hardware and uses information from the calorimeter and the muon spectrometer to provide a rough identification of high-p_{T} jets, taus, and other objects. The L1 trigger reduces the initial event rate from 40 MHz (one collision every 25 ns) to approximately 100 kHz [14]. Events passing this step are then evaluated by the High-Level Trigger (HLT), which is software based, and reconstructs objects using the full detector information. Different triggers [15] target different types of events, depending on the presence of for instance large missing transverse energy, or certain objects of interest. The HLT further reduces the event rate to around 1 kHz. While awaiting the L1 trigger decision, which has a fixed latency of 2.5 µs, the detector output is buffered in the individual modules. The HLT has an average latency of 350 ms before reaching the decision to store or reject the event.

3.4 Event reconstruction

Collision events passing the trigger selection, are written to disk for offline processing. Reconstructed entities like tracks, jets and taus are collectively referred to as *objects* and are defined by criteria provided by dedicated performance working groups in ATLAS.

3.4.1 Tracks

Charged-particle trajectories are reconstructed starting from three hits in the pixel and SCT detectors. In the pixel layers, a traversing particle typically deposits energy in multiple pixel cells, which are clustered together to form a hit. The charge collection in each individual pixel is used to estimate the position of the track through the cluster, by computing the 'centre of gravity' of charge contributions to the cluster. In the SCT, clusters of strips are formed, but both sides of the layer must be combined

to form a point in three-dimensional space. Three compatible space-points make up a track seed, which enter into an iterative combinatorial track finding. The procedure attempts to add additional hits from the remaining silicon layers, potentially creating multiple track candidates, in case several compatible hit combinations are found. Each candidate is assigned a track score, computed based on quality criteria such as fit quality and cluster properties, which is used to solve ambiguities [16].

3.4.2 Vertices

The position of proton interactions is computed by fitting tracks to a common vertex. The process starts from a seed position, determined in the transverse plane by the beam spot, and in the z direction by the mode of z-coordinates of tracks passing a quality selection. In an iterative procedure, a χ^2 fit is performed, and each track is assigned a weight corresponding to how well the track parameters match the vertex position. Using the weighted tracks, the fit is performed again, and the track weights are updated to reflect the new vertex position. After the last iteration, any track falling outside the vertex position by more than seven standard deviations, are removed from this vertex candidate and used to seed a new vertex. A vertex candidate is retained if it contains at least two tracks. The distribution of the number of vertices per bunch crossing in Run 2 is shown in fig. 3.3, and as indicated on the plot, the average value for 2015 and 2016 data combined is 23.7. The vertex with the highest sum of squared track p_{T} is selected as the primary (or hard-scattering) vertex, while all other vertices are attributed to pile-up.

The distance of closest approach between a track and the reconstructed vertex, called the impact parameter, is computed in the transverse and longitudinal directions and denoted d_0 and z_0, respectively. Tracks originating from secondary decay vertices, such as from tau or b-quark decays, typically have large impact parameters, which will be shown in section 6.2 to be of importance for inferring the polarisation directions. The impact parameter resolution decreases with track p_{T}, while increasing with higher $|\eta|$ [17].

3.4.3 Jets

Being segmented in both the lateral and longitudinal direction, the calorimeters can reconstruct particle showers in three dimensions, known as topological clusters. If the energy deposit in a cluster corresponds to a p_{T} greater than 7 GeV, the jet is reconstructed using the anti-$\mathrm{k_T}$ algorithm [19], with a distance parameter of $R = 0.4$. The calorimeter cell energy is initially calibrated to the electromagnetic scale, i.e. the energy deposit of electromagnetically interacting particles. Taking into account tracks associated with the jet, the final calibration is derived using a combination of simulation and *in situ* methods [20]. The latter uses data from well-known processes such as Z boson decays. The calibration affects the reconstruction performance via two parameters: the jet energy scale, which relates the calorimeter response to the true jet energy, and the jet energy resolution. Both depend on the jet p_{T} and pseudorapidity.

To suppress pile-up jets, a Jet Vertex Tagging (JVT) algorithm [21] is used to identify jets which originate from the primary vertex. For very forward jets ($\eta >$

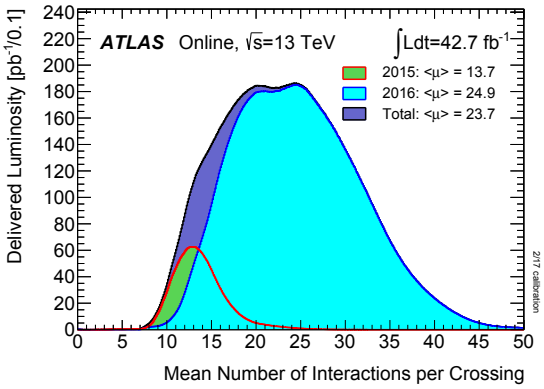

Figure 3.3: Luminosity-weighted distribution of the mean number of interactions per bunch crossing in 2015 (green) and 2016 (light blue) data. The dark blue curve shows the combination of the two. Plot taken from [18].

2.4), a separate forward-JVT tool [22] is used. Identifying such jets is important for reconstructing events with a Higgs boson produced via vector boson fusion.

3.4.4 Electrons and muons

Electrons are reconstructed by combining inner detector tracks with energy deposits in the EM calorimeter. The track quality and the shape of the EM shower is used to determine the identification quality. Likewise for muons, the reconstruction combines inner detector tracks with tracks in the muon spectrometer. In the following analysis, electrons and muons are only used as input to the calculation of missing energy, and to veto events containing non-tau leptons.

3.4.5 Missing transverse energy

The missing transverse energy, $E_{\mathrm{T}}^{\mathrm{miss}}$, denotes the momentum imbalance in an event, measured in the transverse plane. It is calculated as the negative momentum sum of all reconstructed and calibrated objects seen in the event,

$$\boldsymbol{E}_{\mathrm{T}}^{\mathrm{miss}} = -\sum \boldsymbol{E}_{\mathrm{T}} = -(\boldsymbol{E}_{\mathrm{T}}^{e} + \boldsymbol{E}_{\mathrm{T}}^{\gamma} + \boldsymbol{E}_{\mathrm{T}}^{\tau} + \boldsymbol{E}_{\mathrm{T}}^{\mathrm{jets}} + \boldsymbol{E}_{\mathrm{T}}^{\mathrm{SoftTerm}} + \boldsymbol{E}_{\mathrm{T}}^{\mu}). \tag{3.1}$$

The 'soft term' corresponds to inner detector tracks originating from the primary vertex, which are not associated to any reconstructed object [23]. The magnitude of $E_{\mathrm{T}}^{\mathrm{miss}}$ is used to select boosted tau pairs, since the neutrinos from the tau decays can carry off significant momentum, and is also used as input for the ditau mass reconstruction, discussed in section 6.2.4.

3.4.6 Taus

With a mean flight path of 87.03 μm [3], taus typically decay inside the beam pipe, making its reconstruction considerably harder than for the other leptons. 35% of

Table 3.1: Branching ratios of important hadronic tau decay modes [3]. The h indicates a charged hadron, which can be either a $\pi^{\pm}$ or a $K^{\pm}$. All decays involve a ν_τ, which is not written explicitly.

Decay mode	Brancing ratio
$h^{\pm}$	$11.51 \pm 0.05\%$
$h^{\pm}\pi^0$	$25.93 \pm 0.09\%$
$h^{\pm} \geq 2\pi^0$	$10.81 \pm 0.09\%$
$3h^{\pm}$	$9.80 \pm 0.05\%$
$3h^{\pm} \geq 1\pi^0$	$5.09 \pm 0.05\%$

decays are leptonic ($\tau \rightarrow \ell\bar{\nu}_\ell\nu_\tau,\ \ell = e,\mu$), while the remaining involve hadronic decay products. Of the latter, five dominant decay modes make up over 90% of the branching ratio. These involve either one or three charged hadrons, typically called *prongs*, and are listed in table 3.1. The following analysis considers only hadronically decaying taus (τ_{had}).

The reconstruction starts with topological calorimeter clusters, from which jets are constructed, as usual with radius parameter $R = 0.4$. For a jet to be considered as a τ_{had} candidate, it must first satisfy $p_{\text{T}} > 10\,\text{GeV}$ and $|\eta| < 2.5$. Before computing the momentum vector of the candidate, a tau production vertex is assigned, based on the tracks within $\Delta R < 0.2$ of the jet seed direction. The τ_{had} direction can now be determined by the tau production vertex and the cluster barycentre, and tracks are assigned to the candidate if they lie within the *core region* $R = 0.2$ of the candidate direction, and satisfy quality requirements [24]. The complete τ_{had} 4-momentum is constructed from clusters within the core region. To account for differences in energy calibration between QCD jets and taus, a tau energy scale correction is applied.

Separation of taus from QCD jets is done by Boosted Decision Trees (BDTs) [25], operating on various observables oriented around jet shape and energy deposition ratios. Three identification working points are provided, determined from the BDT score and the p_{T}, so that the combined reconstruction and identification efficiency is approximately constant as function of p_{T} for a given working point. These are named *loose*, *medium* and *tight*, in order of increasing background rejection. The combined signal efficiencies are, in the same order, 0.6 (0.5), 0.55 (0.4) and 0.45 (0.3) for 1-prong (3-prong) taus.

At this point, a novel algorithm introduced in Run 2 called tau particle flow [26] (or tau substructure algorithm — a pet child has many names), further refines the τ_{had} candidate by reconstructing its individual charged and neutral components. Access to the π^0 4-momentum is vital for the reconstruction of the tau decay plane, as will be discussed in section 6.2.

π^0 reconstruction

Practically all neutral pions decay to a pair of photons; of these photons, around half of them convert to e^+e^- pairs due to interactions with detector material in front of the calorimeter. EM calorimeter clusters in the core region around the τ_{had} form the starting point of the π^0 reconstruction. The energy deposit is corrected for contami-

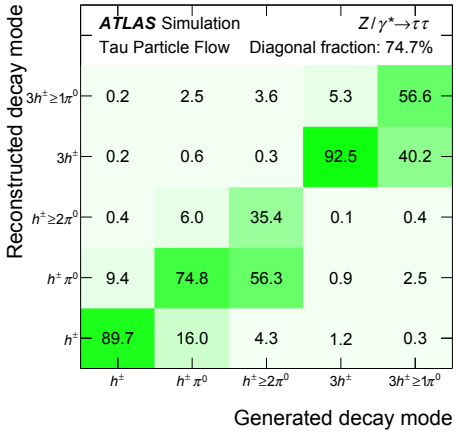

Figure 3.4: Decay mode classification efficiency in simulated $Z \to \tau\tau$ events, showing the fraction of how often a given generated decay mode is reconstructed as a certain mode. Plot taken from [26]

nation from charged hadrons, and a minimum p_{T} requirement is imposed, in order to reduce contributions from pile-up and calorimeter noise. The remaining background is mainly from charged hadrons. The π^0 identification decision is based on the score from a BDT trained on observables like shower shape and energy density, where the decision threshold is optimised in five $|\eta|$ intervals, corresponding to structurally different calorimeter regions.

Decay mode classification

Rather than simply counting the number of reconstructed charged and neutral hadrons, several BDTs are employed to classify the decay mode, taking the kinematics of the decay as input. π^0's from a real tau decay are correlated both in energy and direction, hence the multivariate approach can more effectively assign the π^0 multiplicity instead of using the π^0 identification score alone. The classification efficiency is illustrated in the matrix in fig. 3.4, showing that the probability of correctly classifying one-prong decays with zero or one π^0, is 90% and 75%, respectively. Effects from pile-up are shown to have minimal impact on the classification, degrading it by approximately 0.04% per additional vertex in the event.

4-momentum reconstruction

The τ_{had} four-momentum is computed by summing the momenta of the individual tracks and π^0 candidates, and calibrating the energy using calorimeter information. This calibration is most important at high transverse energies, where the decay products are highly collimated and the π^0 energy deposits cannot be separated. The particle flow and calorimeter information is combined by a regression BDT trained on simulation, a calibration known as MVA TES.

The most vital element for the particle flow method is, however, the angular resolution, which is significantly improved with respect to a calorimeter-only approach. This does in turn improve the ditau mass resolution. Further, access to the individual π^0 4-momenta is essential for the study of the Higgs *CP* properties. The particle flow reconstruction is stable in the presence of pileup; the τ_{had} angular resolution degrades by $\sim$ 0.5% per additional reconstructed vertex, while the transverse energy resolution increases by $\sim$ 4 MeV per additional vertex.

3.4.7 Overlap removal

In the case where two or more objects are geometrically overlapping, the identification ambiguity is resolved by keeping only the object of which the identification is most certain. This means retaining the first object in the following order of priority: muons, electrons, taus, and lastly jets. The overlap criterion depends on the type of object. Electrons are excluded if within $\Delta R < 0.2$ of a muon, and similarly, τ_{had} candidates are excluded if within $\Delta R < 0.2$ of an electron of a muon. Jets are excluded if within $\Delta R < 0.2$ of a τ_{had}, or if within $\Delta R < 0.4$ of an electron or muon.

Chapter 4

Bytestream converter software

Algorithms and tools for event reconstruction are implemented in the ATHENA framework [27], an ATLAS-specific variant of the general GAUDI framework [28]. The reconstruction code is divided into separate packages, which can roughly be classified as algorithms, which operate on data objects to produce higher-level output, and services, which perform some common task that one or several algorithms may need. The core of the bytestream converter software resides in the `PixelRawDataByteStreamCnv` package, while the `PixelCabling` service provides the mapping from local pixel module coordinates to the global ATLAS-wide coordinate system. This software is run both offline, i.e. when reconstructing previously recorded data, and online, in real-time as the detector is taking data, in order to provide input to the trigger software.

The raw data output from the detector is written in a module-dependent binary format, known as *bytestream* data. The bytestream data is organised into blocks of data called fragments, containing the output from a readout unit. The beginning of a fragment is indicated by a header, a 32-bit block identifying the type and properties of the fragments to follow. These 32-bit blocks are the minimum quanta of bytestream data, and are typically referred to as 'words'. Each header has a generic part, which is structurally identical all across the types of fragment, and a fragment specific part, which can include information applicable only to a specific subsystem. The fragments are divided into five types of progressively lower subsystem level, where a given fragment type is essentially an aggregation of the lower-level fragments from this subsystem. The highest level is the event fragment — all recorded detector data from one event is contained within this. It is divided into subdetector fragments, which is further divided into Read-Out Subsystem (ROS) fragments, divided again into Read-Out Buffer (ROB) fragments. The final ATLAS-general fragment type is the Read-Out Driver (ROD) fragment [29]. The contents of the data elements contained within ROD fragments are purely specific to the detector subsystem that they originate from. In fact, due to the difference of the FE-I3 and the FE-I4B, the content of the pixel ROD fragment is dissimilar between the IBL and the existing pixel layers — hence the software that interprets the data must be capable of switching between two different binary formats.

Interaction with the bytestream format is a two-way process. The converter software does the decoding part, translating the raw detector output into offline data objects, but also the reverse operation of encoding offline data into raw data. The lat-

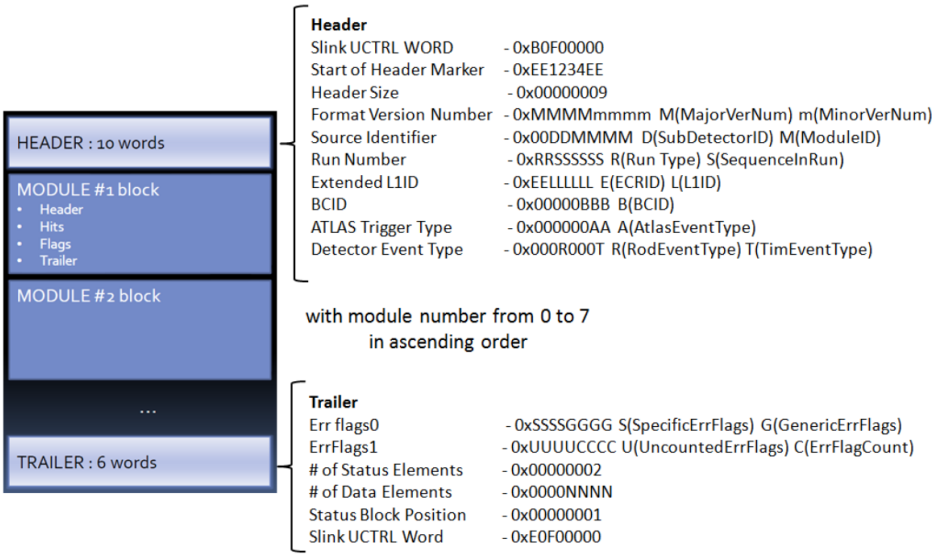

Figure 4.1: Schematic of the ROD fragment format [31]. See text for description.

ter is performed during detector simulation of Monte Carlo (MC) events, to emulate the input to the trigger software.

4.0.1 ROD fragment format

The lowest unit of detector-wide standardised fragments is the ROD fragment, shown in fig. 4.1. The start-of-header marker, identifying the beginning of a ROD header, is always 0xEE1234EE. The next words indicate the header size and version, followed by the source identifier, which is composed of the subdetector and module identifier numbers. A subdetector ID of 0x11 corresponds to barrel layers 1 and 2, 0x12 corresponds to the disks, while 0x13 to the *b*-layer. ID 0x14 is given to both the IBL and the Diamond Beam Monitor (DBM) [30], which both use FE-I4B sensors. The module identifier equals the ROB ID. The task of translating the source identifier into the physical position of the module that sent the fragment, is done by the `PixelCabling` service. The subsequent fields of the ROD header (run number, Level 1 ID, bunch crossing ID) give the timestamp of the event, while the trigger type field gives trigger information, and the event type field allows for additional information mainly related to calibration.

The ROD header is followed by module blocks, containing data from each sensor; the specific format of the module blocks is discussed in the next section. The ROD trailer closes off the fragment, and contains error flags and counters for the number of status elements (equals number of error flag words, always two) and number of module blocks.

4.1 FE-I4B fragment format

The format of the pixel and IBL module blocks contained within the ROD fragment is entirely module specific, and is decided by firmware developers. The differences in arrangement and features of the new FE-I4B chip compared to the FE-I3 called for a new format to be developed, which has been continuously updated over the commissioning period of the IBL. A noticeable difference in the transmission of hit data is the absence of an MCC on the IBL modules; each IBL front-end communicates hit data to the ROD directly. The FE-I4B module format is listed in table 4.1, while the FE-I3 format is for reference shown in fig. A.1. The general structure of data enclosed within a header and a trailer applies to both, but the format itself differs. The identity of the front-end is given by the five `nnnnn` bits, indicating the link number. The two most significant bits (in little-endian format) give the Slink number, while the remaining three give the front-end number within the Slink. More details on the orientation of this numbering is given in section 4.1.3. The header further provides the Level 1 and bunch crossing IDs.

Table 4.1: FE-I4 module fragment format, up to date as of 2017.

Module block	data_out[31:0]
header	`001nnnnnFLLLLLLLLLLLLLBBBBBBBBBB`
hit (long)	`100nnnnnTTTTTTTTCCCCCCCRRRRRRRRR`

hit (condensed)	`101RRRRRTTTTTTTTCCCCCCCRRRRRRRRR`
	`1CCCRRRRRRRRRTTTTTTTTCCCCCCCRRRR`
	`1TTTCCCCCCCRRRRRRRRRTTTTTTTTCCCC`
	`111TTTTTTTTCCCCCCCRRRRRRRRRTTTTT`

FE flag error	`000nnnnnnxSSSSSSxxxxxxxDDDDDDDDDD`
trailer	`010nnnnnEcPplbzhvMMMMMMMMMMBBBBB`

`n`: link number	`F`: FE-I4B flag bit	`L`: L1ID
`B`: BCID	`R`: row	`C`: column
`T`: hit ToT	`x`: unused	`S`: service code
`D`: service code counter	`E`: readout timeout error bit	`c`: condensed mode bit
`P`: link masked by PPC	`p`: preamble/header error	`l/b`: L1ID/BCID error
`z`: trailer timeout error	`h`: header/trailer limit error	`v`: row/column error
`M`: skipped trigger counter		

The FE-I4B features two protocols for transmitting hit data. The first is a 'long' hit, where one 32-bit word is used to communicate the position of a single hit. The word is identified by the most significant bits being 0x100, followed by link number (`n`), ToT (`T`), column (`C`) and row (`R`) information. The column and row numbering starts at (1,1), in the the upper left corner of the sensor [32]. The columns go along the global ϕ direction and range from 1 to 336 inclusive, while the rows go up to 80. The second hit data protocol is the *condensed* mode, which allows for the information in five long hit words to be compressed into four, thereby saving 32 bits. Reducing the bandwidth usage is a concern for the IBL, to avoid overflowing the readout buffer

in events with high track multiplicities.

The front-end *flag error* block contains FE-I4B service codes (S), and a 10-bit payload (D). The service codes range from 0 to 31, indicating different types of error reported by the front-end. The full list of service codes is given in [32]. For all codes except 14, 15 and 16, the payload is a counter, which adds up the number of times an error has occured. This counter is reset once the service code is read out. The payload of the special codes 14–16 contain information on skipped triggers and event truncation.

The module trailer contains an aggregation of error codes reported by the ROD. The readout timeout error (E) indicates that the module did not send its data within the maximum allowed time after a L1 trigger signal. The ROD still inserts a header-trailer pair for unresponsive modules, but it will necessarily not enclose any data, and the E bit is set. In addition, the least significant bits of both the header and trailer are set to 0x000BAD. The condensed mode bit (c) is set if the module data is encoded in condensed mode; the decoder software does however not rely on this to correctly identify and process condensed hit words, it is merely implemented as a cross-check. The P bit indicates that this particular front-end is masked off by the ROD software. The preamble/header error (p) bit is set if the ROD receives an ill-formatted header from the front-end. The l and b bits indicate errors with the L1ID and BCID counters, respectively. The z bit is set in case the ROD did not receive a module trailer within a certain time limit, similarly as for the E error; in this case the ROD inserts a generic trailer. To limit the amount of data placed in the link buffers, a threshold can be applied, forcing the ROD to stop outputting data beyond the limit. The h bit will then signal that the limit was reached. The v bit indicates row or column error, while the 10-bit M field is the skipped trigger counter. This counter adds up the number of times an L1 trigger was ignored because the front-end buffer was full. The final five B bits of the trailer is just a repetition of the five least significant bits in the BCID.

4.1.1 FE-I4B Time-over-Threshold (ToT) values

The FE-I4B ToT resolution is four bits, hence the ToT value can range from 0 to 15. However, the ToT field in a hit word is eight bits, which is due to a feature called *dynamic phi pairing*: If two neighbouring pixels are above threshold, located in the same column but adjacent row, the ToT value of the upper-row hit can be written into the same hit word as the lower-row hit. This is also a bandwidth-saving feature, which in combination with the condensed mode can allow for up to ten hits to be written in only four 32-bit words. The four most significant bits in the ToT field corresponds to the pixel indicated by the row and column numbers, while the four least significant bits correspond to the neighbouring pixel. In case of no hit in this pixel, the ToT is zero.

The FE-I4B has two hit discriminators, one analogue and one digital. The latter is adjustable to three different levels, and gives the threshold for which the ToT value is measured. If the analogue threshold is passed but the digital is not, the hit is assigned status as a ‘small’ hit, and is only kept if adjacent to a ‘big’ hit, i.e. a hit passing the digital threshold. Due to the rise time of the pulse, a small hit is likely to be assigned to the wrong bunch crossing, therefore the association with a big hit

is allowed to stretch one bunch crossing backwards in time [32, 33]. The ToT output from the sensor is encoded using the digital discriminator setting, `HitDiscCnfg`, and is converted back to the true ToT value by the ROD. The relationship between the ToT code and the true ToT value is shown in table 4.2. As can be seen, the value of the `HitDiscCnfg` setting equals the offset from ToT = 1. The `HitDiscCnfg` setting is reflected in the bytestream decoder software, in order to correctly identify the overflow value. At `HitDiscCnfg` = 2, the decoder will interpret ToT 0x2 as 0x10, thereby fully utilising the four-bit ToT budget for all `HitDiscCnfg` settings.

Table 4.2: Conversion table from ToT code to true ToT value, for the different possible values of `HitDiscCnfg`. All numbers in hexadecimal.

	HitDiscCnfg													Overflow	Small hit	No hit
ToT code		0	1	2	3	4	5	6	7	8	9	A	B	C	D	E	F
True ToT	0	1	2	3	4	5	6	7	8	9	A	B	C	D	E	0	0
	1	2	3	4	5	6	7	8	9	A	B	C	D	E	F	1	0
	2	3	4	5	6	7	8	9	A	B	C	D	E	F	2 (→10)	1	0

4.1.2 `PixelRawDataByteStreamCnv`

The descriptively named `PixelRawDataByteStreamCnv` package constitutes the core of pixel bytestream decoding. It receives the module data in sequential order, from all pixel, IBL and DBM RODs, and converts hits into an inner-detector general format called Raw Data Object (RDO) [34]. The RDO data object has specific classes depending on the subdetector; for pixels it represents a single pixel, for SCT it represent a strip, and for TRT a single straw. The common part of the RDO object is the offline identifier, a 64-bit unique number identifying the position of the measurement within the ATLAS coordinate system. Specific to the pixel RDO is the ToT value of the hit, as well as the Level 1 and bunch crossing identifiers.

In addition to converting the hit data into the generalised format, required for the clusterisation and tracking algorithms, the bytestream decoder also propagates the front-end errors to the pixel monitoring software. This is done through an interface to the `PixelByteStreamErrorsSvc` service, which keeps track of the per-event count of all front-end errors, including errors occurring in the fragment decoding. Such decoding errors are

- missing header before a hit word or a trailer; in case of the former, the hit data is ignored,
- missing trailer before a new header is encountered,
- the link number reported by the module is not known to the cabling map (see next section),
- a stream of four condensed hit words is interrupted; in this case all hits in the stream are ignored, or

- the data word was not recognised as any known type.

These errors typically indicate data corruption, except for the unknown link number, which can also be a configuration issue. Errors related to unexpected hit position or ToT values are categorised as 'invalid identifier' errors.

4.1.3 `PixelCabling`

The purpose of the pixel cabling service, located in the `PixelCabling` package, is to provide the translation from the online identity of a given pixel in bytestream data, to its physical position in ATLAS-wide coordinates, represented in the form of an RDO object. To be able to encode simulated events, the reverse operation also has to be supported. The translation can be separated into two stages, the first being to associate a module to its position in η-ϕ-layer space, while the second is to convert row and column number within the module to the η-ϕ position of the pixel. To set the terminology for the translation, the *online* position is the location described by the ROD output, i.e. the ROD/ROB number, the module link number, and the row and column on the module. The *offline* position, on the other hand, is given in eta and phi indices[1] and is part of the RDO.

The cabling map

Identification of a module based on the ROD and link numbers is done using a look-up table constructed upon initialisation of `PixelCablingSvc`. The structure of the table, referred to as the cabling map, is shown in table 4.3. The first four columns are the offline positional parameters, while the others are related to the online identity. The meanings of each of these are:

Barrel/EC Indicating whether the module is located in the barrel region (0), the endcap (+2 for A side (high-η side), -2 for C side) or is part of the DBM (+4 for A side, -4 for C side).

Layer/Disk Layer or disk number. 0 = IBL, 1 = *b*-layer, 2 = layer 1, 3 = layer 2. For DBM, it corresponds to the sensor number in a telescope, ranging from 0 to 2 with increasing $|\eta|$.

Phi and eta module Module index in phi and eta directions.

ROB and ROD ID ROB and ROD identifier numbers. Note that for the pixel layers, one ROD corresponds uniquely to one ROB, and follow the numbering pattern ROD = ROB = `0xDDRRRR`, where `DD` is the subdetector ID, and the `R`'s give the module number. For the IBL, on the other hand, four ROBs are connected to one ROD, and follow a slightly different numbering; ROD = `0xDDRRRL` and ROB = `0xDDRRR0`, where `L` is the Slink number within a stave.

[1] Since the position of a pixel on the module is discrete in η and ϕ, is it given in indices. These indices are internal to the ATLAS software, and are not to be confused with η and ϕ coordinates. To make the distinction more clear, eta and phi are spelled out when referring to the pixel indices.

Table 4.3: Excerpt of the cabling map used for 2017 datataking, showing the entries for half of IBL stave number 2. See the text for explanation of each column.

Barrel/EC	Layer/Disk	Phi module	Eta module	ROBID	RODID	40FMT	40Link	80FMT	80Link	Geo. ID
0	0	1	9	140071	140070	0	7	0	F	LI_S02_A_M4_A8_2
0	0	1	8	140071	140070	0	6	0	F	LI_S02_A_M4_A8_1
0	0	1	7	140071	140070	0	5	0	F	LI_S02_A_M4_A7_2
0	0	1	6	140071	140070	0	4	0	F	LI_S02_A_M4_A7_1
0	0	1	5	140071	140070	0	2	0	3	LI_S02_A_M3_A6
0	0	1	4	140071	140070	0	0	0	1	LI_S02_A_M3_A5
0	0	1	3	140070	140070	0	6	0	7	LI_S02_A_M2_A4
0	0	1	2	140070	140070	0	4	0	5	LI_S02_A_M2_A3
0	0	1	1	140070	140070	0	2	0	3	LI_S02_A_M1_A2
0	0	1	0	140070	140070	0	0	0	1	LI_S02_A_M1_A1

Link and formatter (FMT) numbers The readout bandwidth for the pixel layers can be either 40 Mb/s, in which case the 40FMT/40Link columns are used, or 80 Mb/s (the *b*-layer supports also 160 Mb/s), in which case the 80FMT/80Link columns are used. The link number reported by a pixel module header is an eight-bit aggregation of the two, defined as `(FMT << 4 | Link)`. The IBL modules all operate at 160 Mb/s, hence the meaning of these columns is different. To incorporate the IBL module layout, the 40Link and 80Link columns are repurposed to allow for unique identification of the front-end on a given module. Recall that unlike the pixel modules, where the MCC transmits data for the entire module, the IBL front-ends transmit data separately, so the module identity is insufficient to locate a hit. The value in the 40Link column indicate the lowest-eta front-end on a planar sensor, while the 80Link column indicate the higher-eta one. The numbering of the front-ends decreases with η and is shown in fig. 4.2. For 3D sensors with only a single front-end per module, the 40Link column contains the only relevant values, and the 80Link values are simply set to 0xF. Comparing to the `nnnnn` bits of the fragment header, described in section 4.1, the numbers of the 40/80Link columns correspond to the two least significant bits.

Geographical ID The module name given by DCS. Not of relevance to the software.

To correctly set the pixel link numbers, which depend on the readout speed, the cabling service downloads a list of readout speed settings for all RODs prior to creating the cabling map. This information is stored in the ATLAS COOL conditions database [35]. The values of the cabling map itself was during Run-1 and the beginning of Run-2 read from locally stored text files, but has been updated to be read from the COOL database. This significantly eases the process of updating link numbers in case of hardware upgrades or other changes to the cabling. Reading the values from local files is still supported, and is used for simulation. In particular, a set of mapping files corresponding to potential layouts of the future ITk [36] upgrade have been

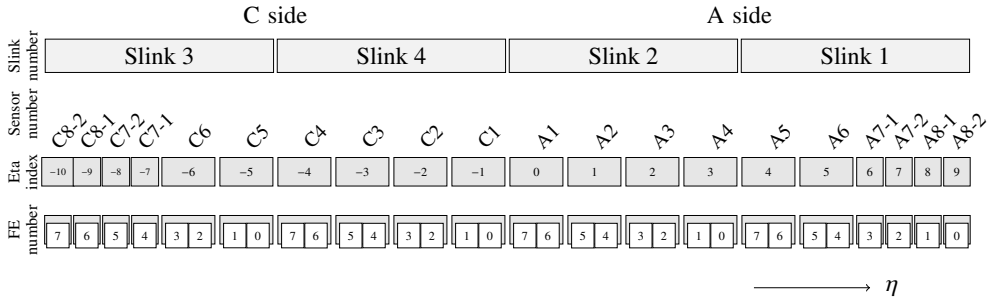

Figure 4.2: IBL sensor numbering.

provided for use in scoping studies. The FE-I4B `HitDiscCnfg` setting is also added in the database, for all individual front-ends. Most front-ends will have the same setting, so in order to save storage space, the database entry contains a single most-common value for the planar sensors, an optional single most-common value for the 3D sensors, and finally an exception list, containing the settings and link numbers of all front-ends which do not adhere to the common value. All database entries are associated with an Interval Of Validity (IOV), a timestamp indicating the start time of a conditions setting. Upon entering a new IOV, the three database entries are downloaded anew, and if a change is detected, all information stored in `PixelCablingSvc` is reloaded. Since the entries are partly interconnected — a change in the readout speed must be reflected by the link numbers of the cabling map — a change in any of the three triggers an update of the two others as well. The software updates have full backwards compatibility, to ensure Run-1 data can be processed even though the newly added database folders are nonexistent in the Run-1 database instance.

Online Identifier

For an efficient mapping between the offline ID of a module, given by the four first columns in the cabling map and encoded in RDO objects, and the module position in terms of online parameters (columns 5 and onwards), a 64-bit online identity token is constructed, defined as

- Pixels: Online ID = `0x00FLDDMMMM`, where `F` = FMT, `L` = link, and `DDMMMM` is the ROB number. The FMT and link values depend on module readout speed, as explained in section 4.1.3.
- IBL: Online ID = `0xEFGHDDMMML`, where `E` = 80FMT, `F` = 80Link, `G` = 40FMT, `H` = 40Link. This definition allows to associate both front-ends on a planar module to the correct module position.

The online ID is purely internal to the pixel bytestream converter code, to facilitate the look-up of modules in the cabling map. With the offline and online module identities being unambiguously determined by the two tokens, the implementation of the module mapping consists of two main dictionaries providing the translation from online ID to offline ID and back; two dictionaries for the ROB to ROD relationship, and one additional dictionary for the `HitDiscCnfg` settings.

On-module pixel identity

The offline module identity is resolved when receiving a module fragment header, while for each following hit, the pixel row and column numbers within the module must be converted to eta and phi indices. This naturally depends on the arrangement of the module, and on the sensor technology. The phi index always increases with increasing ϕ coordinate, while the definition of the eta index differs between the barrel and endcap region: In the barrel, it increases along the positive z direction, and in the endcaps, it increases along the R direction, i.e. it increases for decreasing $|\eta|$. The conversion is done separately for pixels, IBL and the DBM:

Pixels (barrel): The FE-I3 front-ends are arranged in a 8×2 grid on a module, facing each other so that the row number increases towards the centre of the module (see fig. A.2). Hence the phi index is equal to the row number for front-ends 8 to 16, while it decreases with increasing row for front-ends 0 to 7. The same goes for the eta index. Since row and column numbers are given with respect to the front-end, and not the entire module, the indices has to be corrected for the front-end position on the module.

Pixels (disks): Disk modules with odd-numbered phi value (column 3 in table 4.3) follow the same structure as for barrel modules, while even-numbered modules are mirrored, so that the phi index goes in the opposite direction. The logic for the eta index is unchanged.

IBL: All modules on the IBL staves are mounted in the same direction, with phi index increasing along decreasing row number, and eta index increasing with increasing column number. Recall that the numbering in the FE-I4B starts at (row, column) = $(1, 1)$, in contrast to the phi and eta index convention, which like for the FE-I3 which starts at $(0, 0)$. This is taken into account. Further, the eta index must be corrected for the different number of front-ends between planar and 3D modules.

DBM: The DBM sensors are rotated by 90° with respect to the usual phi and eta index directions, so that the eta index increases with decreasing row. The phi index increases with column on the A side of the detector, and decreases with column on the C side.

The software is written to be flexible in terms of the detector layout it can accommodate, which was important during the study of alternative IBL designs, before the hybrid design of planar plus 3D sensors was chosen. To select the correct detector layout for a given geometry description, the `PixelCablingSvc` code is interfaced with the `IBLParameterSvc` package, which provides information about the number of IBL modules, the number of front-ends per module, and the number of columns and rows per front-end. The chain of information in the pixel bytestream conversion code is illustrated as a flowchart in fig. 4.3. Two event displays, showing early 2015 cosmic and collision events, can be seen in fig. 4.4. They illustrate that both the decoding of data and the module position assignments of the `PixelCablingSvc` works correctly.

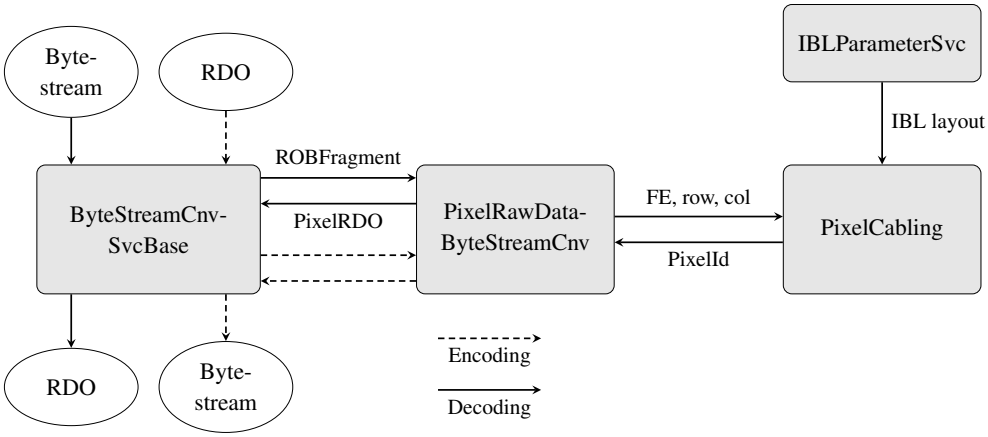

Figure 4.3: The information flow in the pixel bytestream converter software. Solid arrows indicate bytestream decoding, i.e. reading out real data from the detector. The higher-level parts of code (`ByteStreamCnvSvcBase`) selects out `ROBFragments` from the pixel, IBL and DBM subdetectors, and provides them to `PixelRawDataByteStreamCnv` for conversion. The row, column, front-end and module numbers of each hit are converted into a `PixelID` object by the `PixelCabling` code, which requires input on the detector geometry from `IBLParameterSvc`. Dashed arrows indicate bytestream encoding, which is the reverse process, used for processing simulated events. Not shown is the propagation of front-end errors, which are decoded and passed on to the pixel monitoring software.

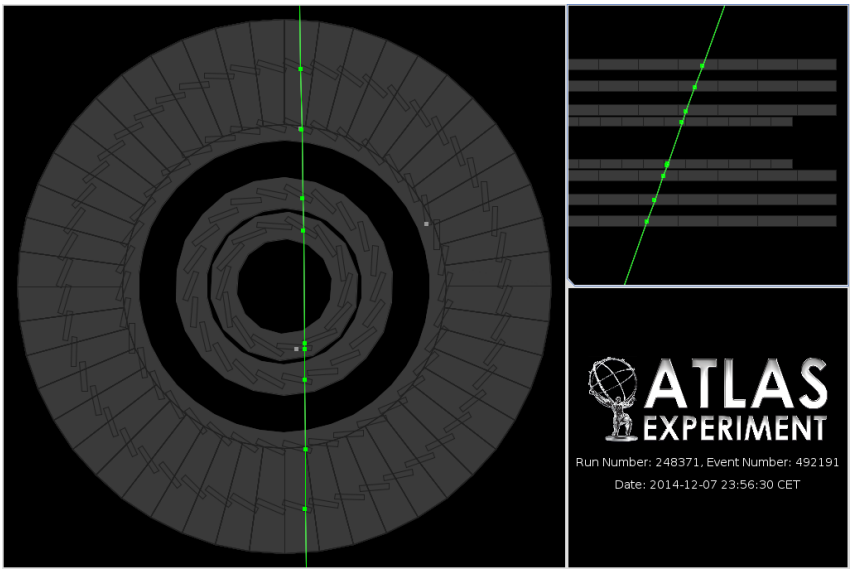

(a) An event display from Milestone Week 7 in December 2014, during a commissioning run to prepare ATLAS for Run 2 datataking. This particular run recorded cosmic radiation, and the green curve shows a cosmic muon passing through the entire detector from above. As one can see there are hits in all layers, including the newly inserted IBL, which is not only operating successfully, but its recorded data is also being properly read out.

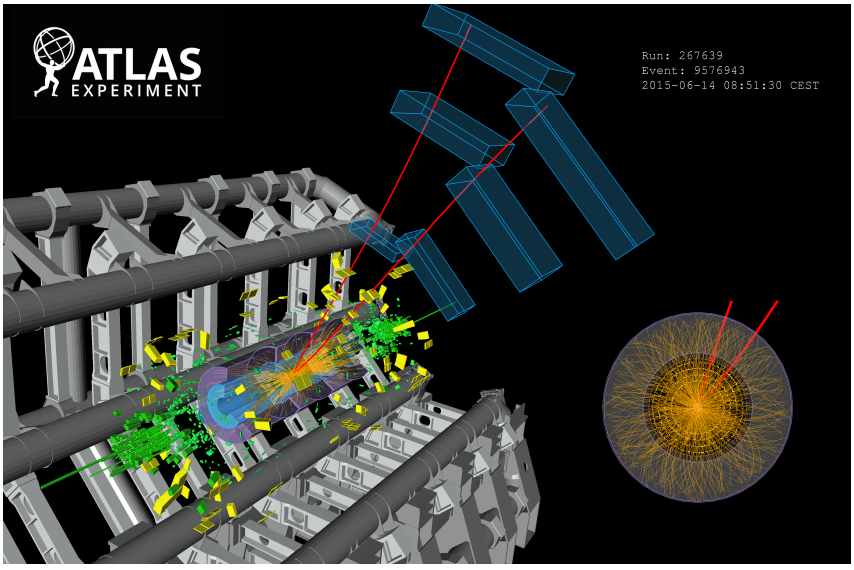

(b) An event display from early collision data in June 2015. The red lines show the tracks of two muons from a J/ψ candidate, extrapolated back from the muon spectrometer to match with tracks in the inner detector.

Figure 4.4: Event displays from early 2015 datataking.

Chapter 5

Depletion voltage measurement

Monitoring the radiation damage to the pixel sensors is vital to the operation of the detector. Given the proximity to the interaction point, the physical properties of the sensors are expected to change noticeably over time, and the design of the sensors reflect this. For optimal performance, the sensors should operate fully depleted, meaning the electrically charged region of the p-n-junction extends over the entire sensor volume. The bias voltage required to maintain full depletion, called the *depletion voltage*, depends on several factors, the main one being the fluence the sensor has been exposed to. The bias voltage of the pixel sensors is continually adjusted and is foreseen to reach 600 V at the end of the sensor lifetime. The depletion voltage has been measured in voltage scans in 2016 and 2017 data.

5.1 Radiation damage in silicon sensors

Radiation-induced effects in semiconductors are typically divided into surface and bulk effects. Surface damage encompasses all effects related to the silicon oxide layer, the passivation layer, and the interface between the two. Ionisation of the oxide is not a fully reversible process, and leads for instance to build-up of positive charge, which increases noise. The following study will however concentrate on damage caused to the sensor bulk, meaning defects created in the silicon lattice. Such defects manifest observable changes like increased leakage current, charge trapping, and most relevant for this study, an increase in the depletion voltage.

On a microscopic level, defects are created by interactions between atoms in the lattice, and impinging particles. The structure of the defect can be a single displaced atom (an interstitial) and a vacancy, known as a Frenkel pair, or in case the impacting particle or recoiling atom has enough energy to displace additional atoms, a defect cluster. The minimum energy required to displace a silicon lattice atom is about 25 eV, while about 5 keV is required to create a defect cluster [37]. Interactions via the Coulomb force tend to favour small energy transfers, so electrons will typically produce point defects, while neutrons, interacting via the strong force, produce mainly clusters. Secondary interactions from knocked-loose atoms evens out the picture, but the amount of radiation damage is still strongly dependent on the type of incoming particle, and its energy. To compare the damage from different types of particles at different energies, one can compute a scaling factor which (to first order) accounts for all energy not causing ionisation, but deposited into the lattice. The

Non-Ionising Energy Loss (NIEL) hypothesis [38] assumes that this scaling factor is proportional to the resulting damage. As a standard for comparison, 1 MeV neutrons are typically used. For a given fluence Φ of a certain particle, the corresponding 1 MeV neutron equivalence fluence Φ_{eq} is obtained by multiplying by the particle's *hardness factor*.

In addition to Frenkel pairs, more complex lattice deformations can occur. These may be neighbouring vacancies or di-interstitials, or the vacancies and interstitials can combine with impurity atoms. This results in new levels in the forbidden gap between the valence and the conduction band, altering the properties of the sensor material. For instance, additional energy levels in the middle of the band gap increases conductivity and therefore the leakage current, while shallow levels act as *traps*, immobilising electrons or holes for a period of time, reducing the charge collection efficiency. Changes to acceptor- or donor-like levels, in the lower or upper part on the band gap, respectively, change the effective doping of the material. This directly affects the depletion voltage.

5.1.1 Evolution of the depletion voltage during irradiation

Before irradiation, the depletion voltage V_{depl} of a simple diode can be expressed in terms of the sensor thickness d and the donor concentration N_{D} [39],

$$V_{\mathrm{depl}} = \frac{q_e N_{\mathrm{D}} d^2}{2\epsilon_0 \epsilon_{\mathrm{Si}}}, \tag{5.1}$$

where q_e is the elementary charge, and ϵ_0, ϵ_{Si} are the permittivities of vacuum and silicon, respectively. For an actual sensor, the layout of the pixel implants and the thickness of the oxide layer will both give corrections to this equation, but focussing on the sensor bulk, the relation generally holds[1].

The spatial extension of the depleted zone depends on the sensor type. For the ATLAS pixel sensors, an n^+-in-n design is used, where n^+-doped electrodes are implanted on an n-type substrate. On the back side of the sensor, p^+ material is deposited. With this configuration, the depleted region grows from the back side, and only reaches the electrodes when the bias voltage is equal to or higher than the depletion voltage. Figure 5.1a illustrates the extension of the depleted zone. This means that for any lower voltages, the pixels are all connected by the conducting bulk material, rendering the sensor unoperational. At the depletion voltage, the strength of the electric field is lowest closest to the pixel side, so operating at a higher voltage (*overdepletion*) is beneficial for the charge collection.

The advantage of the n^+-in-n design lies in the behaviour after irradiation. The effective doping of the bulk material is altered by the creation of Frenkel pairs, which can migrate through the lattice, and interact with dopant atoms. A vacancy can for instance combine with a phosphorus atom, neutralising its donor property. Another case is di-vacancies combining with oxygen, which adds acceptor-like energy levels in the band gap. The depletion voltage becomes a function of the effective doping

[1] This expression relies on a few assumptions. First, that donor and acceptor atoms are completely ionised, so that the electron/hole concentrations are equal to the concentration of acceptors/donors. Second, that the diode consists of a highly doped p^+ implant in low doped bulk material, and third, that the built-in potential is negligible compared to the bias voltage. For details on the derivation, see [39].

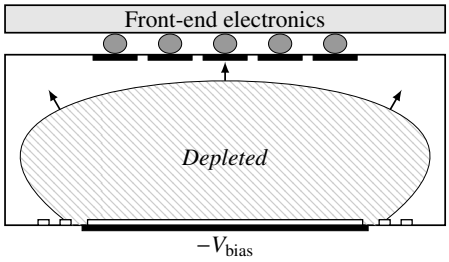

(a) Before type inversion. The sensor bulk is n-type, and the depleted region grows from the p-n-junction located at the back side (bottom) of the sensor.

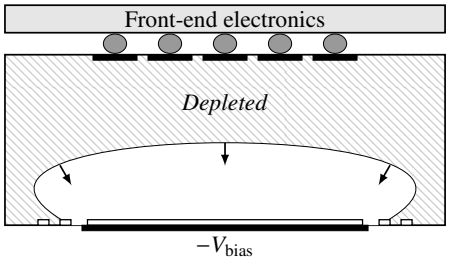

(b) After type inversion. The sensor bulk is now p-type, and the depleted region grows from the read-out side (top).

Figure 5.1: Illustration of the depletion zones in a sensor. The arrows indicate the direction of growth of the depleted region with increasing bias voltage.

$N_{\text{eff}} = N_D - N_A$, which is the difference between donor-like and acceptor-like states, and can be expressed similarly to eq. (5.1):

$$V_{\text{depl}} = \frac{q_e |N_{\text{eff}}| d^2}{2\epsilon_0 \epsilon_{\text{Si}}}. \tag{5.2}$$

As the concentration of acceptor-like states increases, the depletion voltage decreases, until it reaches the point where N_{eff} becomes zero. This is known as the point of type inversion (or space charge inversion). From here on, N_A starts to dominate, and the silicon bulk effectively becomes p-type. The p-n-junction is now shifted to the read-out side, and the depletion region grows in the opposite direction, as illustrated in fig. 5.1b. The depletion voltage, which depends on the absolute value of N_{eff}, rises again, and continues to rise as the fluence increases. The evolution of V_{depl} as function of 1 MeV neutron equivalent fluence is shown in fig. 5.2. At the point where the bias voltage can no longer be increased, the sensor can still be operated partially depleted, since the peak of the electric field is now located by the electrodes. At partial depletion, the charge collection efficiency is expected to be proportional to the depth of the depleted region. This is an approximate statement due to the complexity of the electric field structure, which is described (at least partially) by the double junction model [40], where a structure of the type p^+npn^+ is assumed. Test-beam studies show that there is still some charge collected from the undepleted region, demonstrating that a small electric field is present also here [39].

5.1.2 Evolution of depletion voltage over time, after irradiation

Lattice defects are in general mobile, and diffuse over time. This causes Frenkel pairs to recombine, consolidate into more stable defects, or otherwise rearrange into other configurations. This behaviour is collectively known as *annealing*, and alters the effective doping of the silicon bulk. The time scales for these processes differ, but can be associated to a short- and a long-term component, as described by the

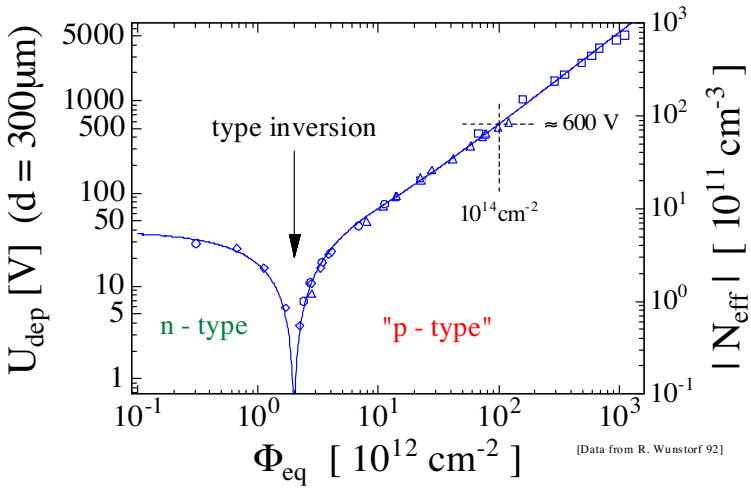

Figure 5.2: Depletion depth as function of fluence, measured immediately after neutron irradiation [37]. The solid curve represents the Hamburg model.

Hamburg model [41]:

$$\begin{aligned}\Delta N_{\text{eff}}(\Phi_{\text{eq}}, t, T) &\equiv N_{\text{eff}}(\Phi_{\text{eq}} = 0) - N_{\text{eff}}(\Phi_{\text{eq}}, t, T) \\ &= N_C(\Phi_{\text{eq}}) + N_A(\Phi_{\text{eq}}, t, T) + N_Y(\Phi_{\text{eq}}, t, T).\end{aligned} \tag{5.3}$$

The first component, N_C, depends only on the fluence and accounts for the rates of donor removal, and acceptor creation. The second component, N_A, depending on time t and temperature T, represents short-term, *beneficial* annealing. This relates to decay of the radiation-induced acceptor-like states, and decreases exponentially with a time constant of around 20 minutes at a temperature of 60°C [42]. The last component N_Y is a long-term effect, with a time constant of 21 hours at 60°C, but increases rather than decreases N_{eff} over time. This effect is referred to as reverse annealing. It should be noted, however, that the time constants are strongly dependent on temperature: For comparison, at 0°C, the beneficial annealing time constant is around 53 days, while the time constant for the reverse annealing is 61 years. This means that in the temperature controlled environment in the inner detector, reverse annealing can in practice be avoided, while raising the temperature during technical stops allows to take advantage of the beneficial annealing process. Parameterisations of the terms in eq. (5.3) can be found in [42].

Evolution of charge collection efficiency

The charge trapping rate is proportional to the concentration of trapping centres, which is, to first order, proportional to the fluence. Trapping becomes a problem when charges are trapped for longer than the charge collection time. For the ATLAS sensors, the charge collection efficiency after 1×10^{15} $n_{eq}cm^{-2}$ irradiation followed by beneficial annealing is $(72 \pm 14\,\%)$ [43]. This does not affect the depletion voltage, but is mentioned here as it makes an impact on the measurement technique described in the next section.

5.2 Depletion voltage scans

Several methods exist to measure the depletion voltage of a sensor. This section gives a short review on the main advantages and drawbacks of some of them.

IV measurements Thermal excitations occurring in the depleted region of the sensor will cause a current to flow. Being proportional to the size of the depleted volume, this current will increase with voltage until full depletion is reached, and then remain constant. Plotting the current as function of bias voltage can therefore be used to extract V_{depl}, which is convenient, since one would typically do this measurement anyway, when testing the breakdown voltage of a sensor. The method is somewhat impractical, however, since the transition between the rise (which goes with the square root of the voltage) and the plateau is not exact. The total leakage current is also dependent on charge diffusion and other factors. Because it increases proportionally with fluence, the leakage current is a good measure of the accumulated radiation dose.

CV measurements A similar but more precise method is to plot inverse square of the capacitance as function of voltage. Viewing the sensor as two conductive plates separated by the depletion depth, the capacitance decreases with increasing bias voltage and becomes constant at full depletion. Once a readout circuit is attached to the sensor, the method is not applicable anymore, since this disrupts the capacitance measurement.

Inter-pixel crosstalk Since the undepleted region of the silicon bulk is conductive, the depletion voltage of the sensor *before* type inversion can be measured by looking at the charge collection in a single pixel, while injecting charge into the neighbouring ones. At the point of full depletion, the pixels become isolated and will not experience cross-talk. After type inversion, the method cannot be used anymore, since the depleted region grows from the readout side of the sensor. This rules out the method for this study, as the *b*-layer type-inverted in 2012 after approximately 5 to 10 fb^{-1}, while the IBL underwent inversion in 2015 after about 3 fb^{-1} of integrated luminosity [44].

Grazing angle A way to study the depth of the depleted region for a given bias voltage, is to place the sensor in a testbeam under a shallow incidence angle, and look at the distribution of pixel hits along the trajectory of the beam. If a track traverses the undepleted region of a pixel, the collected charge will be significantly smaller (although non-zero) than in the depleted region. Using the incidence angle and the point of impact, one can compute the depletion depth to a precision of the order of microns. This technique was used to test the ATLAS pixel sensors [45, 46]. The method necessarily needs a testbeam setup, and cannot be used to evaluate sensors after they have been installed in the detector.

Once sensors are installed in the detector, the choice of methods is rather limited, especially when considering that it must also work after type inversion. The method

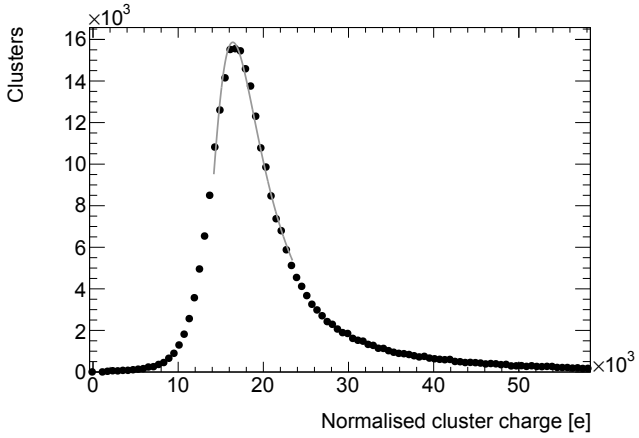

Figure 5.3: Example of a fit to cluster charge, for Layer 2 in run 324320, operated at 120 V. The grey curve shows the fit function, which is a convolution of a Landau and a Gaussian distribution.

chosen for this analysis, is to monitor the charge collection during collision data taking, while increasing the bias voltage in steps. The collected charge is to first order proportional to the bias voltage when $V_{\text{bias}} < V_{\text{depl}}$, while constant after V_{depl} is reached. Results are provided in unit of ToT, which is independent of the per-module ToT to charge calibration.

For this study, only pixel clusters associated to an inner detector track are selected. The tracks are required to pass the *loose-primary* selection of the `InDetTrackSelectionTool`, provided by the tracking group. The full description of the individual selections comprising this working point is documented in [47]. In addition, tracks are required to have transverse momentum larger than 500 GeV, and have hits in all pixel layers. The track-hit residuals must be less than 1.0 mm in both the local x and y directions. Clusters are excluded from the analysis if they contain long or ganged pixels, and the distance to the closest neighbouring cluster centre is required to be more than 2.0 mm, to avoid overlap or charge sharing.

For each cluster, the charge is normalised to correspond to normal track incidence angle, by dividing by the track length. The length l is computed from the incidence angles in the local x direction (ϕ) and in y direction (θ), yielding

$$l = \sqrt{(\tan\theta)^2 + 1/(\cos\phi)^2}. \tag{5.4}$$

For each scan point, i.e. each examined bias voltage, the distribution of normalised cluster ToT is fitted to obtain the most probable value. Generally, the average energy loss through ionisation follows a Landau distribution, but is here convoluted with a Gaussian to account for resolution effects. An example of such a fitted distribution is shown in fig. 5.3.

To estimate the depletion voltage, a two-phased piecewise linear function is fitted to the values of the most probable cluster ToT. The intersection point of the two linear parts gives the estimate of the voltage at full depletion, $\hat{V}_{\text{depl}}$. The transition is

smoothed by a quadratic term with smoothing factor e, resulting in the following fit function:

$$f(V) = a + b(V - \hat{V}_{\text{depl}}) - (b + c)\sqrt{(V - \hat{V}_{\text{depl}})^2 + e}. \tag{5.5}$$

Here, a is the constant offset, while b and c are the slopes of the two linear parts. No initial restrictions are imposed on any of the fit parameters, and the fit function in not required to pass through the origin, as the assumption of linear relationship between ToT and bias voltage is not expected to hold for low voltages in irradiated sensors. Exceptionally, if the fit fails to converge, the slope of the second linear segment is fixed to zero, i.e. the plateau is force to be flat, before the fit is performed anew.

5.2.1 Data samples

Voltage scans were performed at five different occasions in 2016 and 2017. The first was done in April 2016, during the first runs with stable beams, after the winter shutdown. The IBL had at this point been exposed to $3.2\,\text{fb}^{-1}$ of integrated luminosity, while the pixel layers had seen an additional $28.9\,\text{fb}^{-1}$ of Run 1 luminosity. The scan was split over two consecutive LHC fills, corresponding to run numbers 296939 and 296942, and consisted of six scan points for IBL and disks (including the nominal voltage), eleven for the *b*-layer, and five for layers 1 and 2.

The second scan was performed on October 6, 2016, in run 310015, during a week of machine development. $29.2\,\text{fb}^{-1}$ had been delivered since the previous scan. Unfortunately only four scan points of IBL modules were completed before the beam was dumped, and stable beams were not declared again until after the machine development period was over. A new scan was done two weeks later, in run 310969, taking six points for the IBL and for the *b*-layer. Over these two weeks, approximately $3.8\,\text{fb}^{-1}$ of collisions were delivered. An additional $2.8\,\text{fb}^{-1}$ was collected before the 2016 datataking was closed.

The first of the 2017 scans were performed in May, in run 324320 and 324340, during the first stable beams at the end of the recommissioning period. Nine scan points were taken for the *b*-layer, layer 1, and planar IBL modules, eight for layer 2 and disks, and seven for the 3D IBL modules. The last of the scans were taken in end of November 2017, after a strong period of LHC operation, doubling the Run 2 luminosity. All detector layers were scanned during this run.

For all scans, each scan point had a duration of five lumiblocks. However, the first and last lumiblock is rejected to ensure all module voltages are stable. The exception is run 339957, where the duration was three lumiblocks per scan point. A list of the dates and run numbers are given in table 5.1.

5.2.2 Results

Depletion voltages for each layer are extracted for all runs, excluding the cases where the scanned voltage range did not cover both the rising part (required to fit the slope b in eq. (5.5)) and the plateau (required to fit c) of the cluster ToT curve. The results are averaged over all modules in the layer. The following systematic uncertainties are considered:

Table 5.1: Numbers and dates of runs used for voltage scans. The luminosity column gives the integrated delivered luminosity between the start of Run 2 and the date of the respective run.

Run number	Date	Components	Approx. accumulated Run 2 luminosity [fb^{-1}]
296939	Apr 22, 2016	IBL	3.39
296942	Apr 23, 2016	BL, L1, L2, disks	3.39
310015	Oct 6, 2016	IBL	32.6
310969	Oct 19, 2016	IBL, BL	36.3
324320	May 23, 2017	BL, L1, L2	39.2
324340	May 23, 2017	IBL	39.2
339957	Nov 23, 2017	IBL, BL, L1, L2, disks	82.4

Sensor thickness For pixels, the uncertainty in wafer thickness is 6 µm [43]. The uncertainty on the IBL thickness is not given, so the same value as for pixels is assumed. This yields a 2.4% uncertainty on the track length correction for pixels, 2.6% 3D IBL sensors, and 3% for IBL planar sensors.

Alignment A misalignment of the rotational degrees of freedom for the individual modules would affect the track length correction. During the first alignment of the IBL, a temperature-dependent distortion of the staves was observed [48], which affected both the position and rotation of the modules. This effect is however well studied and corrected for with high precision in the updated alignment [49]. The position of the pixel modules have since Run 1 been aligned to within 1 µm [50]. A 1° variation in both η and ϕ would impact the track length correction by only 0.1%, therefore this uncertainty is neglected.

ToT calibration The modules are regularly calibrated so that a given charge always yields the same ToT. For the IBL, 16×10^3 electrons should produce a ToT of 8; for pixels, the tuning is ToT of 18. The ToT is observed to drift over time [44], resulting in a difference between calibration scans which is typically below 5%. This effect shifts the offset value a in eq. (5.5), but has limited effect on $\hat{V}_{\text{depl}}$. In any case, to account for the fact that the ToT calibration is done individually per module and may affect the layer-averaged measurement differently after each new calibration, the 5% uncertainty is retained.

Fit The systematic uncertainty arising from the choice of fit model (eq. (5.5)) is evaluated by repeating the fit without the quadratic smoothing term, i.e. fixing $e = 0$. Half of the difference with respect to the nominal result is taken as the uncertainty. If the fit was constrained by requiring the plateau of the curve to be flat, an additional 10% uncertainty on the measured value is added.

The results are shown in figs. 5.4 to 5.8, and the fit values for the depletion voltage are listed in table 5.2.

For the IBL planar sensors, shown in fig. 5.4, the depletion voltage is very low for the first of the 2016 runs, as is expected, since the sensors had type-inverted

Table 5.2: Results for the depletion voltage measurements. For each layer, all modules are averaged over, before a fit to the normalised cluster ToT is performed. The first uncertainty is statistical, while the second is systematic. The main contribution to the systematic uncertainty comes from the fit. All values are given in volts.

Layer	Run number			
	296939/ 296942	310969	324320/ 324340	339957
IBL planar	$13.31 \pm 0.06 \pm 1.88$	$100.6 \pm 0.1 \pm 16.7$	$90.0 \pm 0.3 \pm 22.9$	$211.9 \pm 0.3 \pm 24.6$
IBL 3D	–	–	–	$19.6^{+1.4}_{-0.6} \pm 2.2$
b-layer	–	$143.1 \pm 0.4 \pm 21.4$	$111.4^{+3.3}_{-3.5} \pm 20.6$	$228.0 \pm 0.6 \pm 27.8$
Layer 1	$21.6 \pm 0.3 \pm 6.9$	–	$55.3^{+2.7}_{-3.6} \pm 3.3$	$120.9 \pm 0.6 \pm 14.6$
Layer 2	$32.5^{+0.3}_{-0.4} \pm 2.6$	–	$28.1^{+3.2}_{-4.1} \pm 7.87$	$87.4 \pm 0.6 \pm 5.3$

the year before. The scan in run 310015 was aborted before reaching the charge-collection plateau, but one can see that the two weeks of irradiation before the next scan (run 310969) was started, had already increased the depletion voltage significantly. From the following run in early 2017 (run 324320), the effect of beneficial annealing over the winter shutdown is apparent. The nominal operating voltage for the planar sensors was 150 V in 2016, increased to 350 V in 2017. These values ensured the sensors were operated at the plateau at all times during datataking, although the margin in 2016 turned out to be somewhat small. For the IBL 3D sensors, shown in fig. 5.5, the last of the 2017 scan was the first run one could really identify the point of underdepletion.

The first 2016 scan of the *b*-layer was started at too high voltages, and could not be used to fit the depletion voltage. It did, however, provide an estimate of the range to be covered in the following scan, which was successful. The large difference in the plateau value of the charge and ToT is believed to be caused mainly by a change in the ToT calibration, which was incorrect for all runs up until run number 298862. As seen in the IBL curves, the annealing effect during the winter shutdown reduces the depletion voltage also in the *b*-layer, here by approximately 30 V. The irradiation during the entire 2017 run period increased V_{depl} up to nearly 230 V, which is still well below the nominal operating voltage of 350 V. It should be noted that the uncertainty from the fit is rather large in several of the measurements.

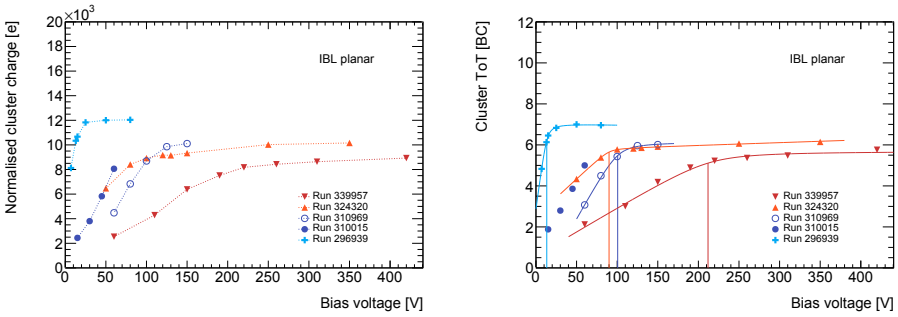

(a) Cluster charge (b) Cluster ToT

Figure 5.4: IBL, planar sensors

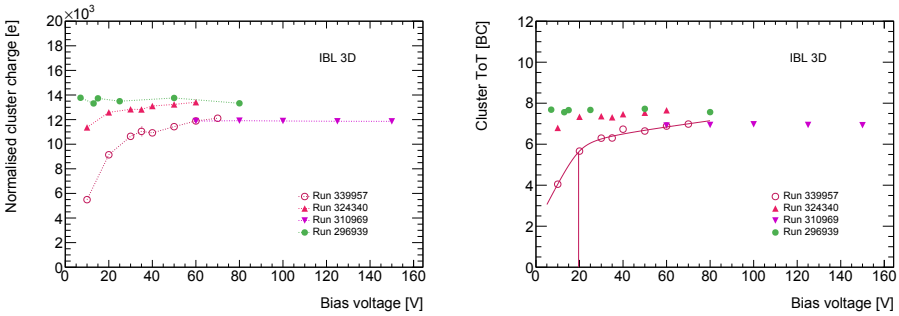

(a) Cluster charge (b) Cluster ToT

Figure 5.5: IBL, 3D sensors

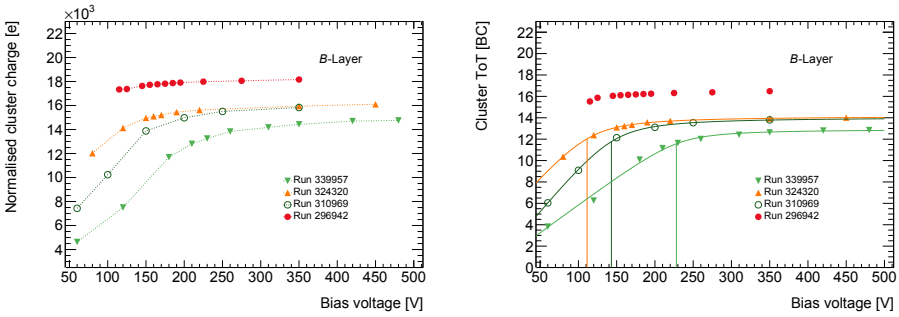

(a) Cluster charge (b) Cluster ToT

Figure 5.6: *b*-layer

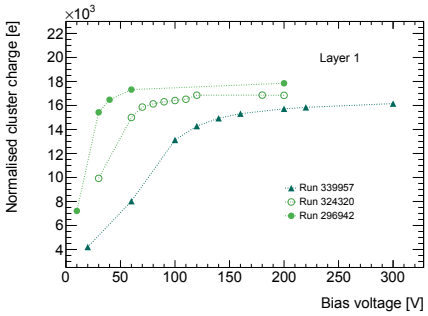

(a) Cluster charge

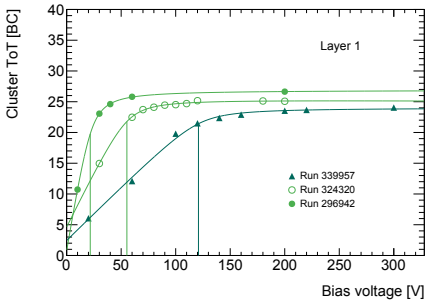

(b) Cluster ToT

Figure 5.7: Layer 1

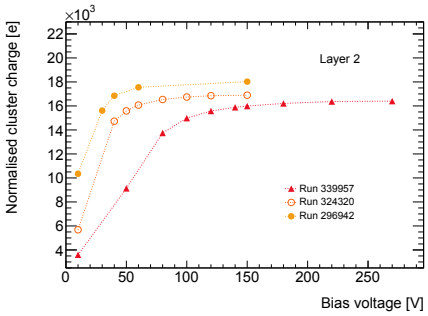

(a) Cluster charge

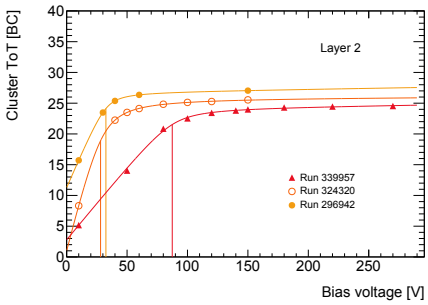

(b) Cluster ToT

Figure 5.8: Layer 2

Part III

Higgs decays to τ pairs

Chapter 6

Analysis introduction

This chapter discusses the theoretical motivation behind the analysis, the observables used, and signal modelling in simulation. The technical implementation of the analysis is described in the next chapter.

6.1 Theoretical motivation

In presence of *CP*-violating effects, a model-independent effective Lagrangian for the Yukawa interaction between the Higgs H and taus can be parametrised using a mixing parameter ϕ_τ,

$$\mathscr{L}_{H\tau\tau} = -\frac{m_\tau}{v}\kappa_\tau(\cos\phi_\tau\bar{\tau}\tau + \sin\phi_\tau\bar{\tau}i\gamma_5\tau)H\,, \tag{6.1}$$

where $v = 246\,\text{GeV}$ is the vacuum expectation value of the Higgs field, and $\kappa_\tau > 0$ is the reduced Yukawa coupling strength. A mixing parameter value of $\phi_\tau = 0$ corresponds to a *CP*-even coupling, which is the Standard Model hypothesis. For $\phi_\tau = \pi/2$, only the $\bar{\tau}i\gamma_5\tau$ term is nonzero, corresponding to a pure *CP*-odd coupling. Any other value indicates that the coupling violates *CP*. The mixing parameter is not a physical observable by itself, but is accessible through studying the correlation between the transverse spin components of the taus. In the tau rest frame, the spin vector can be decomposed into parts longitudinal (s_z) and transverse ($\boldsymbol{s}_\perp$) to the normalised tau direction, $\hat{\boldsymbol{k}}$, where $\hat{\boldsymbol{k}}$ is evaluated in the rest frame of the Higgs. From the differential decay width [51]

$$d\Gamma_{h\tau\tau} \propto 1 - s_z^- s_z^+ + \cos(2\phi_\tau)(\boldsymbol{s}_\perp^- \cdot \boldsymbol{s}_\perp^+) + \sin(2\phi_\tau)[(\boldsymbol{s}_\perp^- \times \boldsymbol{s}_\perp^+) \cdot \hat{\boldsymbol{k}}^-], \tag{6.2}$$

one can explicitly see the relation between ϕ_τ and the transverse spin components of the taus. Because the weak decay of tau violates parity maximally, information about the spin direction is passed on to the decay products, encoded in their angular distributions. Accessing the correlation can be done by constructing a plane from the decay products of each tau, and measuring the angle between them, $\varphi^*_{CP} \in [0, 2\pi)$. The decay planes and the φ^*_{CP} angle is shown in fig. 6.1. In a τ^- decay, the neutrino is preferably emitted in the antiparallel direction to the transverse spin vector of the tau, and the visible decay products in the parallel direction. For a τ^+ decay, the directions are reversed. This means that if the taus come from a scalar particle and have their

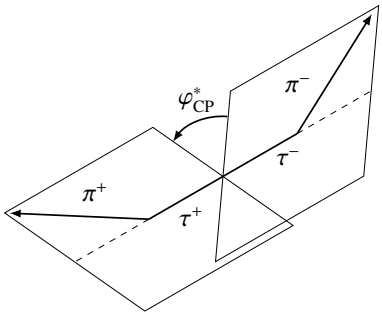

Figure 6.1: Illustration of φ^*_{CP}. The dashed lines indicates the direction of the taus before decaying, in the ditau rest frame.

transverse spin components aligned, the visible decay products preferably go in the opposite directions, and from looking at fig. 6.1 one expects φ^*_{CP} to be peaked around π. Similarly, for taus from the decay of a pseudoscalar, φ^*_{CP} is peaked around 0 and 2π. More accurately, the relation between φ^*_{CP} and the mixing parameter can be shown by reformulating the differential decay width as [52]

$$d\Gamma_{h\tau\tau} \approx 1 - b(E_+)b(E_-)\frac{\pi^2}{16}\cos(\varphi^*_{CP} - 2\phi_\tau)\,. \tag{6.3}$$

This approximation holds at leading order. The functions $b(E_\pm)$ express the spin analysing power of the given decay mode, which for the direct decay $\tau \to \pi\nu$ equal $+1$, but are for other decays in general energy dependent. As can be seen from eq. (6.3), the decay width for a *CP*-even Higgs boson follows a cosine curve, while for a *CP*-odd Higgs it has a phase shift of π. Observing a φ^*_{CP} distribution with a phase of a non-integer multiple of π would indicate *CP* mixing.

A vital feature of the φ^*_{CP} observable is the fact that for background processes, it follows a uniform distribution. Hence the sensitivity to ϕ_τ is a priori not biased by the presence of backgrounds. For combinatorial background where the taus are not correlated, for instance if one or both tau candidates are misreconstructed jets, all angular configurations are of course equally probable; however, it can be shown that the cross section for $Z/\gamma^* \to \tau\tau$ is also independent of φ^*_{CP} for all final states [53].

6.2 Observables

Constructing φ^*_{CP} as shown in fig. 6.1 is a purely academic exercise, since the neutrino momenta cannot be determined. On detector level, two different φ^*_{CP} reconstruction methods can be employed, using the four-momenta of the available decay products to form decay planes. In both cases, the four-momenta are given in the restframe of the visible ditau system, obtained by a rotation-free Lorentz boost along the combined ditau direction.

6.2.1 Impact parameter (IP) method

The Impact Parameter (IP) method [53] requires only a single track to form the decay plane, using its three-dimensional impact parameter vector. It can in principle be used for any tau decay, but naturally excels for one-prong decays with no π^0s, where this is the only choice. The tau decay plane is constructed using the spatial vector $\mathbf{q}_\pm$ and the impact parameter vector $\mathbf{n}_\pm$ of the charged track. The impact parameter vector is defined as the point of closest approach between the track and the primary vertex. A schematic illustration of the vectors and the tau decay plane is shown in fig. 6.2a. The component of the impact parameter vector which is transverse to the track spatial vector, denoted $\mathbf{n}_\perp$, is computed for both the positive and negative track. Using the normalised vectors (unit vectors are in the following always indicated by a circumflex), the angle φ^* between the tau decay planes can be defined by

$$\varphi^* = \arccos(\hat{\mathbf{n}}_\perp^+ \cdot \hat{\mathbf{n}}_\perp^-)\,, \tag{6.4}$$

where $+, -$ indicates the charge of the track. The direction of the negative track can be used to compute a *CP*-odd and *T*-odd triple-product correlation $\mathcal{O}^*_{CP}$,

$$\mathcal{O}^*_{CP} = \hat{\mathbf{q}}_- \cdot (\hat{\mathbf{n}}_\perp^+ \times \hat{\mathbf{n}}_\perp^-)\,. \tag{6.5}$$

The φ^*_{CP} observable, ranging from 0 to 2π, can now be defined by

$$\varphi^*_{CP} = \begin{cases} \varphi^* & \text{if } \mathcal{O}^*_{\mathrm{CP}} \geq 0 \\ 2\pi - \varphi^* & \text{if } \mathcal{O}^*_{\mathrm{CP}} < 0 \end{cases}\,. \tag{6.6}$$

Although the above definition is given for decays with a single track, the method can also be extended to three-prong decays such as $\tau^\pm \to a_1\nu \to \pi^\pm\pi^\mp\pi^\pm\nu$ by using the combined momentum vector of the three tracks, and calculating the closest point of approach between this vector, starting in the tau decay vertex, and the primary vertex.

The distribution of φ^*_{CP} on generator level, for a *CP*-even and *CP*-odd Higgs, along with the main background $Z \to \tau\tau$, is shown in fig. 6.3a.

6.2.2 ρ method

For tau decays involving neutral pions, one can span a plane from the spatial vectors of the charged and the neutral components. This method is usually called the ρ method, since it is suitable for indirect decays via a $\rho(770)$, which in turn decays to $\pi^\pm\pi^0$. The method can also be used for any tau decay mode with more than one π^0, by separately summing charged and neutral decay products, but the sensitivity to the transverse spin direction of the decaying tau deteriorates drastically with increasing multiplicity of the final state. The angle φ^* and the triple correlation $\mathcal{O}^*_{CP}$ are defined using the normalised spatial vectors of the charged and neutral components $\hat{\mathbf{q}}^\pm$ and $\hat{\mathbf{q}}^{\mathbf{0}\pm}$, where the '+' superscript on $\hat{\mathbf{q}}^{\mathbf{0}+}$ indicates that this π^0 is associated with the π^+, and vice versa. Taking the transverse component of $\hat{\mathbf{q}}^{\mathbf{0}\pm}$ relative to $\hat{\mathbf{q}}^\pm$, the definition reads

$$\varphi^* = \arccos(\hat{\mathbf{q}}_\perp^{0+} \cdot \hat{\mathbf{q}}_\perp^{0-}), \qquad \mathcal{O}^*_{\mathrm{CP}} = \hat{\mathbf{q}}^- \cdot (\hat{\mathbf{q}}_\perp^{0+} \times \hat{\mathbf{q}}_\perp^{0-})\,. \tag{6.7}$$

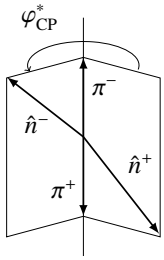

(a) Tau decay planes reconstructed using the IP method.

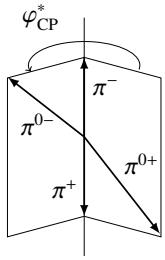

(b) Tau decay planes reconstructed using the ρ method.

Figure 6.2: Illustrations of the tau decay plane reconstruction methods.

An intermediate angle $\varphi^{*\prime}$ is defined by

$$\varphi^{*\prime} = \begin{cases} \varphi^* & \text{if } \mathscr{O}^*_{\mathrm{CP}} \geq 0 \\ 2\pi - \varphi^* & \text{if } \mathscr{O}^*_{\mathrm{CP}} < 0. \end{cases} \tag{6.8}$$

Because the spin sensitivity of each decay plane is dependent on the energy difference between the charged and neutral component, the average distribution of $\varphi^{*\prime}$ is at this point uniform. To obtain a nontrivial shape, events are separated based on the sign of the observables

$$y_- = \frac{E_{\pi^-} - E_{\pi^0}}{E_{\pi^-} + E_{\pi^0}}, \qquad y_+ = \frac{E_{\pi^+} - E_{\pi^0}}{E_{\pi^+} + E_{\pi^0}}, \tag{6.9}$$

where the pion energies are measured in the laboratory frame [51]. The angle φ^*_{CP} can now be defined in a unified way:

$$\varphi^*_{CP} = \begin{cases} \varphi^{*\prime} & \text{if } y_+ y_- \geq 0 \\ 2\pi - \varphi^{*\prime} & \text{if } y_+ y_- < 0\,. \end{cases} \tag{6.10}$$

The distribution of φ^*_{CP} for $\tau \to \rho(\pi^\pm\pi^0)\nu$ is shown in fig. 6.2b.

6.2.3 Combined IP-ρ method

In case of one tau of the ditau pair decaying with a neutral component and the other without, the IP and ρ decay methods can be combined, to create a φ^*_{CP} observable consistent with the definitions in the two previous sections. Considering a case where the τ^+ decays to $\rho^+(\pi^+\pi^0)$, the normalised direction $\hat{\mathbf{q}}^{0+}_\perp$ of the π^0 transverse to the π^+ is computed; while if the τ^- decays to $\pi^-\nu$, the decay plane is on this side constructed using the transverse component of the impact parameter vector $\hat{\mathbf{n}}^-_\perp$ and the spatial vector $\hat{\mathbf{q}}^-$ of the π^-, which yields

$$\varphi^* = \arccos(\hat{\mathbf{q}}^{0+}_\perp \cdot \hat{\mathbf{n}}^-_\perp), \qquad \mathscr{O}^*_{\mathrm{CP}} = \mathrm{sgn}(\rho) \cdot \hat{\mathbf{q}}_- \cdot (\hat{\mathbf{q}}^+_\perp \times \hat{\mathbf{n}}^-_\perp)\,. \tag{6.11}$$

These two are combined into the intermediate angle φ^* according to

$$\varphi^{*\prime} = \begin{cases} \varphi^* & \text{if } \mathscr{O}^*_{\mathrm{CP}} \geq 0 \\ 2\pi - \varphi^* & \text{if } \mathscr{O}^*_{\mathrm{CP}} < 0 \end{cases}. \tag{6.12}$$

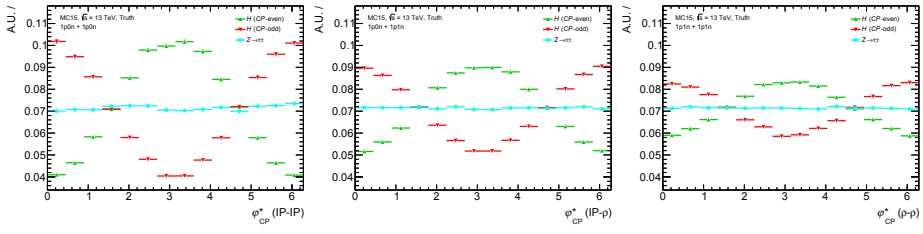

(a) IP method, applied to $\tau^+\tau^- \to \pi^+\pi^-$ decays.

(b) IP-ρ method, applied to $\tau^\pm\tau^\mp \to \rho^\pm(\pi^\pm\pi^0)\pi^\mp$ decays.

(c) ρ-ρ method, applied to $\tau^+\tau^- \to \rho^+\rho^-$ decays.

Figure 6.3: Distributions of φ^*_{CP} for the three relevant ditau decay modes, at generator level. Green points corresponds to pure scalar Higgs, red points to a pseudoscalar, while blue points show the distribution for $Z \to \tau\tau$ decays.

Using the sign of y_+, defined in eq. (6.9), the definition of φ^*_{CP} becomes

$$\varphi^*_{CP} = \begin{cases} \varphi^{*\prime} & \text{if } y_+ \geq 0 \\ 2\pi - \varphi^{*\prime} & \text{if } y_+ < 0 \end{cases} . \tag{6.13}$$

In case of charge conjugation, the definition of course remains the same, but the sign of the ρ charge must be included in the triple product in eq. (6.11).

6.2.4 Mass reconstruction

The invariant mass of the ditau system is reconstructed using a method called the *Missing Mass Calculator (MMC)* [54], which aims to find the most probable neutrino momenta, given the kinematic constraints of the decay. This is done by scanning over the distance between the visible and invisible decay products, while calculating the likelihood at each scan point. The probability density function for the distributions are constructed using simulated events. The final mass estimate, for a single event, is the mass corresponding to the maximum likelihood. The symbol $m_{\tau\tau}^{\text{MMC}}$ is used to indicate the invariant mass reconstructed using the MMC.

6.3 Modelling Higgs decays to τ pairs

In the simulation of the signal process $pp \to H \to \tau\tau$, the narrow width approximation is assumed, meaning that the production and decay factorises and can be treated separately. This allows for using different Monte Carlo generators for the two steps. Since the analysis requires simulation of several *CP* mixing scenarios, some practical aspects need to be taken into account. Two possible approaches can be taken, the first one being to generate independent samples for each mixing hypothesis under consideration. This necessarily requires an MC generator capable of computing the matrix element of a Lagrangian containing *CP*-violating Yukawa terms. The other option is to generate a single MC sample, and subsequently re-weight events according to the different mixing scenarios, based on a recalculation of the matrix element. In practice, this weighting procedure gives higher importance to simulated decays that

are more likely to originate from a given *CP* state. Although this strategy requires additional post-processing of the sample, the re-use of events for different mixing scenarios greatly increases the sample statistics; further, since the samples for the different scenarios are dependent, there are no inter-sample statistical fluctuations to potentially disrupt the basis for comparison. The following section shows that the two approaches result in identical kinematic distributions. Spin correlations are for the first case computed in the Pythia [55] MC generator, while in the second using TauSpinner [56–58]. Both will be introduced in the following sections.

These studies were performed using generators interfaced through the common ATLAS software Athena, release 19.2.3.6. Since the aim is to check the truth-level kinematics, no detector simulation is performed. The final samples used for the analysis are generated and reconstructed with release 20.7, with full detector modelling; more details about this in section 7.1. The settings used for the tau decay and hadronisation, however, are the same as described in this section.

Higgs production and decay

The Higgs production processes are simulated using Powheg-Box [59–61]. Production via *gg*F [62] and VBF [63] are both evaluated at next-to-leading order (NLO), using the CT10 [64] set of parton density functions. No non-SM physics is assumed in this step. The Higgs decay and subsequent showering and hadronisation is done in Pythia. Since version 8.200, Pythia models full spin correlations in tau decays, for arbitrary values of the mixing parameter ϕ_τ. Replacing the old implementation with isotropic decays, the new sophisticated modelling follows the spin correlation algorithm of Richardson [65], for up to six-body tau decays. The procedure is summarised in [66], and documented in detail in [67]. In brief, the spin correlations are separated from the computation of the hard-scattering matrix element, by initially setting all decay matrices to the identity. Starting from the last decayed particle, the decay matrix is computed, and iteratively going backwards through all decays, the decay is repeated and the decay matrix updated. Finally, after processing all decays, the outgoing particles are all correlated. For a spin-0 particle such as the Higgs, no information about the production process is required to model the decay, apart from its *CP* state, which is set globally. Pythia is used to model the tau decays also in the samples that are later reweighted, but in this case the spin correlations are ignored, and the decays are done isotropically.

Event reweighting

The event reweighting is done using TauSpinner, which is distributed as part of the Tauola library [68, 69]. TauSpinner takes as input the four-momenta of all tau decay products, including the neutrinos, and calculates a per-event spin weight, corresponding to the specified properties of the parent boson. The spin weight is computed on basis of the tau polarimetric vectors, which are uniquely determined by the decay product kinematics, and a spin density matrix, which depends on the ditau production. For Higgs decays, the spin density matrix is diagonal (but with opposite sign) for a pure scalar or pseudoscalar Higgs, but contains off-diagonal elements in the case of *CP* mixing. The full range of mixing parameter values is supported.

6.3.1 Validation of event reweighting procedure

There are three cases to be considered for comparison:

- Pythia version 8.186. This will serve as the reference, as this version contains the sophisticated tau decay algorithm, and is thoroughly validated by the ATLAS Physics Modelling Group (PMG). This was the final Pythia version to be used for MC12 (8 TeV) sample generation campaign. Only SM Higgs decays are supported; this version is also included in the comparison of pseudoscalar decays, but in this case the events are reweighted to the pseudoscalar hypothesis using TauSpinner.
- Pythia version 8.205. This version features full control of Higgs parity, and spin correlations are modelled according to the description in section 6.3. This was, at the time of the study, the most recently released version. It was later validated separately for the MC15 (13TeV) campaign by the PMG.
- Pythia version 8.205, with spin correlations switched off, but re-introduced using TauSpinner weights. TauSpinner version 1.4.0, distributed with Tauola version 1.1.5, is used.

In order to be consistent with the at the time most recent PMG validation status, the comparison is performed at a center-of-mass energy $\sqrt{s} = 8\,\text{TeV}$. Figure 6.4 shows the results for the scalar Higgs scenario, while fig. 6.5 shows the pseudoscalar scenario. The observables plotted here are computed in the true Higgs rest frame, and do in some cases depend on the neutrino momentum vectors. Hence they do not equal the φ^*_{CP} definitions in section 6.2, but the shape and thereby sensitivity to ϕ_τ, is the same. The definition is specified in the caption of each figure. The reference (Pythia8.186) is shown in green, spin correlations modelled by Pythia8.205 in dashed black, and spin correlations modelled by TauSpinner are shown in red. The lower section on each plot indicates the difference with respect to the reference.

No deviation is observed between the modelling of the spin correlations in Pythia and TauSpinner. The event reweighting approach, having the practical benefit of relying only on a single high-statistics signal sample to simulate all mixing scenarios, is implemented for the following analysis. Note that an updated version of TauSpinner is used for the final samples; this does, however, not affect the modelling. The systematic uncertainty of the spin correlation modelling is discussed in section 7.4.

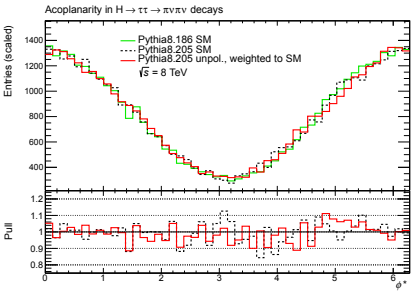

(a) Angle between the tau decay planes spanned by the $\pi^{\pm}$ and ν momentum vectors, in decays to $\pi^{+}\nu\pi^{-}\nu$.

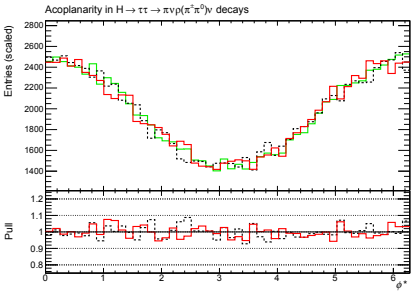

(b) Angle between the tau decay planes spanned by the $\pi^{\pm}$ and ν momentum vectors on one side, and the $\pi^{\pm}$ and π^{0} vectors on the other side, in decays to $\pi^{\pm}\nu\rho^{\mp}(\pi^{\mp}\pi^{0})\nu$.

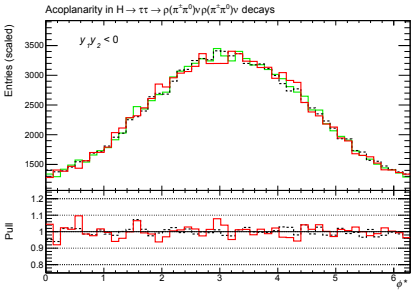

(c) Angle between the tau decay planes spanned by the $\pi^{\pm}$ and π^{0} momentum vectors, in decays to $\rho^{\pm}(\pi^{\pm}\pi^{0})\nu\rho^{\mp}(\pi^{\mp}\pi^{0})\nu$, selecting only events with $y_{+}y_{-} < 0$.

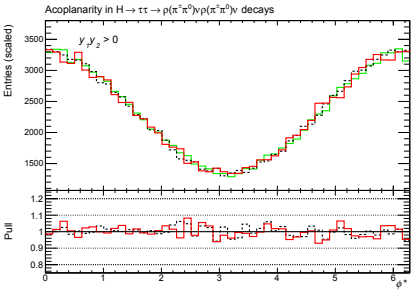

(d) Angle between the tau decay planes spanned by the $\pi^{\pm}$ and π^{0} momentum vectors, in decays to $\rho^{\pm}(\pi^{\pm}\pi^{0})\nu\rho^{\mp}(\pi^{\mp}\pi^{0})\nu$, selecting only events with $y_{+}y_{-} > 0$.

Figure 6.4: Comparison plots for scalar Higgs decays, where the taus decay to (a) $\pi\nu\pi\nu$, (b) $\pi\nu\rho(\pi\pi^{0})\nu$, (c) and (d) $\rho(\pi\pi^{0})\nu\rho(\pi\pi^{0})\nu$.

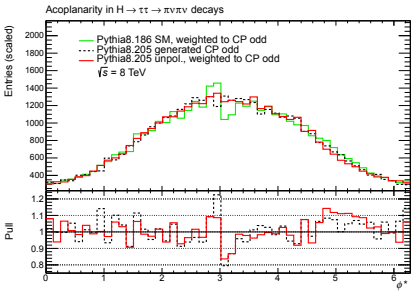

(a) Angle between the tau decay planes spanned by the $\pi^{\pm}$ and ν momentum vectors, in decays to $\pi^{+}\nu\pi^{-}\nu$.

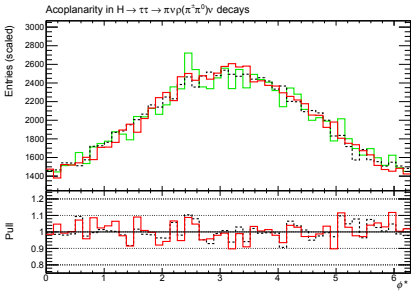

(b) Angle between the tau decay planes spanned by the $\pi^{\pm}$ and ν momentum vectors on one side, and the $\pi^{\pm}$ and π^{0} vectors on the other side, in decays to $\pi^{\pm}\nu\rho^{\mp}(\pi^{\mp}\pi^{0})\nu$.

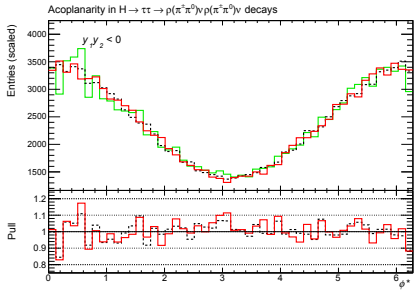

(c) Angle between the tau decay planes spanned by the $\pi^{\pm}$ and π^{0} momentum vectors, in decays to $\rho^{\pm}(\pi^{\pm}\pi^{0})\nu\rho^{\mp}(\pi^{\mp}\pi^{0})\nu$, selecting only events with $y_{+}y_{-} < 0$.

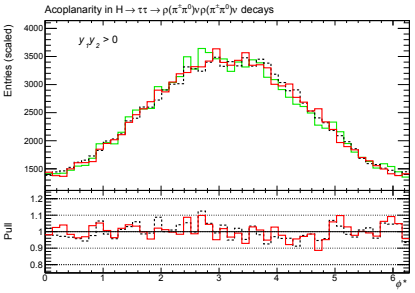

(d) Angle between the tau decay planes spanned by the $\pi^{\pm}$ and π^{0} momentum vectors, in decays to $\rho^{\pm}(\pi^{\pm}\pi^{0})\nu\rho^{\mp}(\pi^{\mp}\pi^{0})\nu$, selecting only events with $y_{+}y_{-} > 0$.

Figure 6.5: Comparison plots for pseudoscalar Higgs decays, where the taus decay to (a) $\pi\nu\pi\nu$, (b) $\pi\nu\rho(\pi\pi^{0})\nu$, (c) and (d) $\rho(\pi\pi^{0})\nu\rho(\pi\pi^{0})\nu$.

Chapter 7

Estimating the sensitivity for measuring *CP* invariance in Higgs decays to tau pairs

The expected performance of a measurement of the Higgs *CP* mixing parameter using the φ^*_{CP} observable, is studied using data and Monte Carlo corresponding to an integrated luminosity of 36.1 fb^{-1}. At the time of submission of this thesis, the results have not been approved by the ATLAS collaboration for public presentation, therefore only the expected final results, and only plots of distributions outside of the signal regions, are shown. The fundamental parts of the analysis are based upon the Run 2 $H \rightarrow \tau\tau$ cross section measurement, which is also, at the time being, not approved by the internal review committee for public release. Apart from the $Z \rightarrow \tau\tau$ background estimate, the cross section measurement builds largely on the Run 1 result [70]. The *CP* invariance measurement, described in this chapter, uses a reweighting technique and fit model inspired by the Run 1 measurement of *CP* invariance in VBF production [71] using $H \rightarrow \tau\tau$ decays. This measurement probed the *HVV* coupling, and is completely independent of *CP* violation in the Yukawa coupling, discussed here. In the same fashion as this VBF analysis, a binned likelihood fit is employed to assess different mixing hypotheses, where the signal template is constructed from Monte Carlo events, reweighted following the procedure described in section 6.3. Although an analytic expression for the φ^*_{CP} distribution as function of the mixing parameter ϕ_τ does exist (eq. (6.3)), the impact of detector reconstruction is not easily parameterised. Using simulation to extract the templates takes into account not only reconstruction effects, which may alter the shape of the template, but also the amplitude difference caused by selection requirements. A limiting factor to this approach is the finite size of the MC samples, and the systematic uncertainties arising from the simulation. Both these points are at least partially mitigated by using a data-driven approach to estimate the contribution from the main background processes.

7.1 Data and Monte Carlo samples

Data

The full dataset from 2015 and 2016 data taking is used, corresponding to a total integrated luminosity of 36.07 fb^{-1}, after rejecting lumiblocks where the detector was not fully operational. Split by year, the datasets contains 3.21 and 32.81 fb^{-1} for 2015 and 2016, respectively.

Signal samples

The signal samples are generated using PowHeg-Box for the Higgs production, and Pythia version 8.212 for the Higgs decay, parton shower and hadronisation. VBF production is simulated with NLO accuracy, while *gg*F is simulated at next-to-next-to-leading order (NNLO). In both cases the `PDF4LHC15` [72] parametrisation of the parton density function is used, with the `AZNLO` [73] tune. The hadronisation part uses the `CTEQ6L1` [74] PDF set. QED emissions from electroweak vertices and charged leptons are simulated with Photos [75] version 3.61. The production cross section numbers are provided by the LHC Higgs Cross Section Working Group [76], computed at N^3LO QCD accuracy [4] for *gg*F and NNLO [77] for VBF, in both cases with NLO electroweak corrections. The spin correlation between the taus from the Higgs decay is disabled in Pythia, and re-introduced using event weights computed by TauSpinner version 2.0.3.

Background MC samples

All electroweak production of W and Z bosons is simulated using Sherpa [78] version 2.2.1. This includes the important, irreducible $Z \to \tau\tau$ background, W produced along with jets, and diboson production. Single-boson production in association with jets is computed at NLO QCD and electroweak precision for up to and including two jets, and at LO for ≥ 3 jets [79]. The `NNPDF30NNLO` [80] PDF set is used for these processes.

Top pair and single-top production is simulated in PowHeg-Box using the `CT10` [64] PDF set, interfaced to Pythia version 6.428 for the parton shower. Pythia is configured with the `CTEQ6L1` PDF set and the `Perugia2012` tune [81]. The list of individual samples considered for the analysis are shown in table 7.1.

All MC samples include a full simulation of the interaction with the detector material, using Geant4 [82], and a subsequent emulation of detector and trigger response [83]. The samples are reconstructed using the same Athena software version as used for data. In order to correctly account for effects from pile-up, all events are overlaid with simulated minimum-bias interactions. These interactions include double-, single- and non-diffractive pp collisions, simulated in Pythia8 using the `MSTW2008LO` [84] PDF set with `A2` [85] tunes. The minimum-bias overlay is added randomly so that the distribution of number of pile-up vertices match that observed in data.

Table 7.1: Signal and background Monte Carlo samples considered for this analysis. Under 'Generator', 'ME' gives the MC generator used to calculate the matrix element of the hard scattering, while 'PS' indicates the generator used for the parton showering. The PDF column lists the PDF used for the hard scattering; the parton showering may involve a different PDF.

Process	Generator		PDF	$\sigma \times \mathscr{B}$ [pb]
	ME	PS		
$gg\mathrm{F}\ H \to \tau\tau$	PowHeg	Pythia	PDF4LHC15	0.57338706
VBF $H \to \tau\tau$	PowHeg	Pythia	PDF4LHC15	0.0468777389
$Z \to \tau\tau$	Sherpa2.2.1		NNPDF30NNLO	2550.9
$Z \to \ell\ell$, $\ell = \mu, e$	Sherpa2.2.1		NNPDF30NNLO	9004.4
W + jets	Sherpa2.2.1		NNPDF30NNLO	59650.3
$t\bar{t}$ and single top	PowHeg	Pythia6	CT10	981.5
Diboson	Sherpa2.2.1		CT10	99.8

7.2 Event selection

The event selection follows the $H \to \tau\tau$ cross section analysis closely, but with a more specific final state and with dedicated signal regions. Events are selected by a hadronic di-tau trigger, which in 2015 data taking was
`HLT_tau35_medium1_tracktwo_tau25_medium1_tracktwo_L1TAU20IM_2TAU12IM`,
while in 2016 the trigger was `HLT_tau35_medium1_tracktwo_tau25_medium1_tracktwo`. A detailed description of the tau trigger algorithm can be found in [86]. The triggers listed here are both unprescaled. Because of the increase in instantaneous luminosity between 2015 and 2016, the 2016 trigger requires an event signature of two hadronic tau candidates and an additional L1 jet, where the jet must satisfy $p_{\mathrm{T}} > 25\,\mathrm{GeV}$ and $|\eta| < 3.2$. The trigger efficiency is low for jets just above the p_{T} threshold, and reaches the plateau of full efficiency only at around 70 GeV. To avoid potential mismodelling due to the trigger turn-on curve, the offline reconstructed jet p_{T} is required to be greater than 70 GeV, as well have $|\eta| < 3.2$. The leading jet in the event is further required to be within $\Delta R < 0.4$ of the online jet that passed the trigger. To ensure a consistent selection between the 2015 and 2016 datasets, this jet requirement is applied also in 2015 data.

A set of minimal requirements is used to define a preselection region, which is background dominated and will be used for background estimation and validation of the background modelling. All signal regions are subsets of the events passing preselection. Events are required to have exactly two hadronic tau candidates passing the *medium* identification criterion, and at least one must also pass the *tight* criterion. The candidates must be oppositely charged. Only tau candidates classified as one-prong, with either zero or one associated π^0, are selected. Events with electrons or muons are rejected. The leading tau candidate must have transverse momentum greater than 40 GeV, and the subleading candidate greater than 30 GeV, which is at the plateau of the trigger efficiency curve. Both candidates must be associated to the same primary vertex. Topological requirements are imposed to further reduce background: the angular distance between the tau candidates must satisfy $0.8 < \Delta R < 2.4$, and the

distance in pseudorapidity, $\Delta\eta$, must be less than 1.5. Since neutrinos from the tau decays are expected, a requirement on the missing transverse energy is imposed, of $E_{\mathrm{T}}^{\mathrm{miss}} > 20\,\mathrm{GeV}$. The neutrinos are further expected to be aligned with the direction of the tau candidate. This is ensured by computing the fraction of momenta carried away by the visible decay products, using the collinear approximation. The fraction is required to be between 0.1 and 1.0 for both tau candidates. Finally, the reconstructed invariant Higgs mass is required to lie in the interval $70 < m_{\tau\tau}^{\mathrm{MMC}} < 150\,\mathrm{GeV}$. Distibutions of essential tau candidate and event observables are shown in figs. 7.1 and 7.2, respectively.

The signal regions are split to target the VBF and ggF production modes separately. The VBF region consists of events with at least two jets with $p_{\mathrm{T}} > 30\,\mathrm{GeV}$, where the pseudorapidity difference between the two leading jets satisfy $\Delta\eta_{jj} > 3.0$. Both tau candidates are required to lie between the two leading jets in pseudorapidity, and the product of the two jet pseudorapidities must be negative. The invariant mass of the two jets, m_{jj}, is required to be greater than 400 GeV.

The *boosted* region targets Higgs bosons produced with high p_{T}, typically recoiling off a hard jet produced together with the Higgs in gluon-gluon fusion. The boosted region consists of events passing preselection, but failing the VBF selection, and where the reconstructed Higgs transverse momentum is greater than 100 GeV. The Higgs transverse momentum p_{T}^{H} is defined as the magnitude of the vector sum of the transverse tau and missing energy momentum,

$$\boldsymbol{p}_{\mathrm{T}}^{H} = \boldsymbol{p}_{\mathrm{T}}^{\tau^{+}} + \boldsymbol{p}_{\mathrm{T}}^{\tau^{-}} + \boldsymbol{E}_{\mathrm{T}}^{\mathrm{miss}}\,. \tag{7.1}$$

The boosted region is further split in a signal-enriched high-p_{T} region, requiring $p_{\mathrm{T}}^{H} > 175\,\mathrm{GeV}$. Events failing this selection are assigned to a low-p_{T} boosted category. A summary of the different selection categories is given in table 7.2.

Each of the VBF and boosted regions are further divided into subcategories depending on the decay modes of the tau candidates. The category naming is given according to the method used to reconstruct φ_{CP}^{*}:

- **IP-IP** contains events where both taus have one charged but no neutral component, where the IP method (section 6.2.1) is used to construct the decay planes of both taus,

- **IP-$\boldsymbol{\rho}$** contains events where one tau has a neutral component but the other does not, so the combined IP and ρ method (section 6.2.3) is used, and

- **$\boldsymbol{\rho}$-$\boldsymbol{\rho}$** contains events where both taus have neutral component, and the ρ method is used (section 6.2.2).

Two non-overlapping mass regions are defined, where the Higgs signal region is bounded by $100 < m_{\tau\tau}^{\mathrm{MMC}} < 150\,\mathrm{GeV}$, while a separate Z control region is defined by $70 < m_{\tau\tau}^{\mathrm{MMC}} < 100\,\mathrm{GeV}$. The Z mass interval is used to obtain the data-driven $Z \to \tau\tau$ background template, while the final fit is performed in the Higgs signal region.

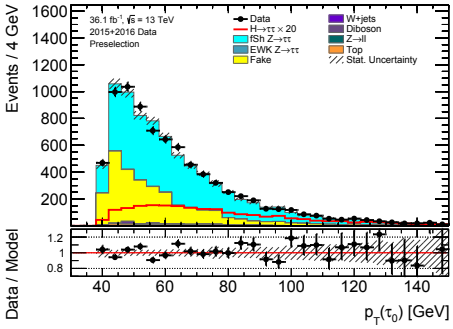

(a) Leading τ p_{T}

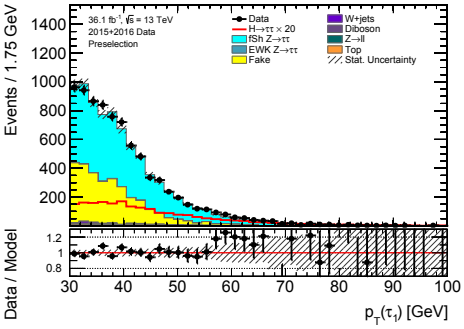

(b) Subleading τ p_{T}

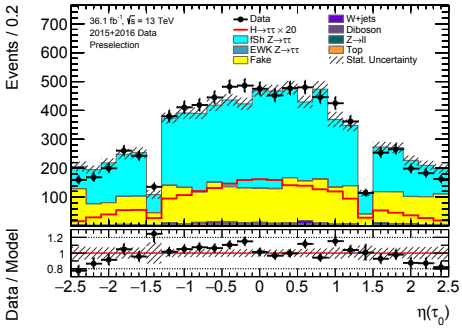

(c) Leading τ pseudorapidity

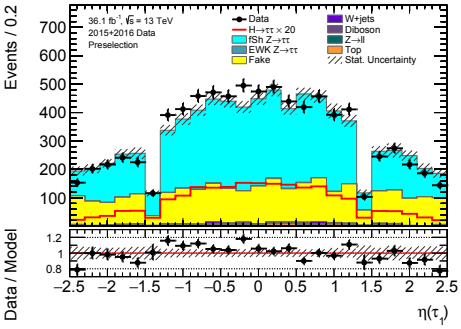

(d) Subleading τ pseudorapidity

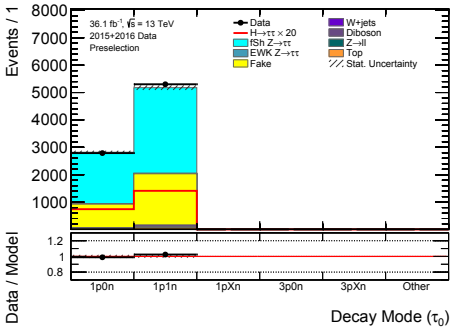

(e) Leading τ decay mode

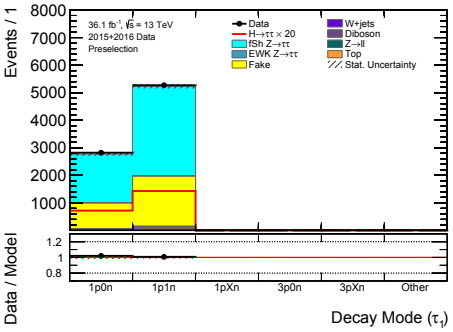

(f) Subleading τ decay mode

Figure 7.1: p_{T}, η and decay mode of the leading and subleading tau candidates, at preselection. The uncertainties are statistical only.

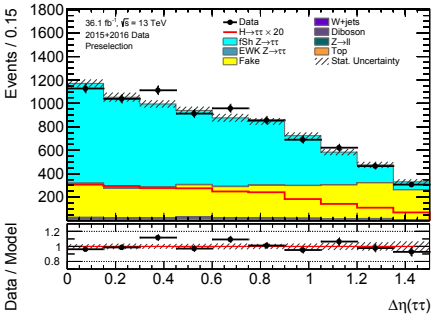

(a) $\Delta\eta_{\tau\tau}$

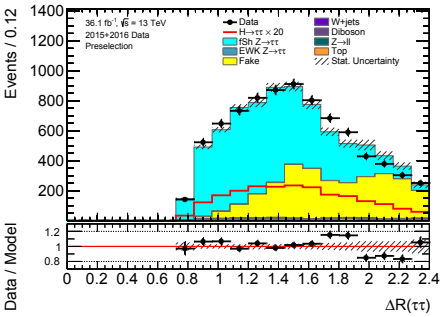

(b) $\Delta R_{\tau\tau}$

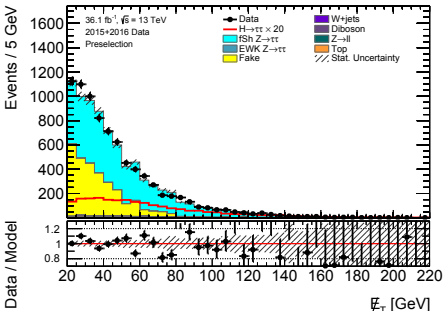

(c) $E_{\mathrm{T}}^{\mathrm{miss}}$

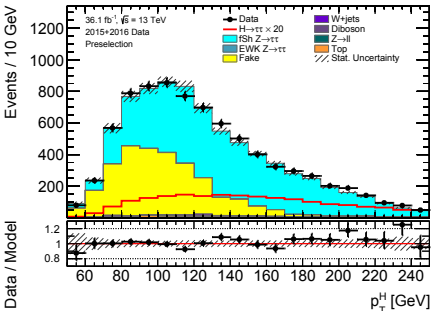

(d) p_{T}^{H}

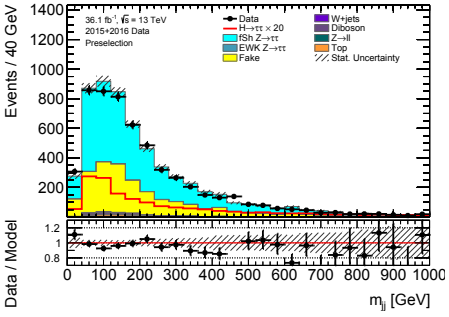

(e) Dijet invariant mass m_{jj}, for events with ≥ 2 jets

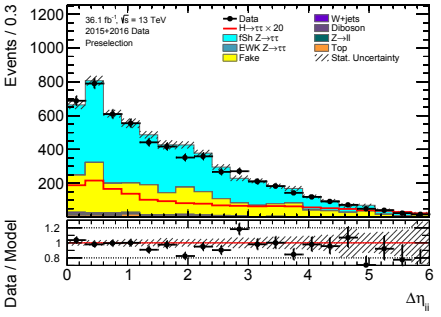

(f) Dijet pseudorapidity difference $\Delta\eta_{jj}$, for events with ≥ 2 jets

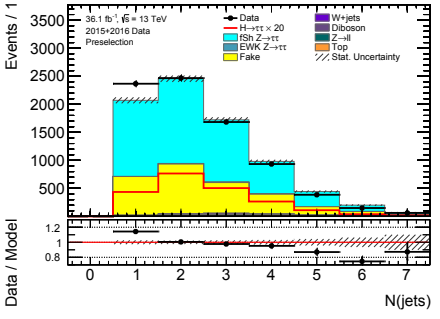

(g) Number of jets

Figure 7.2: Event-level observables, at preselection level.

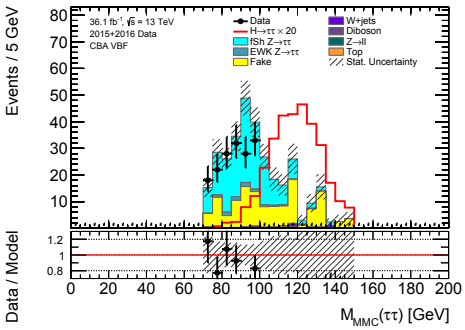

(a) VBF

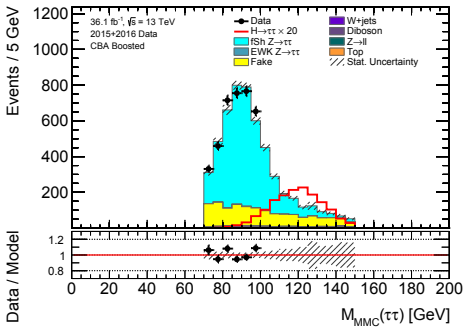

(b) Boosted inclusive

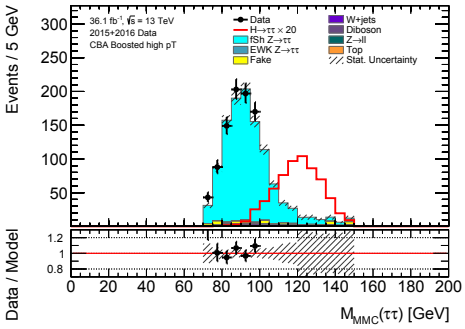

(c) Boosted high p_{T}

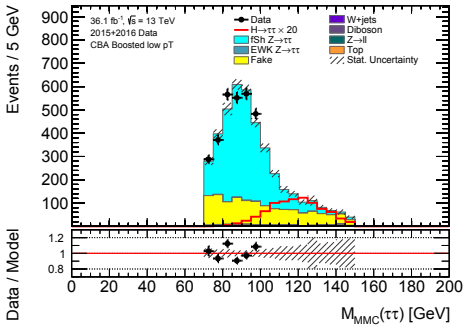

(d) Boosted low p_{T}

Figure 7.3: Invariant mass distributions for the VBF and boosted signal regions.

Table 7.2: Overview of the event selection.

Event selection and categorisation				
Preselection				
Exactly two τ_{had} candidates passing *medium* identification, ≥ one must also pass *tight*				
One jet with $p_{\text{T}} > 70\,\text{GeV}$, $\lvert\eta\rvert < 3.2$				
Both τ candidates classified as one-prong, 0 or 1 π^0				
Both τ candidates matched to same primary vertex				
Leading τ $p_{\text{T}} > 40\,\text{GeV}$, subleading τ $p_{\text{T}} > 30\,\text{GeV}$				
Topological requirements: $\Delta\eta_{\tau\tau} < 1.5$ and $0.8 < \Delta R_{\tau\tau} < 2.4$				
$E_{\text{T}}^{\text{miss}} > 20\,\text{GeV}$				
Reconstructed mass in the interval $70 < m_{\tau\tau}^{\text{MMC}} < 150\,\text{GeV}$				
No electrons or muons				
Fraction of visible τ momentum, calculated using collinear approximation: $0.1 < x_1 < 1.4, 0.1 < x_2 < 1.4$				
VBF region	**Boosted region**			
≥ two jets, subleading jet $p_{\text{T}} > 30\,\text{GeV}$	Failed VBF selection			
$\lvert\Delta\eta_{jj}\rvert > 3.0$, $\eta(j_1) \times \eta(j_2) < 0$	$p_{\text{T}}^H > 100\,\text{GeV}$			
$m_{jj} > 400\,\text{GeV}$				
Both τ candidates lie between the jets in η	**Boosted high-p_{T}** $p_{\text{T}}^H > 175\,\text{GeV}$		**Boosted low-p_{T}** $p_{\text{T}}^H < 175\,\text{GeV}$	
Decay mode selection				
IP-IP	**IP-ρ**		**ρ-ρ**	
1p0n, 1p0n	1p0n, 1p1n		1p1n, 1p1n	
	High d_0^{sig}/y	**Low d_0^{sig}/y**	**High y_+y_-**	**Low y_+y_-**
No further splitting	$d_0^{\text{sig}}(\tau_{\text{1p0n}}) > 1.4$ and $y(\tau_{\text{1p1n}}) > 0.3$	$d_0^{\text{sig}}(\tau_{\text{1p0n}}) < 1.4$ or $y(\tau_{\text{1p1n}}) < 0.3$	$\lvert y_+y_-\rvert > 0.2$	$\lvert y_+y_-\rvert < 0.2$

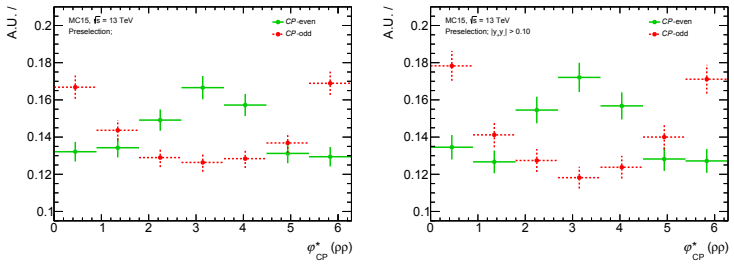

(a) No requirement on $|y_+y_-|$

(b) $|y_+y_-| > 0.10$

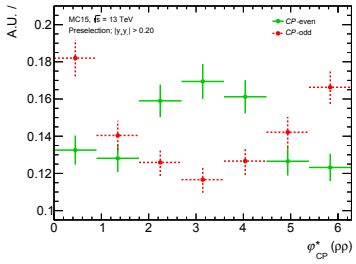

(c) $|y_+y_-| > 0.20$

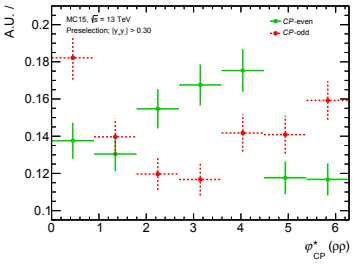

(d) $|y_+y_-| > 0.30$

Figure 7.4: Distributions of φ^*_{CP} using the ρ-ρ method, for increasing minimum requirements on $|y_+y_-|$.

7.2.1 Per decay mode optimisation

The amplitude of the φ^*_{CP} distribution depends on the reconstruction method, but also on the kinematics of the tau decays. For each method, several observables have been studied to investigate the correlation with φ^*_{CP}.

For $\tau \to \rho\nu$ decays, the sensitivity to the tau polarisation is found to be larger for higher absolute values of the charged-to-neutral energy difference y, defined in eq. (6.9). This can be understood from eqs. (6.10) and (6.13): if y_+ and/or y_- is close to 0, one can easily reconstruct it with wrong sign, hence choosing the wrong phase in the φ^*_{CP} definition. To mitigate this, while still retaining all signal events, events reconstructed using the ρ-ρ method are divided into a high-sensitivity category, requiring $|y_+y_-| > 0.2$, and a low-sensitivity category, defined by $|y_+y_-| < 0.2$. This threshold is optimised by running the full fit procedure described in section 7.5, using only ρ-ρ events, and varying the y_+y_- requirement to find the value resulting in the highest sensitivity to ϕ_τ. The φ^*_{CP} distributions at preselection, for increasing $|y_+y_-|$ thresholds, are shown in fig. 7.4.

The IP-IP method can suffer from poor performance if the impact parameter vectors are small, or of similar magnitude, compared to the uncertainty on the primary vertex position. The best improvement is found to be a requirement on the significance of the transverse track impact parameter d_0, denoted d_0^{sig}, which is defined as d_0 divided by its uncertainty in the vertex fit. Figure 7.5 shows the φ^*_{CP} distribution for events reconstructed with the IP-IP method, at preselection, for increasing d_0^{sig} values of both tau candidates. The highest increase in sensitivity is found for a d_0^{sig}

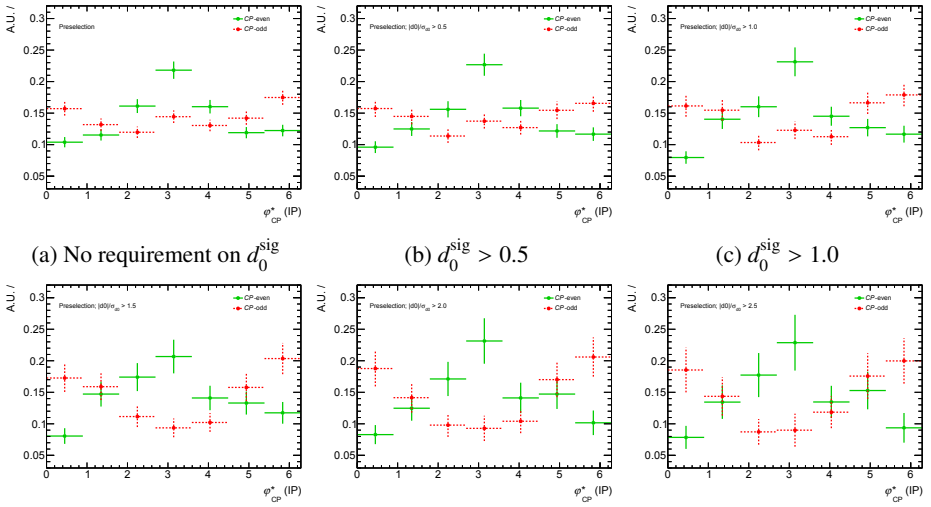

(a) No requirement on d_0^{sig} (b) $d_0^{\text{sig}} > 0.5$ (c) $d_0^{\text{sig}} > 1.0$

(d) $d_0^{\text{sig}} > 1.5$ (e) $d_0^{\text{sig}} > 2.0$ (f) $d_0^{\text{sig}} > 2.5$

Figure 7.5: Distributions of φ^*_{CP} using the IP method, for increasing minimum requirements on d_0^{sig}.

requirement greater than 1.4 for both tau candidates. With the low statistics available in the current dataset, however, splitting $\tau \to \pi\nu$ events into subcategories is not feasible. The study is left for future reference, and the IP-IP category is kept as-is.

For the combined IP-ρ method, the higher branching ratio does allow for a division into high- and low-sensitivity categories. The d_0^{sig} requirement of 1.4 is applied to the $\tau \to \pi\nu$ candidate, while the $|y|$ value of the $\tau \to \pi\pi^0\nu$ candidate is optimised. Requiring $|y| > 0.3$ is found is found to give the highest expected sensitivity.

7.3 Background estimation

The backgrounds can be separated into processes involving two real taus, processes involving one real tau and one QCD jet misidentified as a tau, and events where both tau candidates are misidentified jets.

The first category is by far dominated by $Z \to \tau\tau$ decays, but also includes a small contribution from top pair production and diboson events with two real taus in the final state. Events with one real tau originate from electroweak production of W together with jets, and single top production. All electroweak and top processes are estimated from MC simulations, and are, since their combined contribution is comparatively small, grouped into a single class named *Others*. Events where both tau candidates are faked by jets, for simplicity called *fakes*, constitute the second most important background.

Both the fake tau background and $Z \to \tau\tau$ is modelled using a data-driven approach. To avoid overlap between events with one and two fake tau candidates, events from MC are requested to contain at least one hadronically decaying tau in the

truth record, and this must be the same object as the tau candidate is reconstructed from. The normalisation of all samples in the *Others* category is taken from the MC generator cross section calculation, listed in table 7.1.

7.3.1 Estimation of fake tau background from QCD jets

The shape template for fake taus is obtained from data in the respective signal regions, by inverting the ditau opposite-sign (OS) charge requirement, and selecting instead events with same sign (SS). The distribution of $m_{\tau\tau}^{\text{MMC}}$ and φ_{CP}^{*} in the same-sign region, at preselection and in the VBF and boosted categories, is shown in fig. 7.6. The contribution from events with one or more real tau decay is small, but to avoid double counting of these events, the same-sign contribution in all MC backgrounds are subtracted from the fake template. This procedure introduces a dependence on the MC sample statistics, which is accounted for by a shape uncertainty on the fake template, determined by varying the MC contribution up and down within its total statistical uncertainty. The impact of this uncertainty is typically less than 5% of the fake yield.

A second source of systematic uncertainty comes from the extrapolation of the SS templates to the OS regions. To estimate this uncertainty, an alternative method of extracting the fake templates is used, which is to define an *anti-ID* control region. This region consists of OS events where both taus pass the *medium* identification threshold, but both fail *tight* identification. Since the anti-ID region has a large contamination of processes with true tau decays, it is not chosen as the nominal region to extract the fake templates, but it does still provide means of evaluating the SS to OS extrapolation procedure. The shape uncertainty is estimated by taking the difference between the SS and anti-ID distributions at preselection, for IP-IP, IP-ρ and ρ-ρ events separately.

7.3.2 Estimation of $Z \to \tau\tau$ background

The shape templates for $Z \to \tau\tau$ are in each region constructed from events passing all selection criteria, but lie in a mass interval around the Z peak, $70 < m_{\tau\tau}^{\text{MMC}} < 100\,\text{GeV}$. Templates for fakes and all MC samples, in this mass region, are subtracted to avoid double counting. Taking the Z template from data is beneficial for two reasons; first, one avoids the theory uncertainties from the choice of QCD parameters (such as renormalisation scale, factorisation scale and PDF), which can be substantial, and second, selecting events at the Z peak ensures a large sample size. The distributions of φ_{CP}^{*} for $70 < m_{\tau\tau}^{\text{MMC}} < 100\,\text{GeV}$ is shown in fig. 7.7.

The validity of porting the Z template from the low-mass interval to the Higgs mass interval is tested by comparing the φ_{CP}^{*} distribution between the two at generator level, no selection requirements applied, using the SHERPA MC sample. The comparison, done for the three relevant decay mode combinations separately, is shown in fig. 7.8. At NLO precision, there is no apparent discrepancy. However, to account for differences introduced by reconstruction and phase space selection, an uncertainty on the mass range extrapolation is assigned by performing the same comparison at preselection, and propagating the difference to all signal regions. This is again done separately for the different decay modes.

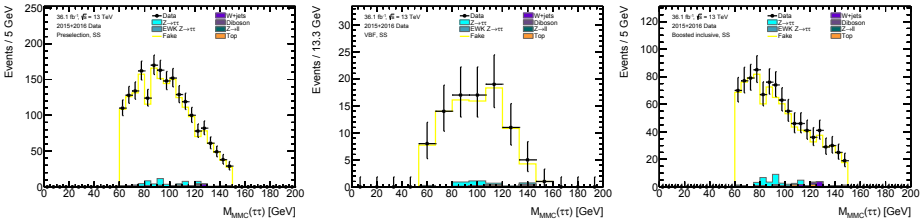

(a) Preselection (b) VBF category (c) Boosted inclusive category

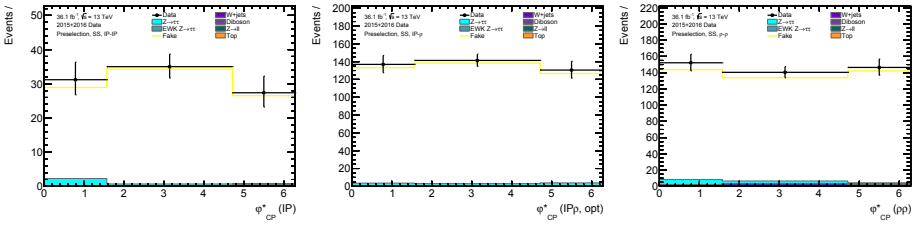

(d) Preselection, IP-IP method (e) Preselection, IP-ρ method (f) Preselection, ρ-ρ method

Figure 7.6: Distributions of $m_{\tau\tau}^{\mathrm{MMC}}$ and φ_{CP}^{*} in the same-sign region. Same-sign events from decays with two real taus are overlaid. The templates used for fake tau background is the yellow line, corresponding to the distribution in data, subtracted the distribution in MC.

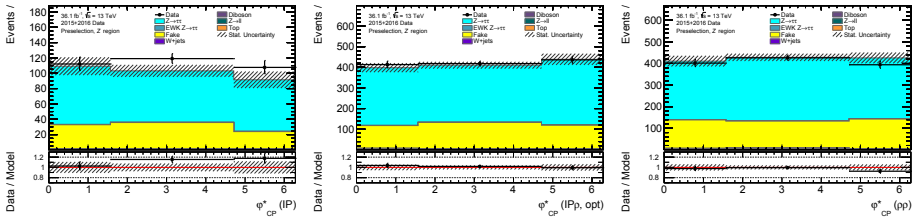

(a) Preselection, IP-IP method (b) Preselection, IP-ρ method (c) Preselection, $\rho - \rho$ method

Figure 7.7: Distributions of φ_{CP}^{*} in the Z mass region, $70 < m_{\tau\tau}^{\mathrm{MMC}} < 100\,\mathrm{GeV}$, at preselection.

The uncertainty on the subtraction procedure follows the same prescription as for the fake-tau template, where the subtracted processes are varied up and down by their statistical uncertainty.

7.3.3 Normalisation of data-driven background templates

The normalisation of the Z and fakes templates is determined from a fit to the distribution of $\Delta\eta_{\tau\tau}$ in data in the preselection region, using MC for the Z histogram. The signal yield at preselection is less than 1%, and is ignored. In this fit the minimum requirement on $\Delta\eta_{\tau\tau}$ is raised to 2.0, which gives a strong handle on the normalisation of fakes. As can be seen in fig. 7.9, the highest two bins have virtually zero contribution from other backgrounds. The separate normalisation factors for the fake tau and Z contributions are unconstrained, while the normalisation for the remain-

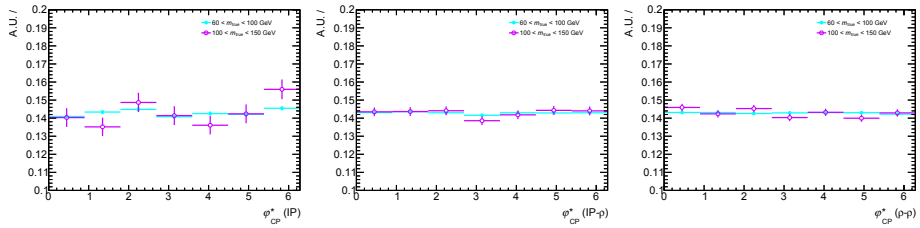

(a) IP-IP method (b) IP-ρ method (c) ρ-ρ method

Figure 7.8: Comparison of the φ^*_{CP} distribution in MC at generator level, in the Higgs (purple) and the Z (blue) mass regions. No selection criteria apart from the mass selection are applied.

ing backgrounds are fixed at their theoretical prediction. Normalisation factors of $r_Z = 0.98 \pm 0.04$ for the Z contribution and $r_{\text{QCD}} = 1.66 \pm 0.10$ for the fake tau contribution are obtained. The r_Z value being close to one shows that the cross section estimate from Sherpa is accurate with respect to data. This is important, as the event yield from MC is needed to correctly normalise the φ^*_{CP} templates in the Higgs mass region. The procedure to extract and normalise the data-driven background templates can be outlined as follows:

1. The $\Delta\eta_{\tau\tau}$ fit is performed at preselection in the full mass range $70 < m^{\text{MMC}}_{\tau\tau} < 150\,\text{GeV}$, and the normalisation factors r_Z and r_{QCD} are extracted.

2. In the VBF and boosted signal regions, in the Z mass range, φ^*_{CP} histograms for fakes are created from SS data, and scaled by r_{QCD}. Histograms for Z are created from OS data, and the histograms for fakes and other backgrounds are subtracted. The Z histograms will be used as templates in the final fit; the histograms from fakes and other backgrounds in the Z mass range are only used for the subtraction.

3. In the VBF and boosted signal regions, now in the Higgs mass range, histograms for fakes are created from SS data, and scaled by r_{QCD}. The yield of Z events in MC is extracted, and scaled by r_Z, to account for the difference between MC and data. The Z histograms from the previous step is scaled to this yield, and used as templates for the φ^*_{CP} distribution in Z events. Histograms from other backgrounds are created from MC.

Theoretical uncertainties affecting the $Z \to \tau\tau$ cross section are incorporated in the fit. The resulting uncertainty on the Z and fake-tau normalisations are propagated on to the final φ^*_{CP} fit. The expected numbers of signal and background events, after background normalisation, are given for all event categories in table 7.3.

7.4 Systematic uncertainties

This section describes the systematic uncertainties affecting the analysis. These are divided into experimental uncertainties, related to detector and reconstruction effects,

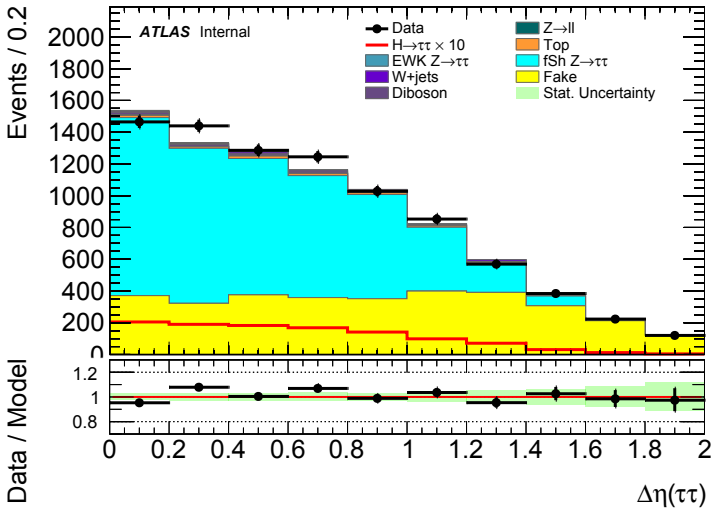

Figure 7.9: Background fit to the $\Delta\eta_{\tau\tau}$ distribution. The normalisation of the $Z \to \tau\tau$ contribution modelled by MC (in blue) and the fake tau contribution (in yellow) are fitted, while the remaining background contributions are fixed to their theoretical predictions.

Table 7.3: Event yields for the different samples considered, at preselection and in the signal regions.

Sample	Category					
	Preselection	VBF inclusive	VBF IP-IP	VBF IP-rho	VBF rhorho	
VBFH	25.9±0.3	11.8±0.2	1.2±0.1	4.9±0.1	4.9±0.1	
ggH	72.5±1.1	4.0±0.3	0.4±0.1	1.5±0.2	1.7±0.2	
Sum signal	98.3±1.2	15.8±0.3	1.6±0.1	6.4±0.2	6.5±0.2	
Fake	3265.4±73.5	152.0±15.9	3.3±2.3	39.7±8.1	26.4±6.6	
$Z \to \tau\tau$	5153.7±68.6	184.1±9.3	3.8±1.9	26.6±3.9	19.6±3.0	
Others	190.0±17.5	7.6±2.2	0.2±0.1	0.7±0.8	4.4±1.9	
Data	8696.0±93.3	298.0±17.3	20.0±4.5	50.0±7.1	43.0±6.6	
Sum bgnd	8609.1±102.0	343.8±18.5	7.3±3.0	67.0±9.0	50.5±7.5	
Sample	Boost high-p_T, inclusive	Boost high-p_T, IP-IP	Boost high-p_T, IP-rho high d_0^{sig}/y	Boost high-p_T, IP-rho low d_0^{sig}/y	Boost high-p_T, rho-rho high y_0y_1	Boost high-p_T, rho-rho low y_0y_1
VBFH	4.8±0.1	0.5±0.0	0.8±0.1	1.3±0.1	0.8±0.1	1.0±0.1
ggH	23.1±0.6	2.1±0.2	3.8±0.3	6.3±0.3	4.3±0.3	5.0±0.3
Sum signal	27.9±0.6	2.6±0.2	4.7±0.3	7.7±0.3	5.2±0.3	6.1±0.3
Fake	67.8±10.6	0.0±0.0	3.3±2.3	5.0±2.9	6.6±3.3	16.5±5.2
$Z \to \tau\tau$	1053.6±20.8	39.9±4.3	47.4±4.6	73.2±5.0	48.4±4.6	53.1±4.9
Others	38.8±4.8	2.6±1.3	3.2±1.1	7.9±2.0	1.5±2.0	1.7±2.6
Data	1236.0±35.2	57.0±7.5	58.0±7.6	98.0±9.9	66.0±8.1	98.0±9.9
Sum bgnd	1160.1±23.8	42.5±4.4	53.9±5.3	86.0±6.1	56.5±6.0	71.4±7.6
Sample	Boost low-p_T, inclusive	Boost low-p_T, IP-IP	Boost low-p_T, IP-rho d_0^{sig}/y	Boost low-p_T, IP-rho d_0^{sig}/y	Boost low-p_T, rho-rho y_0y_1	Boost low-p_T, rho-rho y_0y_1
VBFH	6.9±0.2	0.7±0.1	1.1±0.1	2.0±0.1	1.1±0.1	1.4±0.1
ggH	33.4±0.8	3.4±0.3	4.7±0.3	9.0±0.4	6.0±0.3	7.2±0.4
Sum signal	40.4±0.8	4.1±0.3	5.8±0.3	11.0±0.4	7.1±0.3	8.5±0.4
Fake	1517.0±50.1	43.0±8.4	59.5±9.9	196.6±18.0	102.5±13.0	175.2±17.0
$Z \to \tau\tau$	2912.5±50.7	103.3±11.1	107.4±8.6	205.8±12.3	139.9±9.9	151.5±20.9
Others	103.0±13.1	4.3±1.6	5.6±1.5	19.0±5.8	14.8±6.3	7.3±5.6
Data	4518.0±67.2	139.0±11.8	178.0±13.3	427.0±20.7	242.0±15.6	322.0±17.9
Sum bgnd	4532.5±72.5	150.6±14.0	172.5±13.2	421.5±22.6	257.1±17.5	334.0±27.6

and theory uncertainties, which are related to the underlying assumptions of the simulations.

7.4.1 Experimental uncertainties

Uncertainties related to reconstruction of physics objects are provided by the Combined Performance working groups, and are implemented in the analysis through a common software framework. The uncertainties are evaluated on a per-object basis, so to evaluate the uncertainty on for instance the jet energy scale, all jets in an event are varied by $\pm 1\sigma$ of the prescribed value, and observables are recalculated. The systematic uncertainties related to the background estimate method are discussed in section 7.3.

Jet uncertainties

The uncertainty on the jet energy resolution and jet energy scale depend on p_{T} and pseudorapidity of the reconstructed jet, and is estimated through data and MC comparisons [87]. Different MC samples, corresponding to variations of the hadronic shower model, calorimeter noise thresholds, and detector configuration, are used to derive the uncertainty. To account for differences in energy resolution between data and simulation, jets in MC are smeared by a p_{T} and η dependent scaling factor. The JER uncertainty is parametrised by the full set of 11 nuisance parameters provided by the JetEtMiss working group, while for the JES uncertainty, a reduced set of 21 nuisance parameters is used. In addition, the uncertainty on the efficiency of the jet vertex tagger is included.

Tau uncertainties

Like for jets, uncertainties on the tau energy scale (TES) are derived using both simulations and data. Uncertainties arising specifically from the detector modelling and hadronic shower model are estimated from alternative MC samples.

Uncertainties related to the tau identification efficiency are estimated from tag-and-probe analyses [88], and include nuisance parameters for trigger efficiency, reconstruction efficiency, and misidentification of electrons as hadronic taus.

Currently, the Tau Working Group does not provide an uncertainty estimate of the resolution of the π^0 momentum vector from the particle flow algorithm. This is acknowledged as a limitation to the analysis; deriving an estimate independently of the Tau WG is, however, not considered a feasible option.

$E_{\mathrm{T}}^{\mathrm{miss}}$ uncertainties

The uncertainties on the objects used to compute the $E_{\mathrm{T}}^{\mathrm{miss}}$ are propagated through the calculation, but additional uncertainties enter in the soft term. These uncertainties, on the resolution and the scale of the $E_{\mathrm{T}}^{\mathrm{miss}}$, are derived by the Jet/EtMiss group using data-driven methods [89].

Track uncertainties

Uncertainties on the resolution of the transverse and longitudinal track impact parameters, d_0 and z_0, are derived from data-MC comparisons and parametrised as function of p_{T} and pseudorapidity. These directly affect the calculation of φ^*_{CP} in the IP and ρ methods. Separate nuisance parameters are introduced for the uncertainty caused by dead inner detector modules, and for the general mismeasurement. A p_{T} and η-dependent smearing is applied to tracks in simulation, so that the resolution matches that observed in data. Additional uncertainties arise from the detector alignment, since certain types of deformation are difficult or even impossible to account for in the alignment procedure [90]. These affect the track impact parameters as well as the momentum [17].

Luminosity and pile-up

The uncertainty on the combined integrated luminosity for the 2015 and 2016 dataset amounts to 2.2%.

As mentioned in section 7.1, all simulated events are overlaid with pile-up interactions, where the number of pile-up vertices is sampled from a generalised μ profile. For the profile in simulations to match that of data, MC events are reweighted by a correction factor of $1/(1.16^{+0.07}_{-0.16})$.

7.4.2 Theory uncertainties

With the use of data-driven estimation methods for the two main backgrounds, and the contributions from remaining backgrounds being less than 4% in the signal regions, no generator uncertainties on the background φ^*_{CP} modelling are necessary. Theory uncertainties on the $Z \to \tau\tau$ contribution are included in the background estimation procedure; these affect the normalisation and also the shape of the $\Delta\eta_{\tau\tau}$ distribution. More specifically, they are computed on basis of varying the renormalisation scale, the factorisation scale, and the parametrisation of the PDF and the strong coupling constant [91].

A shape uncertainty on the signal is assigned by comparing the φ^*_{CP} modelling of TauSpinner and Pythia8. The compatibility between the two has already been checked thoroughly in section 6.3.1, but the comparison is now redone in the analysis-specific region of phase-space. The uncertainty estimate is obtained by inverting the TauSpinner reweighting: A signal sample with SM spin correlations is weighted by the reciprocal of the TauSpinner weight corresponding to the SM hypothesis. This removes the spin correlation in the sample, ideally resulting in a uniform φ^*_{CP} distribution. The deviation from a flat distribution is taken as a general shape uncertainty, applied to all mixing scenarios. The procedure was suggested by the TauSpinner authors. Since the signal strength is not considered a parameter of interest, no uncertainty on the signal cross section is taken into account.

The impact of each systematic uncertainty on the event yields, at preselection level, is quantified in table 7.4. The impact on the fit is evaluated in section 7.6.

Table 7.4: Impact on event yields at preselection, for the different systematic uncertainties considered. Track uncertainties do not affect the yields, and are therefore not listed.

NP	Signal	Fake	$Z \to \tau\tau$	Others
Nominal	98.3	3141.0	5241.2	226.8
fake_contamination	+0.0 / 0.0	−38.7 / +38.7	+0.0 / 0.0	+0.0 / 0.0
jet_fjvteff	+0.2 / −0.2	+0.3 / −0.3	+8.7 / −8.7	+0.6 / −0.6
jet_jer_crosscalibfwd	1.0 / −1.0	2.8 / −2.8	4.8 / −4.8	+2.9 / −2.9
jet_jer_noisefwd	1.0 / −1.0	3.1 / −3.1	12.7 / −12.7	+2.8 / −2.8
jet_jer_np0	+1.2 / −1.2	+112.4 / +112.4	+19.7 / −19.7	−1.4 / +1.4
jet_jer_np1	−0.2 / +0.1	−1.9 / +36.0	−27.4 / +2.3	+0.1 / −0.2
jet_jer_np2	+0.1 / −0.2	+64.2 / −5.9	+0.6 / −12.1	−0.2 / +2.7
jet_jer_np3	+0.3 / −0.4	−8.4 / +14.2	+4.1 / −27.4	−6.9 / +1.1
jet_jer_np4	−0.4 / +0.2	+40.7 / −3.7	−38.1 / +15.0	+2.9 / −1.4
jet_jer_np5	−0.5 / +0.4	+2.5 / −10.8	−29.2 / +22.4	+2.4 / −3.5
jet_jer_np6	−0.1 / +0.2	−3.2 / +6.5	−3.6 / −5.1	+0.3 / 0.1
jet_jer_np7	+0.0 / 0.2	+26.0 / −12.6	+5.4 / −12.8	−0.3 / −0.9
jet_jer_np8	+0.0 / 0.1	+13.2 / −0.1	+0.0 / −28.1	+0.0 / −1.9
jet_jes_bjes_response	+0.0 / −0.0	+0.0 / −0.0	+0.0 / −0.0	+0.0 / −0.0
jet_jes_effectivenp_1	+0.6 / −0.8	−1.4 / +3.2	+28.8 / −60.5	+1.9 / −3.2
jet_jes_effectivenp_2	+0.3 / −0.1	+1.2 / −2.3	+1.1 / −22.8	+0.3 / −0.6
jet_jes_effectivenp_3	−0.0 / +0.4	+0.6 / −0.4	−27.9 / +12.0	−0.9 / +0.3
jet_jes_effectivenp_4	+0.3 / −0.1	−1.1 / +0.4	+9.6 / −19.0	+2.6 / −0.1
jet_jes_effectivenp_5	+0.0 / −0.0	−0.1 / +1.0	+3.8 / −4.9	+3.6 / −0.7
jet_jes_effectivenp_6	−0.1 / +0.1	+0.1 / −0.4	+3.9 / −0.8	−2.4 / +1.1
jet_jes_effectivenp_7	+0.1 / −0.1	+0.2 / −0.3	+6.0 / −3.5	+1.0 / −1.0
jet_jes_effectivenp_8restterm	+0.2 / −0.0	+1.5 / −0.3	+2.8 / −11.2	+0.2 / −0.6
jet_jes_etaintercalibration_modelling	+0.1 / −0.5	−1.3 / +1.8	+18.7 / −48.4	+2.3 / −3.9
jet_jes_etaintercalibration_nonclosure	−0.5 / +0.4	+0.4 / −5.7	−51.0 / +36.0	−5.2 / +1.5
jet_jes_etaintercalibration_totalstat	+0.2 / −0.2	+0.4 / −0.7	+12.0 / −21.8	+0.7 / −0.5
jet_jes_flavor_composition	+0.7 / −1.0	−1.9 / +1.2	+17.0 / −11.8	+1.0 / −3.0
jet_jes_flavor_response	−1.2 / +1.2	+2.3 / −1.0	−66.7 / +50.1	−2.0 / +4.0
jet_jes_pileup_offsetmu	−0.3 / +0.2	+1.4 / −0.2	−18.5 / +3.1	−1.9 / +3.5
jet_jes_pileup_offsetnpv	+0.0 / −0.1	+2.4 / −2.5	+6.6 / −18.6	+1.4 / −0.5
jet_jes_pileup_ptterm	+0.6 / −0.5	−7.8 / +0.1	+37.5 / −54.4	+0.2 / +2.0
jet_jes_pileup_rhotopology	+0.8 / −1.1	+1.7 / −4.8	+71.5 / −90.8	+0.9 / −7.4
jet_jes_punchthrough_mc15	+0.0 / −0.0	+0.0 / −0.0	+0.7 / −0.1	+0.3 / −0.0
jet_jes_singleparticle_highpt	+0.0 / −0.0	+0.0 / −0.0	+0.0 / −0.0	+0.0 / −0.0
jet_jvteff	+0.3 / −0.3	+0.6 / −0.6	+19.4 / −19.4	+1.4 / −1.4
lumi	+3.1 / −3.0	+3.9 / −3.9	+163.6 / −163.5	+7.1 / −7.1
met_softtrk_resopara	+1.4 / −1.4	+0.0 / +0.0	+0.0 / −0.0	+0.0 / −0.0
met_softtrk_resoperp	+1.2 / −1.2	+0.0 / +0.0	+0.0 / −0.0	+0.0 / −0.0
met_softtrk_scale	+1.2 / −1.0	+0.0 / +0.0	+0.0 / 0.0	+0.0 / 0.0
pu_prw2015	+0.1 / −0.0	+2.2 / −6.4	−0.1 / +29.2	+3.9 / −3.6
pu_prw2016	+3.3 / −2.6	+2.7 / −7.9	−183.6 / +76.5	−17.9 / +7.9
QCD_scale_uncertainty	+0.0 / 0.0	+177.9 / −177.9	−177.9 / +177.9	+0.0 / 0.0
tau_eff_eleolr_trueelectron	+0.0 / −0.0	−0.3 / +0.3	+0.0 / −0.0	+1.2 / −1.1
tau_eff_eleolr_truehadtau	+2.7 / −2.7	−2.7 / +2.7	+137.5 / −135.6	+4.4 / −4.3
tau_eff_jetid_highpt	+0.1 / −0.1	−0.0 / +0.1	+2.5 / −2.4	+0.1 / −0.1
tau_eff_jetid_total	+11.7 / −11.0	−12.1 / +11.6	+623.4 / −588.3	+19.6 / −18.8
tau_eff_reco_highpt	+0.0 / −0.0	+0.0 / −0.0	+0.0 / −0.0	+0.0 / −0.0
tau_eff_reco_total	+7.1 / −6.8	−7.8 / +7.6	+401.7 / −386.9	+12.5 / −12.2
tau_tes_detector	−2.0 / +2.4	+0.1 / −1.5	−126.1 / +130.6	−4.0 / +2.3
tau_tes_insitu	+3.5 / −4.3	−7.5 / +12.8	+315.9 / −394.8	+19.3 / −9.3
tau_tes_model	+0.7 / −0.5	−2.0 / +2.4	+55.2 / −61.5	+4.6 / −0.0
tau_trigger_statdata2015	+0.4 / −0.5	−0.4 / +0.6	+16.1 / −21.0	+0.5 / −0.6
tau_trigger_statdata2016	+1.5 / −1.4	−1.5 / +1.5	+76.7 / −76.0	+2.5 / −2.5
tau_trigger_statmc2015	+0.2 / −0.2	−0.2 / +0.2	+6.5 / −8.0	+0.2 / −0.2
tau_trigger_statmc2016	+0.9 / −0.8	−0.9 / +0.9	+46.0 / −45.8	+1.5 / −1.5
tau_trigger_syst2015	+0.3 / −0.2	−0.4 / +0.5	+13.8 / −14.0	+0.4 / −0.4
tau_trigger_syst2016	+0.6 / −0.5	−0.5 / +0.6	+28.3 / −28.1	+0.9 / −0.9
theory_ztt_PDF	+0.0 / 0.0	−5.6 / +5.6	+394.1 / −394.0	+0.0 / 0.0
theory_ztt_lhe3weight_mur05_muf05_pdf261000	+0.0 / 0.0	−16.8 / −16.8	+700.4 / −700.4	+0.0 / 0.0
theory_ztt_lhe3weight_mur05_muf1_pdf261000	+0.0 / 0.0	−16.2 / +16.2	+667.0 / −667.0	+0.0 / 0.0
theory_ztt_lhe3weight_mur1_muf05_pdf261000	+0.0 / 0.0	−0.1 / +0.1	−2.2 / +2.2	+0.0 / 0.0
theory_ztt_lhe3weight_mur1_muf1_pdf261000	+0.0 / 0.0	−0.0 / +0.0	+0.0 / −0.0	+0.0 / 0.0
theory_ztt_lhe3weight_mur1_muf2_pdf261000	+0.0 / 0.0	−0.1 / +0.1	+6.8 / −6.8	+0.0 / 0.0
theory_ztt_lhe3weight_mur2_muf1_pdf261000	+0.0 / 0.0	+11.2 / −11.2	−513.0 / +513.0	+0.0 / 0.0
theory_ztt_lhe3weight_mur2_muf2_pdf261000	+0.0 / 0.0	+11.0 / −11.0	−490.1 / +490.1	+0.0 / 0.0
Z_scale_uncertainty	+0.0 / 0.0	−187.3 / +187.3	+187.3 / −187.3	+0.0 / 0.0

7.5 Fit procedure

The sensitivity to the *CP* mixing angle ϕ_τ is estimated by performing maximum likelihood fits of φ^*_{CP} in the separate signal regions simultaneously. Denoting the measured data by $\boldsymbol{x}$, a binned likelihood function $L(\boldsymbol{x};\mu,\boldsymbol{\theta})$ is constructed, where μ is the signal strength, and $\boldsymbol{\theta}$ represents further nuisance parameters. The signal strength is defined as the ratio of the measured signal cross section times branching ratio ($\sigma\times\mathscr{B}$), to the SM expectation. It is not constrained in the fit, hence no model dependence on $\sigma\times\mathscr{B}$ for mixed-*CP* states is introduced, only information about the shape of φ^*_{CP} is exploited. The likelihood function consists of the signal model for a given mixing hypothesis, and the background model, and is defined as the product of Poisson probability terms for each bin in the distribution of φ^*_{CP}.

For each mixing hypothesis considered, the corresponding TauSpinner weighted signal template is used, while the background model is kept fixed. The likelihood function is evaluated for each hypothesis, profiling the nuisance parameters to their best-fit values $\hat{\boldsymbol{\theta}}$. The best estimator for the mixing parameter, $\hat{\phi}_\tau$, is the signal hypothesis for which the log-likelihood is highest, i.e. $\log L(\boldsymbol{x},\mu,\hat{\theta}) = \log L_{\max}$. The 1σ confidence interval on ϕ_τ is defined by

$$\log L(\theta) \geq \log L_{\max} - \frac{1}{2}, \tag{7.2}$$

which can be rewritten using the difference between log-likelihood value of each hypothesis and the best-fit hypothesis,

$$\Delta \log L \equiv L(\boldsymbol{\theta}) - \log L_{\max} \geq \frac{1}{2}. \tag{7.3}$$

Since in practice the *negative* log-likelihood (NLL) is computed, the relation becomes

$$\Delta\text{NLL} = \log L_{\max} - L(\boldsymbol{\theta}) \leq \frac{1}{2}. \tag{7.4}$$

After computing the NLL value for each hypothesis, the curve for ΔNLL as function of ϕ_τ can be plotted by interpolating between the points. From this curve, one can read off $\hat{\phi}_\tau$ at the point where the curve has a minimum, and from the above equation, the 1σ confidence interval can be read off directly at the points where the curve crosses ΔNLL = 0.5.

7.6 Results

The expected sensitivity is estimated by running the fit to a set of pseudo-data, constructed to be equal to the expected φ^*_{CP} distribution of all backgrounds, plus a signal model corresponding to the SM hypothesis. In this *Asimov* dataset [92], all parameters, including event yields and all nuisance parameters to the fit, are set to their expected values, which allows for computing the median significance without generating a large number of Monte Carlo pseudo-experiments. The signal model is 'SM' both in terms of the φ^*_{CP} distribution, representing a pure scalar, and the production cross section, set equal to the SM expectation. The background contribution follows

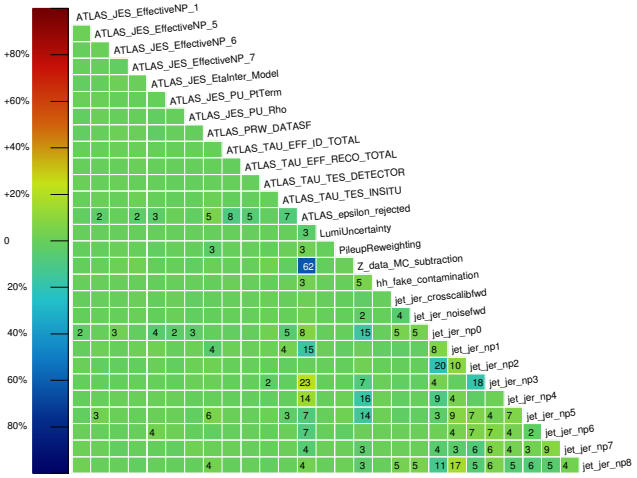

Figure 7.10: Matrix showing the correlation between the nuisance parameters included in the fit of the $\phi_\tau = 0$ hypothesis.

exactly the description in section 7.3, using same-sign data events in the Higgs mass window for QCD jets faking taus, and opposite-sign data events in the Z mass window for $Z \to \tau\tau$ background. The statistical power of the Asimov dataset is equal to that of the combined 2015 and 2016 data.

The full set of nuisance parameters are included in the fit, and their fitted values in the case of the *CP*-even hypothesis are shown in table A.1. For convenience, the values and their uncertainties are plotted in fig. 7.11. The correlation between the individual nuisance parameters is calculated and shown in fig. 7.10.

Fitted distributions for the CP-even hypothesis ($\phi_\tau = 0$) are shown in fig. 7.12 for the VBF category, in fig. 7.13 for the boosted high-p_T category, and in fig. 7.14 for the boosted low-p_T category.

The resulting ΔNLL curve is shown in fig. 7.15. As expected, the *CP*-even hypothesis ($\phi_\tau = 0$) is favoured, and increasing values of the mixing parameter show decreasing compatibility with the Asimov dataset. The statistical power of the 2015 and 2016 dataset is, however, not sufficient to set 1σ limits on ϕ_τ.

7.6.1 Luminosity extrapolation

To estimate the approximate integrated luminosity needed to set limits on the Higgs mixing angle, the result from the previous section is extrapolated to correspond to larger datasets. The templates are scaled to the luminosity of two future scenarios: First, the expected LHC dataset at the end of running with the current machine configuration, planned to happen around 2023, at which point the anticipated luminosity is $300\,\mathrm{fb}^{-1}$. Second, the expected dataset from ten years of running with the High-Luminosity LHC [93], which is planned to be approximately $3000\,\mathrm{fb}^{-1}$. The resulting ΔNLL curves are shown in fig. 7.16. A dataset of $300\,\mathrm{fb}^{-1}$ does still not

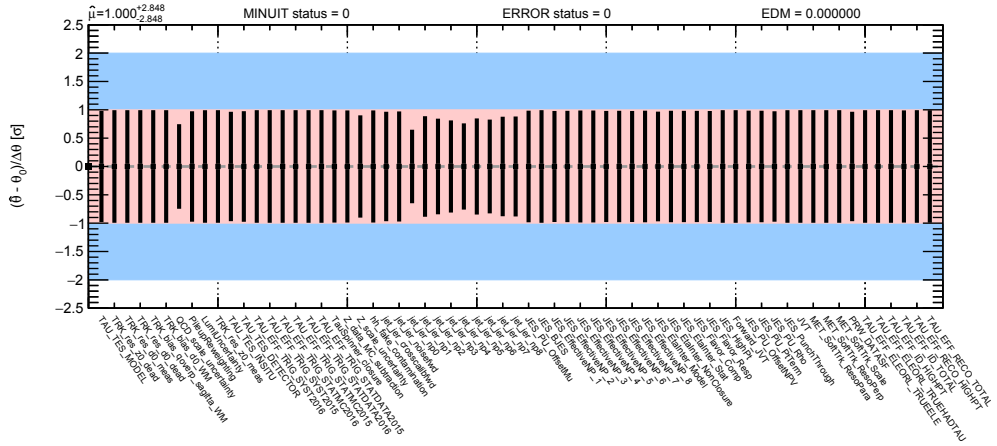

Figure 7.11: Pulls of the nuisance parameters. The values of each point are also listed in table A.1.

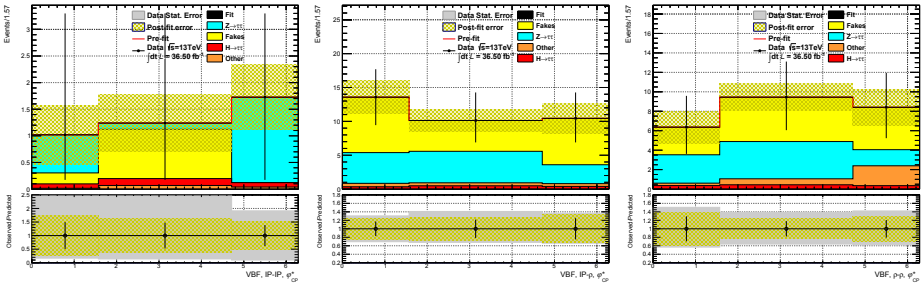

(a) IP-IP, VBF (b) IP-ρ, VBF (c) ρ-ρ, VBF

Figure 7.12: Postfit φ^*_{CP} distributions in the VBF category. Data points correspond to the Asimov dataset. The red histogram represents signal, light blue represents $Z \to \tau\tau$ decays, and yellow represents the fake tau background. The shaded region illustrates the post-fit uncertainty.

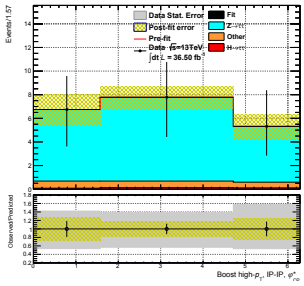

(a) IP-IP, boost high-p_{T}

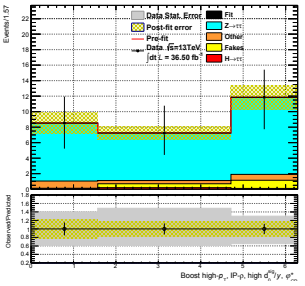

(b) IP-ρ, boost high-p_{T}, high d_0^{sig}/y

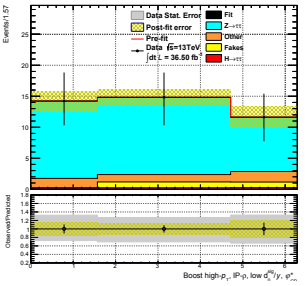

(c) IP-ρ, boost high-p_{T}, low d_0^{sig}/y

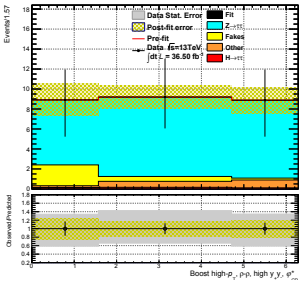

(d) ρ-ρ, boost high-p_{T} high y_+y_-

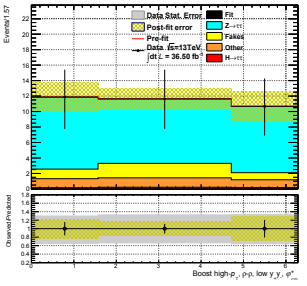

(e) ρ-ρ, boost high-p_{T}, low y_+y_-

Figure 7.13: Postfit φ^*_{CP} distributions in the boosted high-p_{T} category.

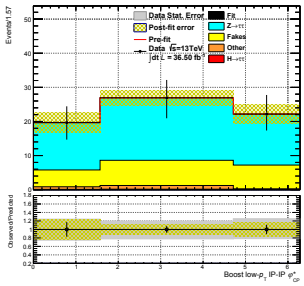

(a) IP-IP, boost low-pt

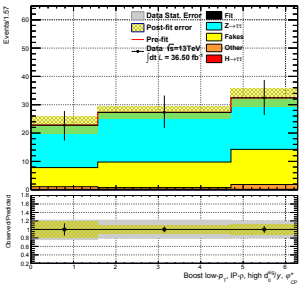

(b) IP-ρ, boost low-p_{T}, high d_0^{sig}/y

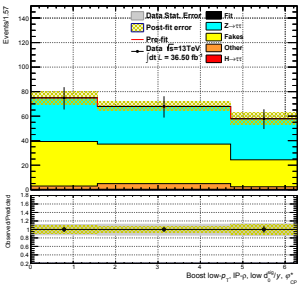

(c) IP-ρ, boost low-p_{T}, low d_0^{sig}/y

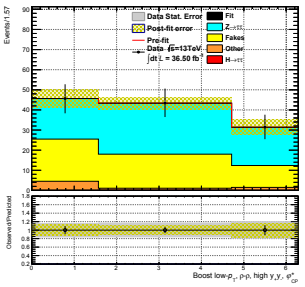

(d) ρ-ρ, boost low-p_{T}, high y_+y_-

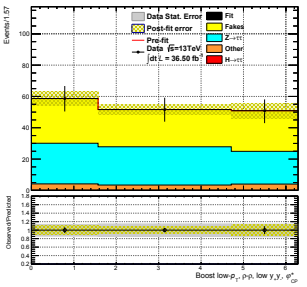

(e) ρ-ρ, boost low-p_{T}, low y_+y_-

Figure 7.14: Postfit φ^*_{CP} distributions in the boosted low-p_{T} category.

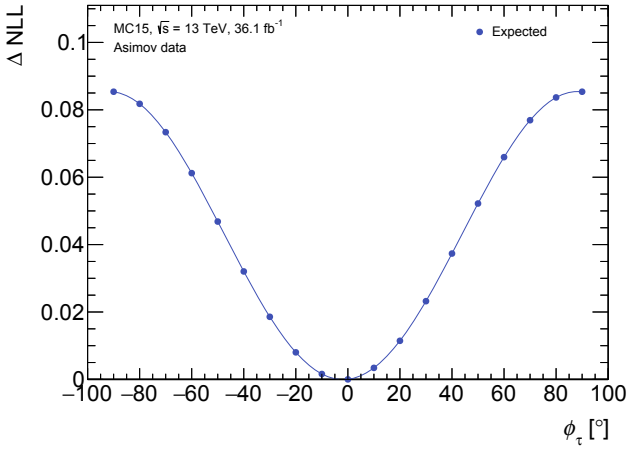

Figure 7.15: Difference in fitted negative log-likelihood (NLL) values between the best-fit ϕ_τ hypothesis to the Asimov dataset, and the fit to alternative hypotheses. Each data point represents the ΔNLL value for a given hypothesis. The line is a cubic interpolation to the points, and is only meant to guide the eye. The Asimov data used in the fits correspond to an integrated luminosity of 36.1 fb^{-1}.

exclude the *CP*-odd hypothesis, while the 3000 fb^{-1} dataset should allow for setting limits of $-60° < \phi_\tau < 60°$ at 1σ confidence level.

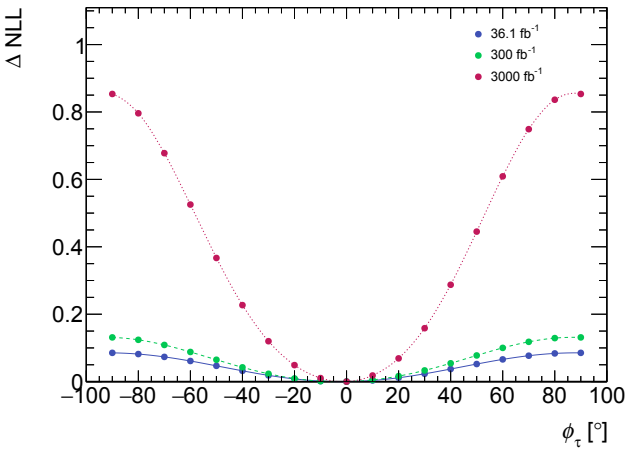

Figure 7.16: ΔNLL curves for 36.1 fb^{-1} (blue points), equal to the combined 2015 and 2016 dataset; 300 fb^{-1} (green points), equal to the expected dataset provided by the LHC around 2023; and 3000 fb^{-1} (red points) equal to the expected dataset provided by the High-Luminosity LHC, after running for about ten years.

Chapter 8

Multivariate study

Since the approach using φ^*_{CP}, shown in the previous chapter, exhibits too low sensitivity to provide a measurement with the current available data, a study has been conducted to investigate the potential gain of using a multivariate approach. Initially motivated by the fact that the IP-IP method can be applied to all decay types, and that choosing one applicable φ^*_{CP} reconstruction method over another might imply loss of information, the approach is extended to include all basic observables in the ditau decay system. A neural network is employed, chosen on basis of their capability to learn correlations across input observables, which is key to this task. The network is used to regress the Higgs mixing angle for each event, and then the network predictions are used as input to a maximum likelihood fit, similar to the procedure described in section 7.5. The following sections explain the approach in detail. For this study only $\tau\tau \to \rho(\pi\pi^0)\rho(\pi\pi^0)$ decays are considered, since it is, compared to $\tau\tau \to \pi\rho$ and $\tau\tau \to \pi\pi$, the most complicated decay and therefore more likely to benefit from a multivariate analysis; in addition, having the highest branching ratio, this decay offers the highest statistics in terms of training events. All observables, the data and MC samples, and the selection requirements used in the following, are identical to the previous chapter, unless otherwise stated.

8.1 Input observables

The event kinematics provided as input to the neural network are a combination of fundamental and derived observables. Studies on neural networks [94, 95] show that multi-layer (*deep*) networks, unlike for instance decision trees, perform very well on low-level observables alone, and adding high-level observables may add only a small improvement on top. Still, to ensure the best possible results, all relevant spin-sensitive observables are included. To conform with machine learning jargon, observables are hereafter called *features*.

The low-level feature set comprises the four-momenta of all visible tau decay products, boosted back to the ditau rest frame. In order to express the vectors in a reference frame common to all events, so that the spin correlations are not washed out by an arbitrary choice of basis, the positive z direction is chosen to lie along the direction of the negative tau. The system is rotated around the z axis so that the π^- has zero x component. Since the $\pi^\pm$ and π^0 are the only two particles constituting the tau decay system, their x and y components are opposite of each other, and the

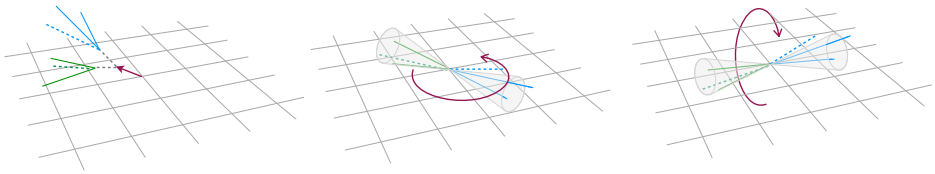

Figure 8.1: Illustration of the transformation of the coordiante system. First, all vectors are boosted back to the ditau restframe; second, the system is rotated so that the τ^- points in the postitive z direction; lastly, the system is rotated around the z axis so that the π^- has zero x component.

original 16 four-momentum components can this way be reduced to 11 independent variables. The rotation is illustrated in fig. 8.1.

The set of high-level features include y_-, y_+ and the product y_-y_+, impact parameter vectors of the charged pions, boosted and rotated the same way as for the four-momentum vectors, and φ^*_{CP} computed with all reconstruction methods: IP-IP, IP-ρ and ρ-ρ. Before being input to the network, all features are scaled so that each distribution in the training data has unit variance, and zero mean.

8.2 Assigning mixing parameter values to training data

In order for the network to learn the correlation between the event kinematics and the Higgs mixing parameter, each training event must be provided with the true mixing value used in simulation. Ideally, to cover the full spectrum of possible mixing values with equal precision, one would have signal samples generated with continuous values of the mixing parameter. A typical approach would be to introduce some level of discretisation, simulating events at certain intervals of the mixing parameter, and let the network interpolate between these intervals. With an unpolarised signal sample, however, a continuous range of mixing parameters can in practice be realised by using `TauSpinner` weights. The unpolarised sample has by definition no value of the mixing parameter, hence no target for the network to learn; this is introduced in its entirety by the following post-simulation analysis.

As discussed in section 6.3, for an event with unpolarised taus, `TauSpinner` calculates a weight $w \in (0, 2)$ representing how compatible the event is with a given mixing parameter hypothesis. For all events, this weight is computed for 18 different mixing hypotheses in equally spaced intervals of 10° in ϕ_τ. The distribution of weights as function of mixing hypothesis, for an example event, is shown in fig. 8.2. Due to the probabilistic nature of the spin correlation, the distribution of weights is broad, and because of the structure of the decay matrix element it follows a sinusoidal shape. A least-squares fit is performed to obtain the parameters of the sine curve. This curve is now interpreted as an unnormalised probability density function for the mixing parameter, from which a parameter value can be sampled, using a simple acceptance-rejection method. The solid line in fig. 8.2 shows the sampled value for this particular event. This value is now taken to be the inherent mixing parameter for the event, and following this procedure, all events are assigned a non-discrete

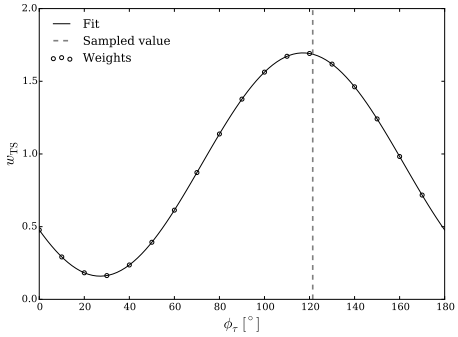

Figure 8.2: Distribution of `TauSpinner` weights for a single example event. The calculated `TauSpinner` weights are deterministic, while the mixing parameter value is randomly sampled.

mixing value, which for the sample as a whole will be uniformly distributed over the allowed ϕ_τ range.

8.3 Network structure and loss function

The network is a fully connected feed-forward network implemented in Keras [96] using TensorFlow [97] as backend. It consists of an input layer with 300 nodes, followed by four equally wide hidden layers with 300 nodes each, using rectified linear (ReLU) [98] activation functions. The single output node has a linear activation function. Batch normalisation [99] is used to improve the speed and stability of training, and the weights are regularised using a combination of L2 regularisation, which penalises the squared sum of node weights, and dropout [100], which randomly removes a percentage of nodes during training, reducing the amount of co-adaptations between nodes and thereby adding robustness. These techniques are all largely standard in machine learning applications. The node weights are optimised using the Adam [101] algorithm, a variant of stochastic gradient descent, including momentum and adaptive learning rate. The networks are trained for 200 epochs using a batch size of 256.

The loss function quantifies the discrepancy between the network prediction and the true target value, and is the value being minimised during training. Typical loss values for a regression problem are mean squared error, $\mathrm{MSE} = 1/n \sum_{i=1}^{n} (y_i^{\mathrm{true}} - \hat{y}_{\mathrm{i}})^2$, or mean absolute error, $\mathrm{MAE} = 1/n \sum_{i=1}^{n} |y_i^{\mathrm{true}} - \hat{y}_{\mathrm{i}}|$, where $\hat{y}$ is the network output, and y^{true} the target value. A disadvantage of MSE loss is that it is heavily affected by values located far from $\hat{y}$, meaning it is not robust against outliers, measurements which are far from the peak of their distribution. For this particular analysis, *outlier* is hardly the right term — looking at the most sensitive observable, φ_{CP}^* (fig. 6.3), all points on the allowed range have reasonably high probability, irregardless of mixing value. In other words, the network should not penalise the pseudoscalar hypothesis too heavily, for an event with $\varphi_{CP}^* = \pi$. On the other hand, although MAE is more robust, is is also less efficient [102], and the non-differentiability at 0 can in some

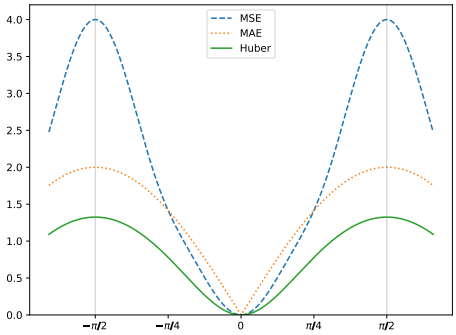

Figure 8.3: Comparison of periodic loss functions. Values greater than $\pi/2$ and smaller than $-\pi/2$ are not possible, but included here to illustrate the periodicity.

cases pose problems.

An elegant way to combine the two is the Huber loss function [103], defined as

$$L(x) = \begin{cases} \frac{1}{2}x^2, & \text{if } |x| \leq \delta, \\ \delta(|x| - \frac{1}{2}\delta) & \text{otherwise,} \end{cases} \tag{8.1}$$

where $x = y_i^{\text{true}} - \hat{y}_\text{i}$ is used, for simplicity. This function behaves linearly for large x (greater than the parameter δ), but is quadratic for small x. The definition in eq. (8.1) is shown primarily because it is somewhat easy to visualise; in practice a continuously differentiable approximation is used, defined as

$$L(x) = \log(\frac{1}{2}\exp(x) - \frac{1}{2}\exp(-x)). \tag{8.2}$$

Because the target variable ϕ_τ is periodic, this periodicity must be incorporated into the loss function. Otherwise, the distance between for instance $\phi_\tau = 89°$ and $\phi_\tau = -89°$ would be computed to 178° and result in a high loss value, while the true distance is in fact 2°, which should yield a low loss. This is solved by redefining the target variable from a scalar to a two-component vector, where one component equals $\sin(2\phi_\tau)$, and the other $\cos(2\phi_\tau)$. The factor 2 accounts for ϕ_τ being periodic on an interval of width π, rather than 2π. The norm of this vector is always less than π, and gives the desired behaviour at the boundaries of ϕ_τ. An illustration of the resulting loss function, including a comparison to periodic MSE and MAE, is shown in fig. 8.3. Upon evaluation of test data, the two-component vector output from the neural network is converted back into the mixing parameter.

8.4 Sensitivity comparison

To compare the neural network approach with the one-dimensional φ^*_{CP} method, a similar fit as explained in section 7.5 is performed, but with the neural network output as the discriminating variable. Like for ϕ_τ, the network output ranges from $-\pi/2$ to $\pi/2$ and represents the network's belief in the underlying mixing parameter of each

individual event. Half of the signal sample is used to train the network, while the other half is used to create templates to be used in the fit. The different templates are constructed from the unpolarised signal sample the same way as for φ^*_{CP}; TauSpinner weights are used to re-weight the histogram to each different mixing hypothesis being studied.

The technique of applying a template fit to the output for a machine learning algorithm is known to improve sensitivity in classifiers, compared to simply cutting at an optimised value [104]. The procedure was for instance used in the ATLAS $H \to \tau\tau$ search in Run 1 data [70]. Also in the regression case, utilising the shape of the network output in a fit is sensitivity-wise preferable over simply averaging the output values. At the same time, it allows for a direct one-to-one comparison with the φ^*_{CP} approach, as the only difference is the observable being fitted.

8.4.1 Generator-level analysis

As in initial test, the comparison of the methods is performed on generator level samples, i.e. without detector simulation. No selection requirements are applied in this case, while a more realistic comparison using the full set of background samples is covered in the next section. To investigate how the performance is affected by which features are included, different networks are trained on the following feature sets:

- φ^*_{CP} only: This network is trained on the single feature φ^*_{CP}, and is expected to be very similar in performance as fitting to φ^*_{CP} directly, since the information is the same. This network has a smaller architecture of ten nodes in the input layer, followed by a single hidden layer, also with ten nodes.

- Basic observables: This network is trained on the four-momenta of the tau decay products, and the missing transverse momentum vector.

- All observables: This network is trained on the basic observables, but also on the track impact parameter vectors, the $y_{+/-}$ values, and all φ^*_{CP} reconstruction methods.

In this simplified comparison, the dataset which will be tested, is generic and composed of 100 *CP*-even signal events, and 300 background events. Since the aim in this case is to study how effectively the network can identify the mixing angle in signal events, the background template is taken to be uniform distribution normalised to 300 events; no background events are actually evaluated by the network. The expectation that the network response on uncorrelated tau candidate pairs (from fake taus) and tau pairs from a spin-1 decay (Z/γ) is uniform, is based on the fact that the φ^*_{CP} distribution for these backgrounds is also uniform. This approximation is lifted in the next section.

Part of the reason for performing a generator-level study is the fact that the number of available training events is significantly higher, as basic quality requirements applied during early stages of sample processing, in the physics groups *derivations*, are avoided. These requirements include $p_{\mathrm{T}}(\tau) > 18\,\mathrm{GeV}$ and $\Delta R_{\tau\tau} < 0.6$. Furthermore, the impact of the detector simulation is removed. The signal sample statistics

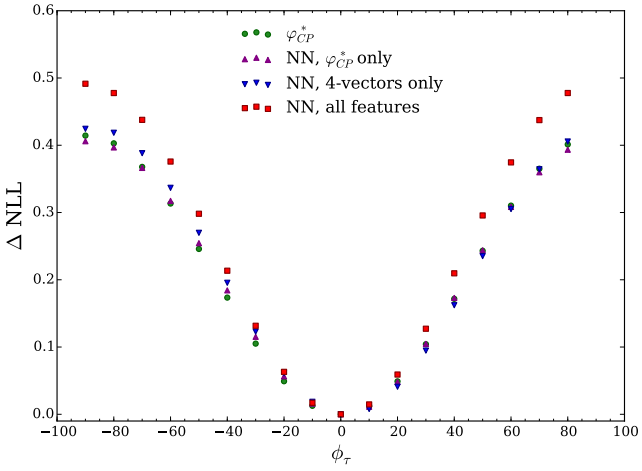

Figure 8.4: Generator-level comparison of neural networks to the φ^*_{CP} method. The φ^*_{CP} approach is shown in green dots. The simple network trained on the distribution of φ^*_{CP} alone, plotted with purple triangles, shows nearly identical performance. Blue triangles show the network trained on the four-momentum of the decay products and $E_{\mathrm{T}}^{\mathrm{miss}}$, while red squares show the network trained on all available features.

on generator level is 326 276 events, of which 50% is used for training the network, and 50% is used to validate the training. After each training epoch, i.e. after each full pass over all training events, the network is evaluated on the unseen validation set in order to prevent overfitting.

The result of the comparison can be seen in fig. 8.4. The baseline for the comparison, the φ^*_{CP} fit, is shown in green points. The network trained on φ^*_{CP} alone shows similar performance, as expected, while training on the basic observable set yields only marginal improvement. Although not initially expected, using the full feature set performs noticeably better.

8.4.2 Reconstruction level comparison

Having established the potential improvement of using a neural network approach, the method is applied to full detector simulation samples, using the complete set of expected backgrounds. To make the following result comparable to the discussion in the previous chapter, the same event selection and categorisation defined in table 7.2 is used. The analysis is still restricted to ρ-ρ decays, however, and systematic uncertainties are not included. After preselection requirements, the signal sample contains 12 920 events in total, again to be split 50–50 in a training and a validation set. The very limited number of events available for training, in addition to the equally limited number of events to use for template creation, poses a major problem to the procedure. In a sparsely populated feature space there is high risk of overfitting, and necessarily difficult to model the true underlying probability density functions of the features. For this reason, a single network is trained on data in the preselection re-

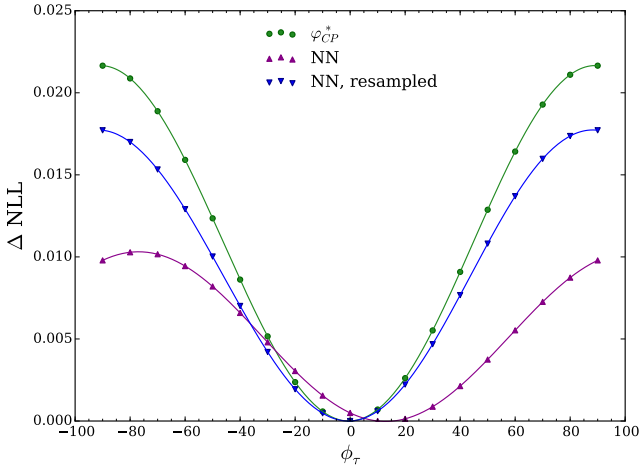

Figure 8.5: ΔNLL curves for the φ^*_{CP} approach (green points), a network trained on without the resampling technique (purple points), and a network trained with the resampling technique (blue points). Since these results are obtained using only ρ-ρ decays, the ΔNLL values are not directly comparable to fig. 7.15.

gion, rather than training separately on the final VBF and boosted signal regions. A method to mitigate this issue is discussed in the next section; results without this technique, are shown for comparison.

Similar to section 7.6, the expected sensitivity is estimated from fits to an Asimov dataset corresponding to *CP*-even signal and backgrounds normalised to the Standard Model expectation. The contribution from $Z \to \tau\tau$ is taken from Monte Carlo, while the fake tau contribution is taken from data. The background normalisation is fixed from a fit to the $\Delta\eta_{\tau\tau}$ distribution as described in section 7.3. All events, including backgrounds, are evaluated by the network. As nothing is different from the ordinary φ^*_{CP} fit at this point, the event yields and normalisations are identical. The resulting ΔNLL curve is shown in fig. 8.5, where the φ^*_{CP} method is plotted with green points, and the neural network approach with purple points. It is quite apparent that the network approach is underperforming, as it not only exhibiting lower amplitude than the result using the φ^*_{CP} observable, but it is also horizontally shifted and fails to identify the true ϕ_τ value of the dataset.

Case resampling

To overcome the performance limitations caused by the insufficient number of training events, a method for resampling events is explored. Various techniques for creating synthetic data from a sample exists, for instance by considering two data points which lie near each other in feature space, and randomly create a new data point somewhere on the vector connecting them [105]. For this particular analysis, however, the inherent randomness in the way the target value of an event is assigned, is put to use. Since the mixing parameter value is drawn randomly from the distribution of `TauSpinner` weights, repeating the procedure on the same event yields a

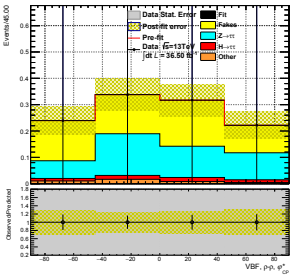

(a) ρ-ρ, VBF category

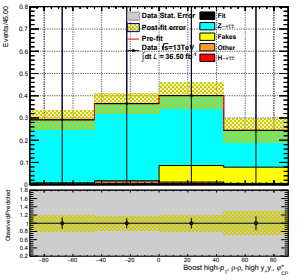

(b) ρ-ρ, boost high-p_{T}, high $|y_+ y_-|$

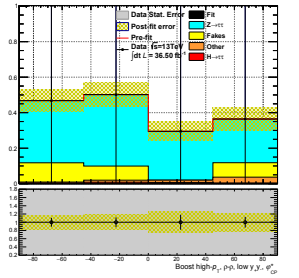

(c) ρ-ρ, boost high-p_{T}, low $|y_+ y_-|$

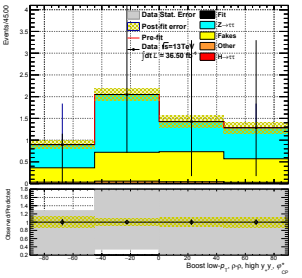

(d) ρ-ρ, boost low-p_{T}, high $|y_+ y_-|$

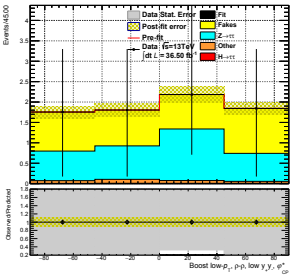

(e) ρ-ρ, boost low-p_{T}, low $|y_+ y_-|$

non-identical value. A set of resampled training data is created by duplicating the initial data points ten times, but each time drawing a new mixing parameter value for each event. A new network is trained on these data, and plotted in blue in fig. 8.5. Post-fit histograms for each analysis region, are shown in section 8.4.2. Using the resampled data, the ΔNLL curve for the network recovers the expected shape, but the performance remains lower than the baseline φ^*_{CP} result. Several reasons can explain this. First of all, the training data, and likewise the data used to create the templates for the fit, are very limited, making it difficult both for the network to learn the probability density distributions of the input features, and to estimate the distribution of the network output for different mixing hypotheses. Second, also due to the limited statistics, the network was trained on data in a less restricted region that in the signal regions where it is tested, and does therefore not see the same feature distributions as trained on. Since generating Monte Carlo samples with full detector simulation is highly CPU intensive, the problem cannot be quickly remedied by creating larger samples, which makes resampling techniques attractive. To conclude, significant improvements are required for the neural network approach to be stable enough to compete with the existing method.

Chapter 9

Conclusion

So far over the course of Run 2, the ATLAS experiment has seen several highlights, one of them being the successful inclusion of a new pixel layer. The readout and reconstruction software has been updated to accommodate the new sensors and the new features provided by the upgraded front-end chips, and has been thoroughly tested over the several dedicated commissioning periods leading up to the start of 13 TeV proton collisions in 2015. Over the following years of datataking, the radiation damage to the pixel layers has been studied by analysing the charge collection as function of applied bias voltage. The operating voltages of the different layers have been continually adjusted to reflect the rising depletion voltage, ensuring efficient operation of the detector.

An improved tau reconstruction algorithm allowed for studying the spin correlation between tau pairs, which gives insight to the *CP* property of the Higgs boson. A Monte Carlo study, hopefully to be followed by a public result in the near future, shows that the method is, however, not sensitive enough to provide a satisfactory limit on the possible mixing of Higgs *CP* states. A potential improvement is possible through the use of multivariate techniques; a neural network approach has been assessed, but is limited by the availability of simulated training events.

The performance of the LHC has been constantly increasing over Run 2, with 2017 being an impressive year where the highest instantaneous luminosity reached twice the machine's design value. Run 2 will continue out 2018, when a second long shutdown period begins. An upgraded High-Luminosity LHC is planned to start operation in 2025, increasing the instantaneous luminosity by an order of magnitude. This improvement allows for probing extremely rare processes, suggesting an interesting time lies ahead.

Appendix A

Auxiliary material

Table A.1: Fitted values of the nuisance parameters included in the fit, discussed in section 7.6.

ATLAS_epsilon_rejected	1	-2.84768	2.84768
Forward_JVT	0	0.99335	-0.99335
JES_BJES 0	0.99335	-0.99335	
JES_EffectiveNP_1	0	0.979699	-0.979699
JES_EffectiveNP_2	0	0.982163	-0.982163
JES_EffectiveNP_3	0	0.987755	-0.987755
JES_EffectiveNP_4	0	0.987319	-0.987319
JES_EffectiveNP_5	0	0.980134	-0.980134
JES_EffectiveNP_6	0	0.982834	-0.982834
JES_EffectiveNP_7	0	0.979729	-0.979729
JES_EffectiveNP_8	0	0.984644	-0.984644
JES_EtaInter_Model	0	0.967735	-0.967735
JES_EtaInter_NonClosure	0	0.983185	-0.983185
JES_EtaInter_Stat	0	0.982099	-0.982099
JES_Flavor_Comp	0	0.981288	-0.981288
JES_Flavor_Resp	0	0.97894	-0.97894
JES_HighPt	0	0.99335	-0.99335
JES_PU_OffsetMu	0	0.984789	-0.984789
JES_PU_OffsetNPV	0	0.985458	-0.985458
JES_PU_PtTerm	0	0.983726	-0.983726
JES_PU_Rho	0	0.97422	-0.97422
JES_PunchThrough	0	0.993161	-0.993161
JVT	0	0.99335	-0.99335
MET_SoftTrk_ResoPara	0	0.99333	-0.99333
MET_SoftTrk_ResoPerp	0	0.993307	-0.993307
MET_SoftTrk_Scale	0	0.993361	-0.993361
PRW_DATASF	0	0.965369	-0.965369
TAU_EFF_ELEORL_TRUEELE	0	0.992908	-0.992908
TAU_EFF_ELEORL_TRUEHADTAU	0	0.993127	-0.993127
TAU_EFF_ID_HIGHPT	0	0.993338	-0.993338
TAU_EFF_ID_TOTAL	0	0.989575	-0.989575
TAU_EFF_RECO_HIGHPT	0	0.99335	-0.99335
TAU_EFF_RECO_TOTAL	0	0.991933	-0.991933
TAU_EFF_TRIG_STATDATA2015	0	0.993321	-0.993321
TAU_EFF_TRIG_STATDATA2016	0	0.993251	-0.993251
TAU_EFF_TRIG_STATMC2015	0	0.993344	-0.993344
TAU_EFF_TRIG_STATMC2016	0	0.993309	-0.993309
TAU_EFF_TRIG_SYST2015	0	0.993354	-0.993354
TAU_EFF_TRIG_SYST2016	0	0.993331	-0.993331
TAU_TES_DETECTOR	0	0.975545	-0.975545
TAU_TES_INSITU	0	0.964914	-0.964914
TAU_TES_MODEL	0	0.980079	-0.980079
LumiUncertainty	0	0.992751	-0.992751
PileupReweighting	0	0.974124	-0.974124
QCD_scale_uncertainty	0	0.746212	-0.746212
TRK_bias_d0_WM	0	0.993346	-0.993346
TRK_bias_qoverp_sagitta_WM	0	0.99335	-0.99335
TRK_res_d0_dead	0	0.99335	-0.99335
TRK_res_d0_meas	0	0.993343	-0.993343
TRK_res_z0_dead	0	0.99335	-0.99335
TRK_res_z0_meas	0	0.993312	-0.993312
TauSpinner_closure	0	0.989435	-0.989435
Z_data_MC_subtraction	0	0.989069	-0.989069
Z_scale_uncertainty	0	0.902191	-0.902191
hh_fake_contamination	0	0.989089	-0.989089
jet_jer_crosscalibfwd	0	0.965636	-0.965636
jet_jer_noisefwd	0	0.971205	-0.971205
jet_jer_np0	0	0.648535	-0.648535
jet_jer_np1	0	0.887004	-0.887004
jet_jer_np2	0	0.843696	-0.843696
jet_jer_np3	0	0.812716	-0.812716
jet_jer_np4	0	0.760693	-0.760693
jet_jer_np5	0	0.847905	-0.847905
jet_jer_np6	0	0.827346	-0.827346
jet_jer_np7	0	0.877896	-0.877896
jet_jer_np8	0	0.881911	-0.881911

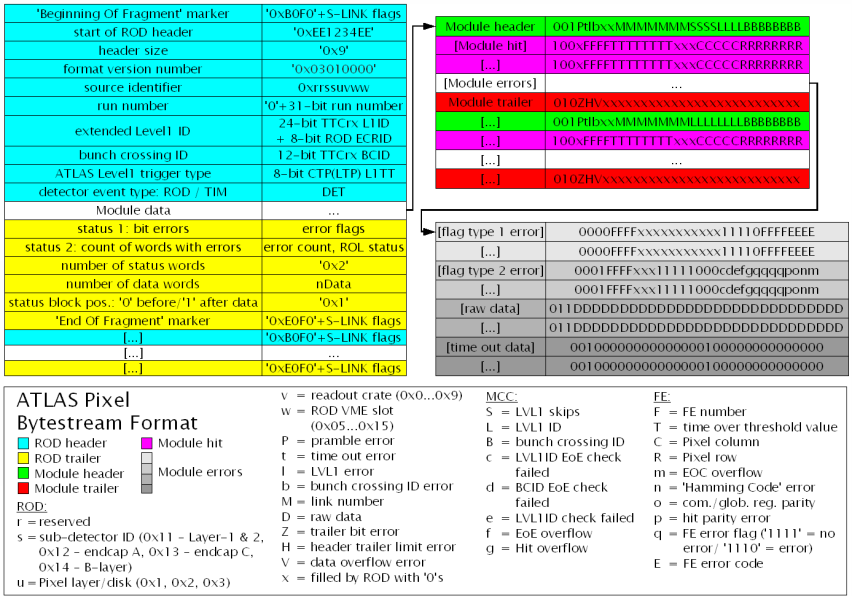

Figure A.1: The MCC bytestream format of the original pixel layers.

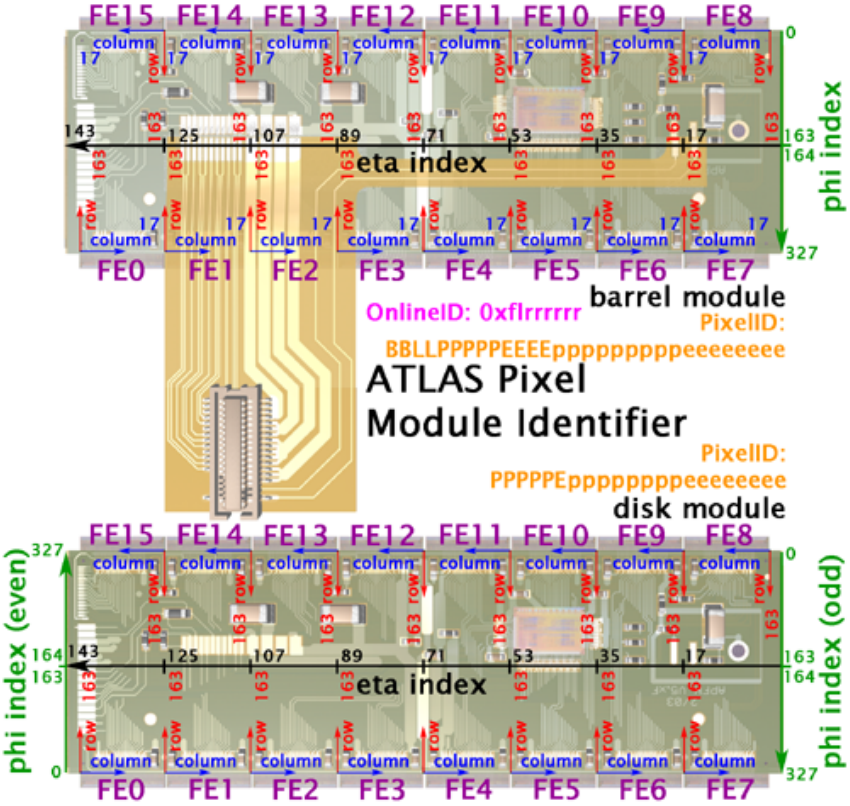

Figure A.2: Sketch of the pixel modules, showing the front-end numbers and the directions of the eta and phi indices.

Glossary

BCID Bunch Crossing Identifier.

BDT Boosted Decision Tree.

CP Charge-Parity.

CSC Cathode Strip Chambers.

DBM Diamond Beam Monitor.

EM Electromagnetic.

FE Front-End.

***gg*F** Gluon-gluon Fusion.

HLT High-Level Trigger.

IBL Insertable *b*-Layer.

IOV Interval Of Validity.

IP Impact Parameter.

JER Jet Energy Resolution.

JES Jet Energy Scale.

JVT Jet Vertex Tagging.

L1 Level 1 Trigger.

L1ID Level 1 Accept Identifier.

MC Monte Carlo.

MCC Module Control Chip.

MDT Monitored Drift Tubes.

MMC Missing Mass Calculator.

NIEL Non-Ionising Energy Loss.

NLL Negative Log-Likelihood.

OS Opposite-Sign.

PDF Parton Density Function.

PDG Particle Data Group.

PMG Physics Modelling Group.

RDO Raw Data Object.

ROB Read-Out Buffer.

ROD Read-Out Driver.

ROS Read-Out Subsystem.

SCT SemiConductor Tracker.

SM Standard Model.

SS Same-Sign.

TES Tau Energy Scale.

ToT Time over Threshold.

TRT Transition Radiation Tracker.

VBF Vector Boson Fusion.

Bibliography

[1] F. Mandl and G. G. Shaw, *Quantum field theory; 2nd ed.* Wiley, New York, NY, 2010. https://cds.cern.ch/record/1236742.

[2] V. Barger and R. Phillips, *COLLIDER PHYSICS; updated edition*. Addison-Wesley, Redwood City, USA, 1996.

[3] Particle Data Group Collaboration, C. Patrignani et al., *Review of Particle Physics*, Chin. Phys. **C40** (2016) 100001.

[4] C. Anastasiou, C. Duhr, F. Dulat, E. Furlan, T. Gehrmann, F. Herzog, A. Lazopoulos, and B. Mistlberger, *High precision determination of the gluon fusion Higgs boson cross-section at the LHC*, JHEP **05** (2016) 058, arXiv:1602.00695 [hep-ph].

[5] CMS Collaboration, V. Khachatryan et al., *Constraints on the spin-parity and anomalous HVV couplings of the Higgs boson in proton collisions at 7 and 8 TeV*, Phys. Rev. **D92** (2015) 012004, arXiv:1411.3441 [hep-ex].

[6] ATLAS Collaboration, G. Aad et al., *Study of the spin and parity of the Higgs boson in diboson decays with the ATLAS detector*, Eur. Phys. J. **C75** (2015) 476, arXiv:1506.05669 [hep-ex], [Erratum: Eur. Phys. J.C76,no.3,152(2016)].

[7] P. Artoisenet et al., *A framework for Higgs characterisation*, JHEP **11** (2013) 043, arXiv:1306.6464 [hep-ph].

[8] ATLAS Collaboration, M. Aaboud et al., *Measurement of the Higgs boson coupling properties in the $H \to ZZ^* \to 4\ell$ decay channel at $\sqrt{s}$ = 13 TeV with the ATLAS detector*, arXiv:1712.02304 [hep-ex].

[9] CMS Collaboration, A. M. Sirunyan et al., *Constraints on anomalous Higgs boson couplings using production and decay information in the four-lepton final state*, Phys. Lett. **B775** (2017) 1–24, arXiv:1707.00541 [hep-ex].

[10] J. Pequenao, *Computer generated image of the whole ATLAS detector*, Mar, 2008.

[11] I. Perić, L. Blanquart, G. Comes, P. Denes, K. Einsweiler, P. Fischer, E. Mandelli, and G. Meddeler, *The FEI3 readout chip for the ATLAS pixel detector*,.

[12] ATLAS Collaboration, G. Darbo, *Experience on 3D Silicon Sensors for ATLAS IBL*, JINST **10** (2015) C05001, arXiv:1411.6937 [physics.ins-det].

[13] *Track Reconstruction Performance of the ATLAS Inner Detector at* $\sqrt{s}$ = 13 *TeV*, Tech. Rep. ATL-PHYS-PUB-2015-018, CERN, Geneva, Jul, 2015. http://cds.cern.ch/record/2037683.

[14] M. zur Nedden, *The LHC Run 2 ATLAS trigger system: design, performance and plans*, Journal of Instrumentation **12** (2017) C03024, http://stacks.iop.org/1748-0221/12/i=03/a=C03024.

[15] ATLAS Collaboration, M. Aaboud et al., *Performance of the ATLAS Trigger System in 2015*, Eur. Phys. J. **C77** (2017) 317, arXiv:1611.09661 [hep-ex].

[16] ATLAS Collaboration, M. Aaboud et al., *Performance of the ATLAS Track Reconstruction Algorithms in Dense Environments in LHC Run 2*, Eur. Phys. J. **C77** (2017) 673, arXiv:1704.07983 [hep-ex].

[17] *Early Inner Detector Tracking Performance in the 2015 data at* $\sqrt{s}$ *= 13 TeV*, Tech. Rep. ATL-PHYS-PUB-2015-051, CERN, Geneva, Dec, 2015. https://cds.cern.ch/record/2110140.

[18] ATLAS Collaboration, *Luminosity public results Run 2*, https://twiki.cern.ch/twiki/bin/view/AtlasPublic/LuminosityPublicResultsRun2. [Online; accessed October 31, 2017].

[19] M. Cacciari, G. P. Salam, and G. Soyez, *The Anti-k(t) jet clustering algorithm*, JHEP **04** (2008) 063, arXiv:0802.1189 [hep-ph].

[20] ATLAS Collaboration, M. Aaboud et al., *Jet energy scale measurements and their systematic uncertainties in proton-proton collisions at* $\sqrt{s}$ = 13 *TeV with the ATLAS detector*, Phys. Rev. **D96** (2017) 072002, arXiv:1703.09665 [hep-ex].

[21] *Pile-up subtraction and suppression for jets in ATLAS*, Tech. Rep. ATLAS-CONF-2013-083, CERN, Geneva, Aug, 2013. https://cds.cern.ch/record/1570994.

[22] *Forward Jet Vertex Tagging: A new technique for the identification and rejection of forward pileup jets*, Tech. Rep. ATL-PHYS-PUB-2015-034, CERN, Geneva, Aug, 2015. https://cds.cern.ch/record/2042098.

[23] *Performance of missing transverse momentum reconstruction for the ATLAS detector in the first proton-proton collisions at at* $\sqrt{s}$*= 13 TeV*, Tech. Rep. ATL-PHYS-PUB-2015-027, CERN, Geneva, Jul, 2015. https://cds.cern.ch/record/2037904.

[24] ATLAS Collaboration, G. Aad et al., *Identification and energy calibration of hadronically decaying tau leptons with the ATLAS experiment in pp collisions at* $\sqrt{s}$*=8 TeV*, Eur. Phys. J. **C75** (2015) 303, arXiv:1412.7086 [hep-ex].

[25] *Reconstruction, Energy Calibration, and Identification of Hadronically Decaying Tau Leptons in the ATLAS Experiment for Run-2 of the LHC*, Tech. Rep. ATL-PHYS-PUB-2015-045, CERN, Geneva, Nov, 2015. https://cds.cern.ch/record/2064383.

[26] ATLAS Collaboration, G. Aad et al., *Reconstruction of hadronic decay products of tau leptons with the ATLAS experiment*, Eur. Phys. J. **C76** (2016) 295, arXiv:1512.05955 [hep-ex].

[27] P. Calafiura, W. Lavrijsen, C. Leggett, M. Marino, and D. Quarrie, *The Athena control framework in production, new developments and lessons learned*, in *Computing in high energy physics and nuclear physics. Proceedings, Conference, CHEP'04, Interlaken, Switzerland, September 27-October 1, 2004*. 2005.

[28] G. Barrand et al., *GAUDI - The software architecture and framework for building LHCb data processing applications*, in *Proceedings, 11th International Conference on Computing in High-Energy and Nuclear Physics (CHEP 2000): Padua, Italy, February 7-11, 2000*. 2000.

[29] C. P. Bee, D. Francis, L. Mapelli, R. McLaren, G. Mornacchi, J. Petersen, and F. J. Wickens, *The raw event format in the ATLAS Trigger & DAQ*, Tech. Rep. ATL-DAQ-98-129, CERN, Geneva, Feb, 2016. https://cds.cern.ch/record/683741. Revised version number 5 submitted on 2016-11-03 11:47.

[30] D. Schaefer, *The ATLAS Diamond Beam Monitor: Luminosity Detector on the LHC*, Tech. Rep. ATL-INDET-PROC-2015-009, CERN, Geneva, Jul, 2015. https://cds.cern.ch/record/2034225.

[31] B. Chen, D. Falchieri, A. Kugel, and J. Mayer, *IBL ROD BOC manual, developer version*, tech. rep., CERN, Geneva, August, 2014. https://espace.cern.ch/atlas-ibl/OffDecWG/Shared%20Documents/Readout%20System/IBL%20ROD/iblRodBocManual_v1.2.3.pdf.

[32] FE-I4 Collaboration, *The FE-I4B Integrated Circuit Guide*, tech. rep., CERN, Geneva, December, 2012. https://espace.cern.ch/atlas-ibl/ModuleWG/Shared%20Documents/FE-I4B-chip/FE-I4B_V2.3.pdf.

[33] T. Hemperek et al., *Digital Architecture of the New ATLAS Pixel Chip FE-I4*, in *Proceedings, 2009 IEEE Nuclear Science Symposium and Medical Imaging Conference (NSS/MIC 2009): Orlando, Florida, October 25-31, 2009*. 2009.

[34] F. Akesson et al., *ATLAS Inner Detector Event Data Model*, Tech. Rep. ATL-SOFT-PUB-2007-006, ATL-COM-SOFT-2007-015, CERN, Dec, 2007. https://cds.cern.ch/record/1074712.

[35] A. Valassi, R. Basset, M. Clemencic, G. Pucciani, S. A. Schmidt, and M. Wache, *COOL, LCG Conditions Database for the LHC Experiments:*

Development and Deployment Status. LHC: Large Hadron Collider, Tech. Rep. CERN-IT-Note-2008-019, CERN, Geneva, Nov, 2008. https://cds.cern.ch/record/1142723.

[36] S. McMahon, P. Allport, H. Hayward, and B. Di Girolamo, *Initial Design Report of the ITk: Initial Design Report of the ITk*, Tech. Rep. ATL-COM-UPGRADE-2014-029, CERN, Geneva, Oct, 2014. https://cds.cern.ch/record/1952548.

[37] G. Lindström, *Radiation damage in silicon detectors*, Nuclear Instruments and Methods in Physics Research A **512** (2003) 30–43.

[38] A. Vasilescu, *Overview on the radiation environment in ATLAS and CMS SCT and the irradiation facilities used for damage studies*, tech. rep., CERN, 1997. https://rd48.web.cern.ch/rd48/technical-notes/rosetn972.ps.

[39] L. Rossi, P. Fischer, T. Rohe, and N. Wermes, *Pixel Detectors: From Fundamentals to Applications*. Particle Acceleration and Detection. Springer-Verlag Berlin Heidelberg, 1 ed., 2006.

[40] V. Eremin, E. Verbitskaya, and Z. Li, *Effect of radiation induced deep level traps on Si detector performance*, Nuclear Instruments and Methods in Physics Research Section A: Accelerators, Spectrometers, Detectors and Associated Equipment **476** (2002) 537 – 549.

[41] M. Moll, *Radiation damage in silicon particle detectors: microscopic defects and macroscopic properties*. PhD thesis, 1999. https://cds.cern.ch/record/425274. DESY-THESIS-1999-040.

[42] F. Hartmann, *Evolution of Silicon Sensor Technology in Particle Physics*, vol. 231 of *Springer Tracts in Modern Physics*. Springer International Publishing, 1 ed., 2009.

[43] G. A. et. al., *ATLAS pixel detector electronics and sensors*, Journal of Instrumentation **3** (2008) P07007, http://stacks.iop.org/1748-0221/3/i=07/a=P07007.

[44] M. Benoit, M. Bomben, R. Carney, G. Giugliarelli, T. Lari, L. Meng, B. P. Nachman, L. Rossini, V. Wallangen, J.-c. Beyer, A. Ducourthial, A. Macchiolo, J. Llorente Merino, P. Miyagawa, I. Dawson, N. Dann, and C. Da Via, *Modeling Radiation Damage Effects for Pixel Sensors in the ATLAS Detector*, Tech. Rep. ATL-COM-INDET-2017-011, CERN, Geneva, Mar, 2017. https://cds.cern.ch/record/2255825.

[45] ATLAS Pixel Collaboration Collaboration, I. e. a. Gorelov, *A Measurement of Lorentz Angle and Spatial Resolution of Radiation Hard Silicon Pixel Sensors*, Nucl. Instrum. Methods Phys. Res., A **481** (2001) 204–221. 26 p, http://cds.cern.ch/record/681508.

[46] C. Troncon, *Detailed studies of the ATLAS pixel detectors*, IEEE Transactions on Nuclear Science **47** (2000) 737–744.

[47] A. Wharton, W. Yao, and R. Jansky, *ATLAS Inner Detector Track Quality Cuts for Run 2*, Tech. Rep. ATL-COM-PHYS-2014-1084, CERN, Geneva, Aug, 2014. https://cds.cern.ch/record/1752536.

[48] *Study of the mechanical stability of the ATLAS Insertable B-Layer*, Tech. Rep. ATL-INDET-PUB-2015-001, CERN, Geneva, Jun, 2015. https://cds.cern.ch/record/2022587.

[49] *Alignment of the ATLAS Inner Detector with the initial LHC data at* $\sqrt{s} = 13$ *TeV*, Tech. Rep. ATL-PHYS-PUB-2015-031, CERN, Geneva, Jul, 2015. https://cds.cern.ch/record/2038139.

[50] *Alignment of the ATLAS Inner Detector and its Performance in 2012*, Tech. Rep. ATLAS-CONF-2014-047, CERN, Geneva, Jul, 2014. https://cds.cern.ch/record/1741021.

[51] S. Berge, W. Bernreuther, and S. Kirchner, *Prospects of constraining the Higgs bosons CP nature in the tau decay channel at the LHC*, Phys. Rev. **D92** (2015) 096012, arXiv:1510.03850 [hep-ph].

[52] S. Berge, W. Bernreuther, and S. Kirchner, *Determination of the Higgs CP-mixing angle in the tau decay channels*, Nucl. Part. Phys. Proc. **273-275** (2016) 841–845, arXiv:1410.6362 [hep-ph].

[53] S. Berge, W. Bernreuther, and S. Kirchner, *Determination of the Higgs CP-mixing angle in the tau decay channels at the LHC including the DrellYan background*, Eur. Phys. J. **C74** (2014) 3164, arXiv:1408.0798 [hep-ph].

[54] A. Elagin, P. Murat, A. Pranko, and A. Safonov, *A New Mass Reconstruction Technique for Resonances Decaying to di-tau*, Nucl. Instrum. Meth. **A654** (2011) 481–489, arXiv:1012.4686 [hep-ex].

[55] T. Sjostrand, S. Mrenna, and P. Z. Skands, *A Brief Introduction to PYTHIA 8.1*, Comput. Phys. Commun. **178** (2008) 852–867, arXiv:0710.3820 [hep-ph].

[56] A. Kaczmarska, J. Piatlicki, T. Przedzinski, E. Richter-Was, and Z. Was, *Application of TauSpinner for Studies on* τ*-Lepton Polarization and Spin Correlations in Z, W and H Decays at the LHC*, Acta Phys. Polon. **B45** (2014) 1921–1946, arXiv:1402.2068 [hep-ph].

[57] T. Przedzinski, E. Richter-Was, and Z. Was, *TauSpinner: a tool for simulating CP effects in* $H \to \tau\tau$ *decays at LHC*, Eur. Phys. J. **C74** (2014) 3177, arXiv:1406.1647 [hep-ph].

[58] Z. Czyczula, T. Przedzinski, and Z. Was, *TauSpinner Program for Studies on Spin Effect in tau Production at the LHC*, Eur. Phys. J. **C72** (2012) 1988, arXiv:1201.0117 [hep-ph].

[59] P. Nason, *A New method for combining NLO QCD with shower Monte Carlo algorithms*, JHEP **11** (2004) 040, arXiv:hep-ph/0409146 [hep-ph].

[60] S. Frixione, P. Nason, and C. Oleari, *Matching NLO QCD computations with Parton Shower simulations: the POWHEG method*, JHEP **11** (2007) 070, arXiv:0709.2092 [hep-ph].

[61] S. Alioli, P. Nason, C. Oleari, and E. Re, *A general framework for implementing NLO calculations in shower Monte Carlo programs: the POWHEG BOX*, JHEP **06** (2010) 043, arXiv:1002.2581 [hep-ph].

[62] S. Alioli, P. Nason, C. Oleari, and E. Re, *NLO Higgs boson production via gluon fusion matched with shower in POWHEG*, JHEP **04** (2009) 002, arXiv:0812.0578 [hep-ph].

[63] P. Nason and C. Oleari, *NLO Higgs boson production via vector-boson fusion matched with shower in POWHEG*, JHEP **02** (2010) 037, arXiv:0911.5299 [hep-ph].

[64] H.-L. Lai, M. Guzzi, J. Huston, Z. Li, P. M. Nadolsky, J. Pumplin, and C. P. Yuan, *New parton distributions for collider physics*, Phys. Rev. **D82** (2010) 074024, arXiv:1007.2241 [hep-ph].

[65] P. Richardson, *Spin correlations in Monte Carlo simulations*, JHEP **11** (2001) 029, arXiv:hep-ph/0110108 [hep-ph].

[66] P. Ilten, *Tau Decays in Pythia 8*, Nucl. Phys. Proc. Suppl. **253-255** (2014) 77–80, arXiv:1211.6730 [hep-ph].

[67] P. Ilten, *Electroweak and Higgs Measurements Using Tau Final States with the LHCb Detector*. PhD thesis, University Coll., Dublin, 2013-09-06. arXiv:1401.4902 [hep-ex]. https://inspirehep.net/record/1278195/files/arXiv:1401.4902.pdf.

[68] P. Golonka, B. Kersevan, T. Pierzchala, E. Richter-Was, Z. Was, and M. Worek, *The tauola-photos-F environment for the TAUOLA and PHOTOS packages, release II*, Computer Physics Communications **174** (2006) 818 – 835, http://www.sciencedirect.com/science/article/pii/S0010465506000403.

[69] M. Chrzaszcz, T. Przedzinski, Z. Was, and J. Zaremba, *TAUOLA of tau lepton decays– framework for hadronic currens, matrix elements and anomalous decays*, arXiv:1609.04617 [hep-ph].

[70] ATLAS Collaboration, G. Aad et al., *Evidence for the Higgs-boson Yukawa coupling to tau leptons with the ATLAS detector*, JHEP **04** (2015) 117, arXiv:1501.04943 [hep-ex].

[71] ATLAS Collaboration, G. Aad et al., *Test of CP Invariance in vector-boson fusion production of the Higgs boson using the Optimal Observable method in the ditau decay channel with the ATLAS detector*, Eur. Phys. J. **C76** (2016) 658, arXiv:1602.04516 [hep-ex].

[72] J. Butterworth et al., *PDF4LHC recommendations for LHC Run II*, J. Phys. **G43** (2016) 023001, arXiv:1510.03865 [hep-ph].

[73] ATLAS Collaboration, G. Aad et al., *Measurement of the Z/γ^* boson transverse momentum distribution in pp collisions at $\sqrt{s} = 7$ TeV with the ATLAS detector*, JHEP **09** (2014) 145, arXiv:1406.3660 [hep-ex].

[74] J. Pumplin, D. R. Stump, J. Huston, H. L. Lai, P. M. Nadolsky, and W. K. Tung, *New generation of parton distributions with uncertainties from global QCD analysis*, JHEP **07** (2002) 012, arXiv:hep-ph/0201195 [hep-ph].

[75] N. Davidson, T. Przedzinski, and Z. Was, *PHOTOS interface in C++: Technical and Physics Documentation*, Comput. Phys. Commun. **199** (2016) 86–101, arXiv:1011.0937 [hep-ph].

[76] LHC Higgs Cross Section Working Group Collaboration, D. de Florian et al., *Handbook of LHC Higgs Cross Sections: 4. Deciphering the Nature of the Higgs Sector*, arXiv:1610.07922 [hep-ph].

[77] P. Bolzoni, F. Maltoni, S.-O. Moch, and M. Zaro, *Higgs production via vector-boson fusion at NNLO in QCD*, Phys. Rev. Lett. **105** (2010) 011801, arXiv:1003.4451 [hep-ph].

[78] T. Gleisberg, S. Hoeche, F. Krauss, M. Schonherr, S. Schumann, F. Siegert, and J. Winter, *Event generation with SHERPA 1.1*, JHEP **02** (2009) 007, arXiv:0811.4622 [hep-ph].

[79] S. Kallweit, J. M. Lindert, P. Maierhofer, S. Pozzorini, and M. Schönherr, *NLO QCD+EW predictions for V + jets including off-shell vector-boson decays and multijet merging*, JHEP **04** (2016) 021, arXiv:1511.08692 [hep-ph].

[80] NNPDF Collaboration, R. D. Ball et al., *Parton distributions for the LHC Run II*, JHEP **04** (2015) 040, arXiv:1410.8849 [hep-ph].

[81] P. Z. Skands, *Tuning Monte Carlo Generators: The Perugia Tunes*, Phys. Rev. **D82** (2010) 074018, arXiv:1005.3457 [hep-ph].

[82] S. Agostinelli et al., *Geant4a simulation toolkit*, Nuclear Instruments and Methods in Physics Research Section A: Accelerators, Spectrometers, Detectors and Associated Equipment **506** (2003) 250 – 303, http://www.sciencedirect.com/science/article/pii/S0168900203013688.

[83] ATLAS Collaboration, G. Aad et al., *The ATLAS Simulation Infrastructure*, Eur. Phys. J. **C70** (2010) 823–874, arXiv:1005.4568 [physics.ins-det].

[84] A. D. Martin, W. J. Stirling, R. S. Thorne, and G. Watt, *Parton distributions for the LHC*, Eur. Phys. J. **C63** (2009) 189–285, arXiv:0901.0002 [hep-ph].

[85] *Summary of ATLAS Pythia 8 tunes*, Tech. Rep. ATL-PHYS-PUB-2012-003, CERN, Geneva, Aug, 2012. https://cds.cern.ch/record/1474107.

[86] ATLAS Collaboration Collaboration,, *The ATLAS Tau Trigger in Run 2*, Tech. Rep. ATLAS-CONF-2017-061, CERN, Geneva, Jul, 2017. https://cds.cern.ch/record/2274201.

[87] *Jet Calibration and Systematic Uncertainties for Jets Reconstructed in the ATLAS Detector at* $\sqrt{s}$ = 13 *TeV*, Tech. Rep. ATL-PHYS-PUB-2015-015, CERN, Geneva, Jul, 2015. http://cds.cern.ch/record/2037613.

[88] ATLAS Collaboration Collaboration,, *Measurement of the tau lepton reconstruction and identification performance in the ATLAS experiment using pp collisions at* $\sqrt{s}$ = 13 TeV, Tech. Rep. ATLAS-CONF-2017-029, CERN, Geneva, May, 2017. http://cds.cern.ch/record/2261772.

[89] ATLAS Collaboration, G. Aad et al., *Performance of algorithms that reconstruct missing transverse momentum in* $\sqrt{s}$ = *8 TeV proton-proton collisions in the ATLAS detector*, Eur. Phys. J. **C77** (2017) 241, arXiv:1609.09324 [hep-ex].

[90] J. Alison, B. Cooper, and T. Goettfert, *Production of Residual Systematically Misaligned Geometries for the ATLAS Inner Detector*, Tech. Rep. ATL-INDET-INT-2009-003. ATL-COM-INDET-2009-003, CERN, Geneva, Oct, 2009. https://cds.cern.ch/record/1154987. Approval requested a second time to resolve issues in CDS.

[91] The Sherpa team, *Scale depedence in SHERPA [sic]*, tech. rep., abc, 2015. https://sherpa.hepforge.org/doc/ScaleVariations-Sherpa-2.2.0.pdf.

[92] L. Lista, *Statistical Methods for Data Analysis in Particle Physics*, vol. 909. Springer International Publishing, 2016.

[93] G. Apollinari, O. Brning, T. Nakamoto, and L. Rossi, *High Luminosity Large Hadron Collider HL-LHC*, CERN Yellow Report (2015) 1–19, arXiv:1705.08830 [physics.acc-ph].

[94] P. Baldi, P. Sadowski, and D. Whiteson, *Searching for Exotic Particles in High-Energy Physics with Deep Learning*, Nature Commun. **5** (2014) 4308, arXiv:1402.4735 [hep-ph].

[95] P. Baldi, P. Sadowski, and D. Whiteson, *Enhanced Higgs Boson to* $\tau^+\tau^-$ *Search with Deep Learning*, Phys. Rev. Lett. **114** (2015) 111801, arXiv:1410.3469 [hep-ph].

[96] F. Chollet et al., *Keras*, https://github.com/fchollet/keras, 2015.

[97] M. Abadi et al., *TensorFlow: Large-Scale Machine Learning on Heterogeneous Systems*, 2015. https://www.tensorflow.org/. Software available from tensorflow.org.

[98] V. Nair and G. E. Hinton, *Rectified Linear Units Improve Restricted Boltzmann Machines*, in *Proceedings of ICML*. 2010.

[99] S. Ioffe and C. Szegedy, *Batch Normalization: Accelerating Deep Network Training by Reducing Internal Covariate Shift*, CoRR **abs/1502.03167** (2015), arXiv:1502.03167, http://arxiv.org/abs/1502.03167.

[100] N. Srivastava, G. Hinton, A. Krizhevsky, I. Sutskever, and R. Salakhutdinov, *Dropout: A Simple Way to Prevent Neural Networks from Overfitting*, J. Mach. Learn. Res. **15** (2014) 1929–1958, http://dl.acm.org/citation.cfm?id=2627435.2670313.

[101] D. P. Kingma and J. Ba, *Adam: A Method for Stochastic Optimization*, ArXiv e-prints (2014), arXiv:1412.6980 [cs.LG].

[102] M. Sugiyama, *Introduction to Statistical Machine Learning*. Morgan Kaufmann Publishers Inc., San Francisco, CA, USA, 2016.

[103] P. J. Huber, *Robust Estimation of a Location Parameter*, Ann. Math. Statist. **35** (1964) 73–101, https://doi.org/10.1214/aoms/1177703732.

[104] O. Behnke, K. Krninger, T. Schrner-Sadenius, and G. Schott, eds., *Data analysis in high energy physics*. Wiley-VCH, Weinheim, Germany, 2013. http://www.wiley-vch.de/publish/dt/books/ISBN3-527-41058-9.

[105] N. V. Chawla, K. W. Bowyer, L. O. Hall, and W. P. Kegelmeyer, *SMOTE: Synthetic Minority Over-sampling Technique*, J. Artif. Int. Res. **16** (2002) 321–357, http://dl.acm.org/citation.cfm?id=1622407.1622416.

Grafisk design: Kommunikasjonsavdelingen, UiB / Trykk: Skipnes Kommunikasjon AS

uib.no

ISBN: 978-82-308-3776-4